Brownian motion under external force field and anomalous diffusion

Oussama Sentissi

UNIVERSITÉ DE STRASBOURG

École Doctorale des sciences chimiques

UMR 7006 : Institut de Science et Ingénierie Supramoléculaires

THÈSE

présentée par :

Oussama SENTISSI

soutenue le : **07 Décembre 2018**

pour obtenir le grade de : **Docteur de l'université de Strasbourg**

Discipline/ Spécialité : Physique

Étude du mouvement Brownien sous champ de force externe et diffusions anormales

THÈSE dirigée par :

Mr. GENET Cyriaque, directeur de recherche CNRS, ISIS, UMR 7006, CNRS-Université de Strasbourg

RAPPORTEURS :

Mr. DUJARDIN Erik, directeur de recherche CNRS, CEMES, UPR 8011, CNRS-Université Paul-Sabatier de Toulouse

Mr. DEGIRON Aloyse, chargé de recherche CNRS, C2N, UMR 9001, CNRS-Université Paris-Saclay

---

AUTRES MEMBRES DU JURY :

Mr. HEBRAUD Pascal, directeur de recherche CNRS, IPCMS, UMR 7504, CNRS-Université de Strasbourg

Mme DAGENS Béatrice, directrice de recherche CNRS, C2N, UMR 9001, CNRS-Université Paris-Saclay

CONTENTS

1 INTRODUCTION 16
- 1.1 An Introduction on Brownian motion 17
- 1.2 Colloidal suspensions 19
- 1.3 Dynamical behavior of colloidal particles under external force fields 21

2 SINGLE PARTICLE TRACKING IN COLLOIDAL SUSPENSIONS 26
- 2.1 An optical microscope for colloidal tracking and optical force measurements 26
  - 2.1.1 Experimental Setup 27
  - 2.1.2 Gaussian beam optics 28
- 2.2 Colloidal suspensions in a fluidic cell 29
- 2.3 Dark field microscopy and spatial calibration 31
  - 2.3.1 Pixel size calibration 33
  - 2.3.2 Tracking the positions of the particles 34
  - 2.3.3 Localisation errors 35
- 2.4 Statistical properties of Brownian motion 38
  - 2.4.1 Probability density function (PDF) 38
  - 2.4.2 Mean Squared Displacement (MSD) 41
- 2.5 Conclusion 42

3 BROWNIAN COLLOIDAL PARTICLES IN EXTERNAL FORCE FIELDS : FROM SEDIMENTATION TO CONVECTIVE TRANSPORT 44
- 3.1 Controlling the colloidal assembly with tunable laser irradiation 45
  - 3.1.1 Force balance point of view 46
  - 3.1.2 Laser induced convective flow 48
  - 3.1.3 Quantitative analysis of both regimes 49
  - 3.1.4 Intermediate laser power : a colloidal suspension regime 52
  - 3.1.5 Mean-square displacement 53
  - 3.1.6 Diffusion Coefficient from the probability density function of displacement 56
  - 3.1.7 Suspension regime : Influence of the density of the colloidal particles 60
  - 3.1.8 Steady state dynamics 61
- 3.2 Modeling the light-induced convective currents 62

3.2.1 Formulation of the problem 62
3.2.2 Modeling the heat transfer. 64
3.2.3 Thermal vs velocity boundary layer thicknesses 66
3.2.4 Fluidic velocity profile 68
3.3 Conclusion 71
4 MEASURING RADIATION PRESSURE AT A FEMTO NEWTON RESOLUTION LEVEL WITH BROWNIAN COLLOIDS 72
4.1 Optical forces measurement. 72
4.1.1 Optical forces in Mie regime 73
4.1.2 Optical Setup 74
4.2 Brownian motion in an external force field 74
4.2.1 Langevin equation 74
4.2.2 Free Brownian Motion in the over-damped regime 75
4.2.3 External conservative force on a Brownian particle 78
4.2.4 Measurement uncertainties 80
4.3 Stationarity and ergodicity aspects 82
4.3.1 PDF of position 82
4.3.2 PDF of displacements 88
4.3.3 Autocorrelation function 91
4.3.4 Ergodic steady state 92
4.4 Statistical resolution 95
4.4.1 Force estimator. 95
4.4.2 Simulation results 97
4.5 Global noise and stability 98
4.6 Radiation pressure force measurements. 101
4.6.1 One beam configuration 101
4.6.2 Resolution and sensitivity 102
4.6.3 Force field profile reconstruction 104
4.7 Conclusion 106
5 OBSERVINGING ANOMALOUS BROWNIAN TRAJECTORIES WITHIN A COLLOIDAL ASSEMBLY 107
5.1 Observing anomalous diffusion 108
5.2 From ensemble to single particle analysis 110
5.3 Anomalous mean squared displacements 112
5.4 Displacement distributions and ergodicity 113
5.5 Conclusion 118
6 CONCLUSION AND PERSPECTIVES 120
Appendices 123

A HEAT EQUATION SOLUTION 124

B NAVIER-STOKES EQUATION SOLUTION 126

ACKNOWLEDGEMENTS

First of all, I would like to thank my thesis director Dr. Cyriaque Genet for his availability, guidance and instruction. His enthusiasm, passion and discussions were a great source of encouragement and inspiration for me. He is a great person from both the scientific and human point of view.

I also want to especially thank Pr. Thomas W. Ebbesen for giving me the opportunity to work in his outstanding laboratory. His unconditional support and excellent advices.

I would like to express my gratitude to Dr. Béatrice Dagens, Dr. Erik Dujardin, Dr. Aloyse Degiron and Dr. Pascal Hebraud for accepting to be the jury members of my thesis, but also for the curiosity they express toward my work. In particular, I am indebted to Dr. Dagens for having accepted our late invitation, thus making my defense possible.

During the last three years as a PhD student, I enjoyed working in a warm, stimulating and supportive environment. Furthermore, it was delightful to cohabitate with exceptional colleagues, to just cite few : Vincent, Youssef, Ricardo, Mike, Marc-Antoine, all Marcos, Lucas, Alessandra, Alessandro, Akihiro, Taki,...

I am in debt to all the past and present members of the nanostructures laboratory. First, I want to thank Thibault Chervy, Gabriel Schnoering, Shaojun Wang and Hadi Bahsoun the first generation of PhDs for their advices and stimulating discussions. I wish to thank also the second generation of PhDs Yoseline, Minghao, Jérôme and all the trainees for the inspiring discussions and the good mood in the laboratory. Then, I would like to extend my gratitude to all the post docs starting by "the great" Stefano Azzini, Jino George, Anoop-san, Robrecht, Atef, Xiaolan, Kalaivanan... I moreover want to thank Eloïse Devaux and James Hutchison for their kindness, joviality and their good advices . A special thanks to Marie-Claude, who was always up to date with every administrative matter. In this sense, I would like to thank all the administrative staff starting from

Muriel, Claire,... and the logistic staff Thierry, Philippe,...

My physicist friends on daily basis Ziyad, Tapas, David, Etienne, François, Kevin, Arthur, Jean Yves, Manu... for the exciting discussions and vigorous debates. I would like to adress my thanks to my non-physicist friends Julien, Thomsy, Mel, Pedro, Yul, for their support.

Finally, I would love to express my greatest thanks to my family. Especially to my parents for all the sacrifices and infinite support, and I desire to thank my beloved Morgane for her affection and goodness.

RÉSUMÉ ÉTENDU

Les mesures de forces faibles aux échelles micro et nanométrique ont plusieurs applications dans différentes disciplines telles que la physique, la chimie et la biologie. A ces échelles, le mouvement Brownien est inéluctable, fixe une limite de résolution et représente un bruit pour la mesure de telles forces.

Ce travail de thèse s'inscrit dans ce contexte. Plus précisément, nous nous intéressons à la dynamique de suspensions colloïdales dispersées dans l'eau à température ambiante, pour valider leur intérêt dans un contexte de mesure de forces optiques de faible intensité. Pour ce faire, nous avons construit un microscope à champ noir permettant de suivre les particules et de reconstruire leurs trajectoires. Ces dernières sont ensuite analysées statistiquement afin de soustraire la contribution balistique au mouvement de la particule. En effet, la contribution balistique est directement proportionnelle au champ de force appliqué à la particule et c'est elle qui permettra la mesure de la force. Au niveau de résolution que nous visons, la sonde laser permettant l'observation des trajectoires influence directement la dynamique de l'ensemble colloïdal. Nous démontrons ainsi l'existence de trois régimes distincts en fonction de la puissance laser injectée dans le système:

- Basse puissance : les particules sédimentent car leur densité volumique est plus grande que celle de l'eau ;
- Puissance intermédiaire : la sédimentation des particules est compensée par le courant convectif induit par le gradient de température résultant de l'absorption par l'eau de la puissance du laser à la longueur d'onde de travail ;
- Haute puissance : les particules sont entrainées par un courant convectif induit dominant la sédimentation.

Il est ensuite essentiel de valider les hypothèses de stationnarité et d'ergodicité qui sont fondamentales pour mettre en place notre méthode de mesure de force. L'analyse statistique fine de notre système nous permet de mettre en évidence et de caractériser des effets de diffusion anormale brownienne. Nos expériences révèlent en effet la présence de trajectoires anormales dont l'origine se comprend comme un effet d'interaction entre

la particule suivie et le reste de l'ensemble colloïdal. Ces expériences montrent notamment la richesse dynamique d'une suspension colloïdale qui s'inscrit dans la famille des systèmes où ces effets de diffusion anormale sont observés [1].

La thèse est structurée en quatre chapitres. Le premier chapitre décrit le système expérimental et le microscope à champ noir que nous avons construit. Il présente également l'ensemble des outils et méthodes utilisés pour l'enregistrement des trajectoires colloïdales et leur analyse statistique.

Le deuxième chapitre décrit en détail les trois régimes dynamiques observés en fonction de la puissance du laser du microscope. Un modèle théorique permettant de comprendre ces différents régimes est également proposé. Ce modèle couple une description Navier-Stokes du fluide à une équation de la chaleur.

Le troisième chapitre présente les résultats de mesures de forces optiques réalisées sur l'ensemble statistique formé par la suspension colloïdale. Une résolution de 0.3 fN est démontrée.

Le dernier chapitre rassemble les mesures effectuées sur les trajectoires browniennes anormales que nous avons pu repérer parmi l'ensemble colloïdal grâce aux spécificités de notre microscopie à champ noir. Nous décrivons ci-dessous plus en détails le contenu technique et physique des chapitres 2, 3 et 4.

Le montage optique réalisé au cours de la thèse est présenté dans la figure (0.1). Le faisceau d'une diode laser à 637 nm ayant un profil Gaussien est séparé en deux pinceaux dont les polarisations sont perpendiculaires, focalisés au niveau de l'échantillon de telle sorte que les deux faisceaux soient confondus aux plans focaux respectifs.

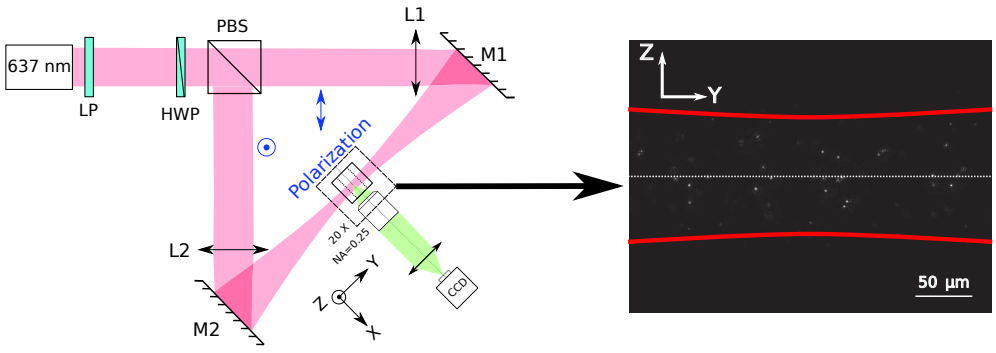

Figure 0.1 – Montage optique réalisé au cours de la thèse. Le montage est utilisé soit en injectant toute la puissance laser dans un bras, soit en équilibrant la puissance injectée dans les deux bras.

La lumière diffusée par chaque particule, illuminée par le faisceau, est collectée par un objectif placé perpendiculairement à l'axe optique. Un exemple d'image obtenue par le microscope à champ sombre est présenté à la droite du schéma du montage optique dans la figure (0.1).

Les particules sont localisées à l'aide d'un greffon [2] du logiciel libre de traitement d'image ImageJ. La taille d'un pixel est $p_s = 540nm \pm 5nm$, avec une résolution sur le déplacement mesurée $\Delta r = 20nm$ entre deux images successives. Chaque position est enregistrée avec une fréquence de 120 Hz. On reconstruit ainsi la trajectoire de la particule avec un pas temporel $\Delta t = 8ms$. L'estimateur de la moyenne de déplacement suivant l'axe vertical est calculé par :

$$\mu_i^{\Delta Z} = \frac{\sum_{n=1}^{N_i} Z_{n+1} - Z_n}{N_i - 1}, \tag{0.1}$$

Où Z_n est la position détectée à l'instant $t = n\Delta t$ dans l'image n, et N_i est la longueur de la trajectoire i, la vitesse moyenne est définie par :

$$< V_z >_{N_T} = \frac{< \mu_j^{\Delta Z} >_{N_T}}{\Delta t}, \tag{0.2}$$

Avec N_T le nombre de trajectoires détectées.

Dans la figure (0.2) est représentée l'évolution de l'estimateur de la vitesse moyenne verticale $< V_Z >$ en fonction de la puissance totale injectée dans le système. La zone bleue représente le régime de sédimentation, la zone rouge le régime de convection et celle en blanc le régime de suspension.

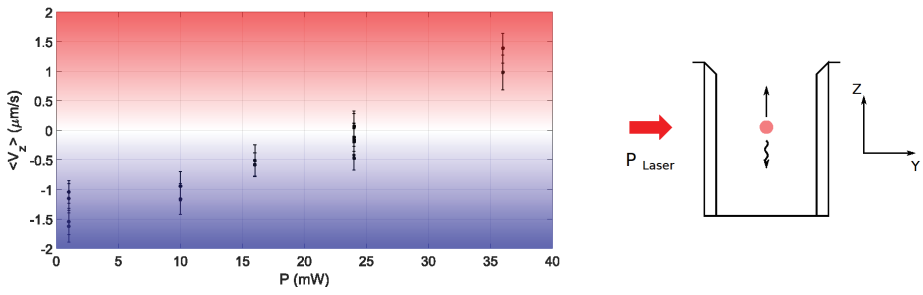

Figure 0.2 – Vitesse moyenne mesurée en fonction de la puissance laser. Dans cet exemple, il s'agit de particules de Mélamine de rayon r = 470 nm. On répète l'expérience à chaque puissance afin de vérifier la reproductibilité des vitesses mesurées à une puissance donnée. On constate que les valeurs moyennes se chevauchent.

On montre bien l'existence de trois régimes dynamiques différents en fonction de la puissance laser injectée dans le système.

Dans l'optique de mesurer des forces faibles, les propriétés statistiques du mouvement brownien offrent un moyen efficace de réduire l'erreur sur la mesure en augmentant la taille de l'échantillon statistique. En effet, la mesure de forces nécessite une résolution à la limite thermique définie par :

$$< \delta F >= \sqrt{\frac{2 k_B T \gamma}{N_t \Delta t}} \tag{0.3}$$

Où N_t est l'ensemble de tous les déplacements détectés au cours d'une expérience, $k_B T$ l'énergie thermique et γ le coefficient de trainée donné par la loi de Stokes pour des particules sphériques. Dans nos conditions expérimentales, la limite thermique en fonction du nombre de points est donnée par :

$$< \delta F >= \frac{93.5 \text{ fN}}{\sqrt{N_t}} \tag{0.4}$$

De là, vient l'idée d'augmenter la taille de l'ensemble statistique. La force est alors donnée [3] par :

$$< F_y >= \frac{< \mu_y > \gamma}{\Delta t} \tag{0.5}$$

Où $< \mu_y >$ est le décalage, de la distribution des déplacements, induit par le champ de force appliqué sur les particules. On injecte toute la puissance laser dans un seul bras « voir figure (0.1) » et on mesure la force moyenne de pression de radiation appliquée sur l'ensemble des particules. Les résultats sont présentés dans la figure (0.3).

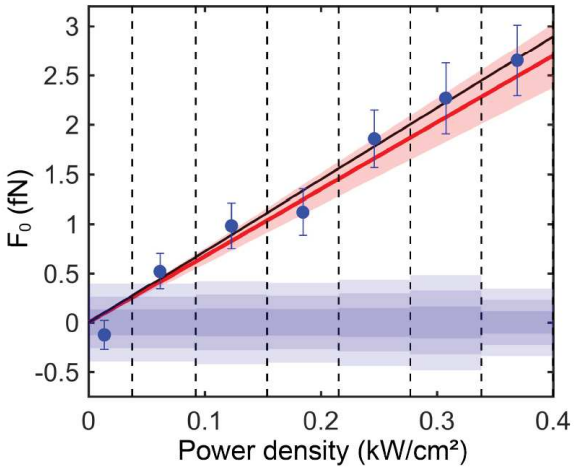

Figure 0.3 – Pression de radiation mesurée. La limite thermique est représentée à 1σ, 2σ et 3σ.

Les valeurs mesurées sont comparées à la valeur calculée en utilisant la théorie de Mie pour la diffusion de la lumière par une particule sphérique. Les résultats sont bien en accord avec notre mesure. Dans le but de quantifier la sensibilité de notre méthode de mesure, nous utilisons la configuration à deux bras « voire figure (0.1) ». Les résultats sont présentés dans la figure (0.4). On atteint une sensibilité d'un femto newton avec une résolution de 0.3 fN.

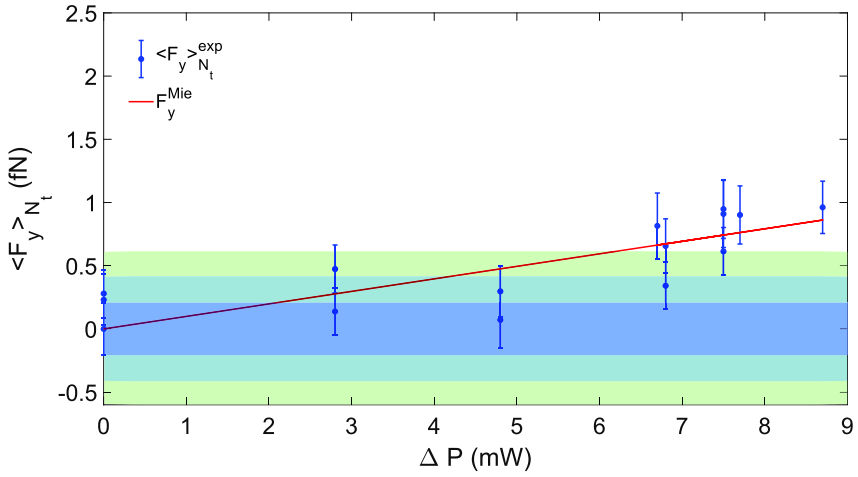

Figure 0.4 – Configuration où la différence de puissance entre les deux faisceaux est réglée finement. Afin de mesuré la force minimale détectable par notre montage optique.

Avec ces mesures, il est également possible de reconstruire le champ de force qui suit le profil d'intensité du laser. Les résultats pour la reconstruction du profil du champ de force sont présentés figure (0.5), où il apparait bien que le profil du champ de force suit précisément le profil d'intensité

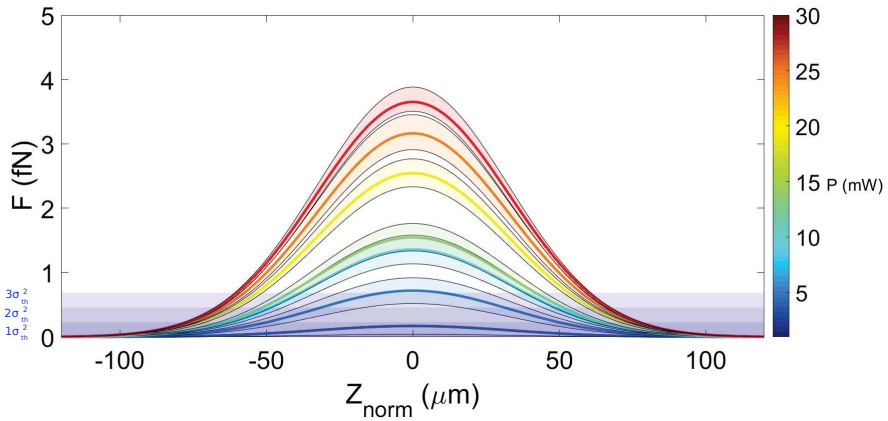

Figure 0.5 – Profil de force reconstruit à partir du profil d'intensité pour différentes puissances.

Dans un ensemble colloïdal diffusif, certaines particules peuvent se retrouver dans le même voisinage ce qui induit une interaction particule-particule. Nous avons mesuré que ces interactions correspondent à des trajectoires diffusant anormalement. Afin de quantifier nos observations, le déplacement quadratique moyen (Time Averaged Mean Squarre Displacement) TAMSD est mesuré. Il est défini comme suit :

$$\delta_j r^2(\tau_n) = \frac{1}{N_j} \sum_{i=1}^{N_j} [r_{j+i} - r_j]^2 = 2D\Delta t. \tag{0.6}$$

Avec $\tau_n = n\Delta t, i = 1, 2, 3, \ldots, N_i/4$, est l'intervalle temporel sur lequel on moyenne les déplacements au carré. D est le coefficient de diffusion de la particule.

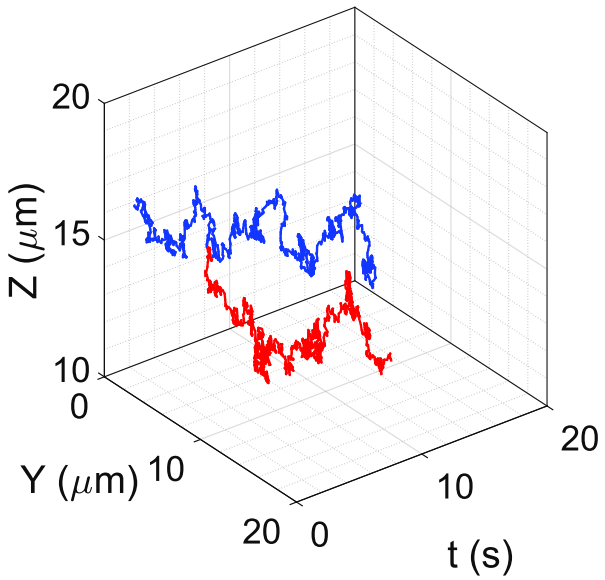

Figure 0.6 – Trajectoires de deux particules en interaction.

On représente dans la figure (0.6) un exemple de trajectoire où on observe cet effet de diffusion anormale, qui se traduit sur la TAMSD représentée dans la figure (0.7). La TAMSD prend la forme suivante:

$$\delta r^2(\tau) = K_\alpha \tau^\alpha. \tag{0.7}$$

Avec $\alpha < 1$.

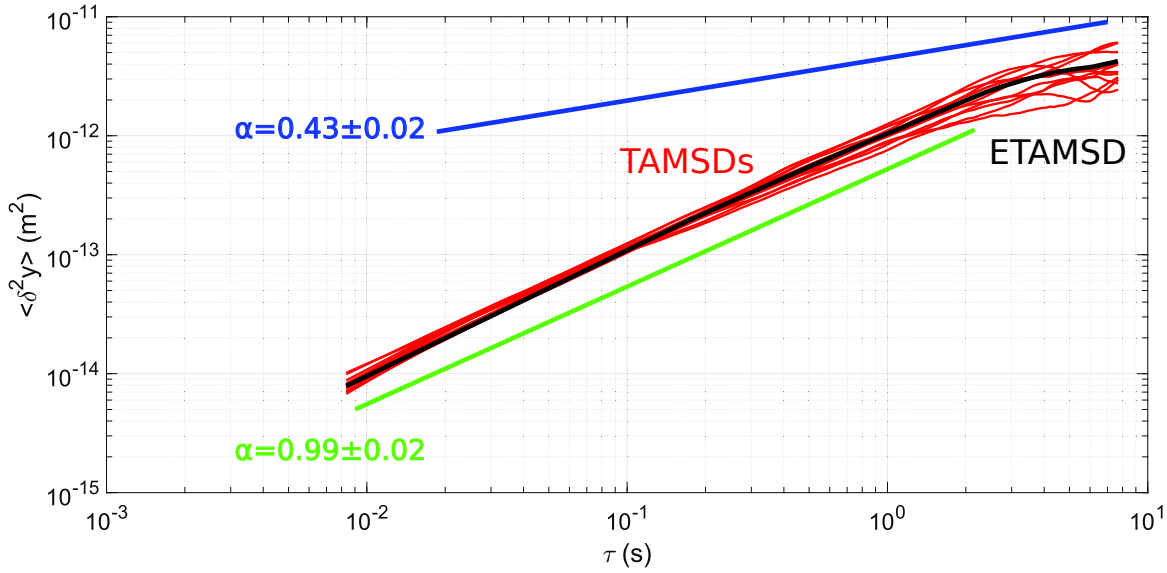

Figure 0.7 – MSDs des trajectoires anormales détectées en fonction du pas temporel.

On voit bien le changement de pente des TAMSDs moyennées temporellement pour toutes les particules sub-diffusives, caractéristiques d'un mouvement anormal. Ceci est clair aussi sur les (ETAMSD), TAMSD moyennées sur l'ensemble, qui correspondent simplement à la moyenne d'ensemble des TAMSDs. Deux pentes se distinguent clairement dans la figure (0.7).

On regarde ensuite les distributions des déplacements des particules diffusant anormalement. Les distributions sont représentées dans la figure (0.8). Les distributions sont bien Gaussiennes, respectant l'hypothèse de « Gaussianité » alors que la diffusion reste clairement anormale.

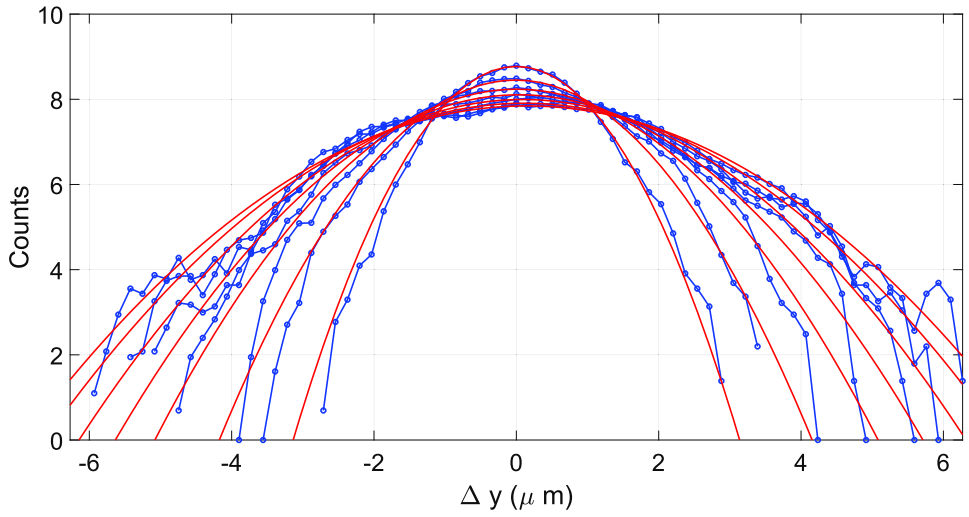

Figure 0.8 – Distributions de déplacements, à différents pas temporels, des trajectoires dont les MSDs sont anormales.

Afin de vérifier l'hypothèse ergodique, on utilise le paramètre ξ, défini ainsi [4] :

$$\xi = \frac{\delta r^2(\tau)}{< \delta r^2(\tau >} = \frac{\text{TAMSD}}{\text{ETAMSD}}, \tag{0.8}$$

qui nous renseigne sur le comportement de la TAMSD moyennée dans le temps d'une particule par rapport au comportement de la TAMSD moyennée dans le temps de l'ensemble de toutes les particules. Finalement, on exploite un paramètre connu pour caractériser le caractère non ergodique du système [5] :

$$\text{EB}(\tau) =< \xi^2 > - < \xi >^2, \tag{0.9}$$

Que l'on simplifie :

$$\text{EB}(\tau) =< \xi^2 > -1, \tag{0.10}$$

car $< \xi >^2 = 1$ par construction. Ce paramètre donne une condition suffisante pour l'hypothèse ergodique, mais on peut définir une condition nécessaire à partir de ϵB défini par :

$$\epsilon\text{B} = \frac{< \delta r^2(\tau) >}{< \Delta r^2(\tau >}. \tag{0.11}$$

représentant le ratio entre la moyenne temporelle et la moyenne d'ensemble.

On représente dans la figure (0.9), les résultats obtenus pour les deux paramètres EB et ϵB.

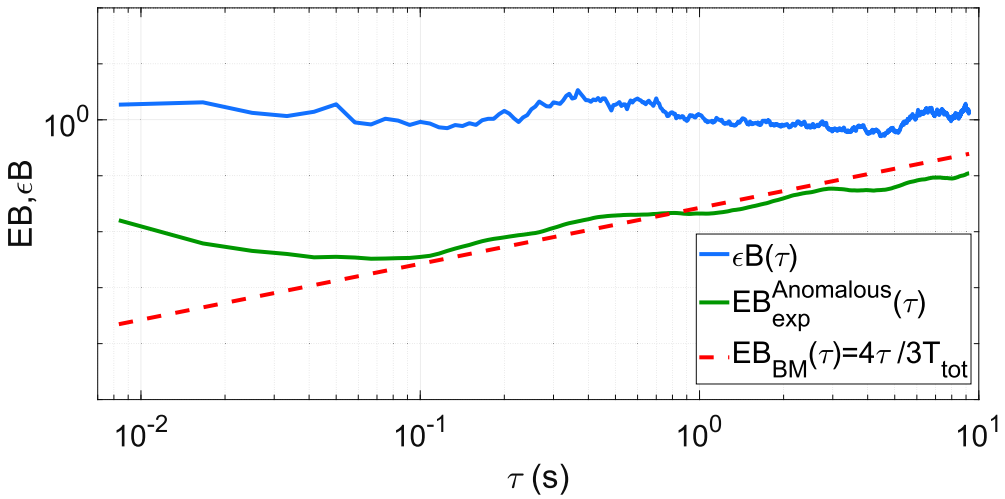

Figure 0.9 – Paramètres ergodiques en fonction du décalage temporel.

Malgré la TAMSD sous-diffusive, les distributions des déplacements sont Gaussiennes et l'on n'observe pas de violation de l'hypothèse ergodique.

Ce résultat est intéressant en soit, sachant que les descriptions théoriques de la diffusion anormale s'accompagnent soit d'une distribution non Gaussienne, soit d'une violation de l'hypothèse ergodique, soit des deux à la fois. Dans notre cas, on observe une diffusion anormale, Gaussienne et ergodique.

Dans cette thèse, nous avons exploité la richesse dynamique d'une suspension colloïdale pour (i) mesurer des forces optiques faibles et (ii) mener des études fondamentales sur les effets convectifs et les diffusions anormales.

A travers les quelques exemples de dynamiques spécifiques que nous avons caractérisées, notre travail cherche à montrer l'intérêt des ensembles colloïdaux pour ce type d'études, où des techniques optiques de détection simples mais précises permettent d'extraire les informations quantitatives pertinentes. Notre travail ouvre des perspectives intéressantes :

D'une part, dans le contexte des mesures de champ de forces optiques, où l'on peut imaginer reconstruire des champs de force complexes en utilisant des modes optiques spécifiques (exemple des vortex optiques, les champs optiques chiraux, . . .).

D'autre part, les mesures de diffusions anormales appellent à un travail théorique pour modéliser, dans le point de vue de Langevin, les évolutions sous-diffusives mesurées. Ce contexte de la description théorique des mouvements browniens anormaux est aujourd'hui en plein essor [6], et nos résultats expérimentaux apportent dans ce domaine d'étude d'autres exemples dont il faudra comprendre la structure.

NOTATION AND CHARACTERISTIC VALUES

Table 0.1 – Notations and characteristic values.

Quantity	**Notation**	**Equation**	**Typical value**[1]
Particles radius	R	$R = d/2$	0,5 µm (Ps)
Density of the particle	ρ		1,04 g/m^3 (Ps)
Particle mass	m	$m = \frac{4}{3}\pi R^3 \rho$	$5,5.10^{-13}$g
Dynamic Viscosity	η		10^{-3} Pa.s
Dragg coefficient	γ	$\gamma = 6\pi\eta R$	$9,42.10^{-6}$µm
Thermal Energy	$k_B T$		$4,11.10^{-21}$ J
Diffusion coefficient	D	$\frac{k_B T}{\gamma}$	0,436 $\mu m^2/s$
Number of displacement for the i^{th} trajectory	N_i		1200 at least
Number of trajectories	N_T		50
Number of all the displacement	N_t	$\sum_i^{N_T} N_i$	180 k and 600 k
Time between two frames	Δt	$\frac{1}{fps^2}$	$\frac{1}{120}$
Measurement time	t_{mes}	$N_t \Delta t$	1,5 ks and 5 ks
Sample mean	$\overline{\Delta X}$	$\frac{1}{N_i} \sum_i^{N_T} \Delta X_i$	
Sample variance $Var\{\overline{\Delta X}\}$	$\sigma^2_{\overline{\Delta X}}$	$\frac{1}{N_i - 1} \sum_i^{N_T} (\Delta X_i - \overline{\Delta X})^2$	$\sigma^2_{\overline{\Delta X}} = 2D_x \Delta t$
Sample standard deviation	$\sigma_{\overline{\Delta X}}$	$\sqrt{Var\{\overline{\Delta X}\}}$	
Sample standard error of the mean	$SE\{\overline{\Delta X}\}$	$\frac{\sigma_{\overline{\Delta X}}}{\sqrt{N_i}}$	
Sample standard error of the variance	$SE\{\sigma^2_{\overline{\Delta X}}\}$	$\sigma^2_{\overline{\Delta X}} \sqrt{\frac{2}{N_i - 1}}$	

1

INTRODUCTION

That light can exert mechanical pressure on irradiated objects, this is one of the central predictions that J.C. Maxwell formulated in his 1873 Treatise [7]. Together with the existence of propagation of electromagnetic waves, the confirmation of this prediction has motivated few experimentalists to set up the appropriate experiments in order to reveal this so-called « radiation pressure ». P. Lebedev, former PhD student of A. Kundt at the then-German University of Strasbourg, was the first to be able to conduct successful experiments that confirmed, in all its main aspects, Maxwell's prediction [8]. Since, then, optical radiation pressure has been exploited at the level of micron and nano-scaled objects. In this context, the pioneering work of Ashkin on the possibility to « tweeze » tiny objects using light led to the development of optical tweezers as powerful non-invasive tools in the fields of biology and physics [9]. During the last three decades, optical tweezers performances have been improved constantly, in order to be able to manipulate small objects such as nanoparticles and bio- molecules [10, 11].

Essentially, optical tweezers are intensively used [12] to probe, manipulate and characterize the dynamical properties of small dielectric objects ranging from few nanometres to few microns. For example, the force extension relation for a single DNA molecule was measured [13] by fixing one end to a glass substrate and the other end to a 520 nm particle trapped using an optical interferometric trap.

More recently, our group, in collaboration with the group of D.J. Norris, at EH–Zurich, has demonstrated the possibility to trap single chiral colloidal object and to perform simultaneously in situ chiral recognition protocols [14]. This capacity was achieved by exploiting the versatility of the strategy of optical tweezing as a general experimental scheme. The 2018 Nobel Prize in Physics is reminding us that the importance of this tool from a broad and multidisciplinary point of view.

Recently, new aspects and properties associated with radiation pressure have emerged in the context of nano-optics. Here, the possibility to excite, control and propagate inhomogeneous electromagnetic fields with complex beam topologies lead to a great variety of optical force effects, ranging from pulling forces [15] to chiral radiation pressure [16–18].

In this manuscript, we present our effort to propose micron-scaled colloidal particles as efficient probes of radiation pressure, with the potential to spatially resolve the topological signatures of these new types of optical forces. Following previous demonstrations made in our group on the capacity of metallic colloids to map complex plasmonic band structures through the measure of radiation pressure [3, 19], we investigate in more details here the relevance of exploiting collective Brownian motion in resolving radiation pressure signals.

In this introduction therefore, we will shortly introduce what Brownian motion is. We will discuss in details in the manuscript why and how the stochastic character of Brownian motion can be exploited in the context of weak force measurements. Then, we will briefly describe the type of colloidal assemblies we have been working with. Our colloidal systems obey a priori to simple behaviors, but, as it will be discussed below, it is not obvious to use a colloidal system as a simple meter that can yield reproducible results. How to control and ensure reproducibility using an ensemble of colloidal particles has been a central challenge of the work presented here.

1.1 AN INTRODUCTION ON BROWNIAN MOTION

A short introduction, alongside with the basic statistical properties of Brownian motion are given.

The motion of particles, with a size few orders of magnitude larger than the size of the surrounding solvent molecules but still invisible by naked eye, is random and caused by the incessant collisions between the molecules of the solvent and the wall boundary of the particle. The first to analyse precautiously such motion is Robert Brown in 1828 [20], when he observed under the microscope the perpetual jiggling of pollen grains of different species suspended in water. This incessant jiggling causes the fluctuations of positional degrees of freedom, in such a way that the variables describing the mechanical and dynamical evolutions of the system are no longer deterministic but have become stochastic.

From the theoretical point of view, Einstein, in 1905 *annus mirabilis*, proposed in his paper [21] a solution to the problem of Brownian motion based on the kinetic theory of gas. Einstein derived the diffusion equation for a Brownian particle and gave a relation between the Mean Squared Displacement (MSD) and the diffusion coefficient of the particle immersed in the thermal fluctuations mediated by the solvent. Contemporary to Einstein, Smoluchowski [22, 23] derived the diffusion equation for a Brownian particle under an external force field using combinatory analysis leading to the same results as Einstein[21]. Figure (1.1) displays an example of such Brownian motion.

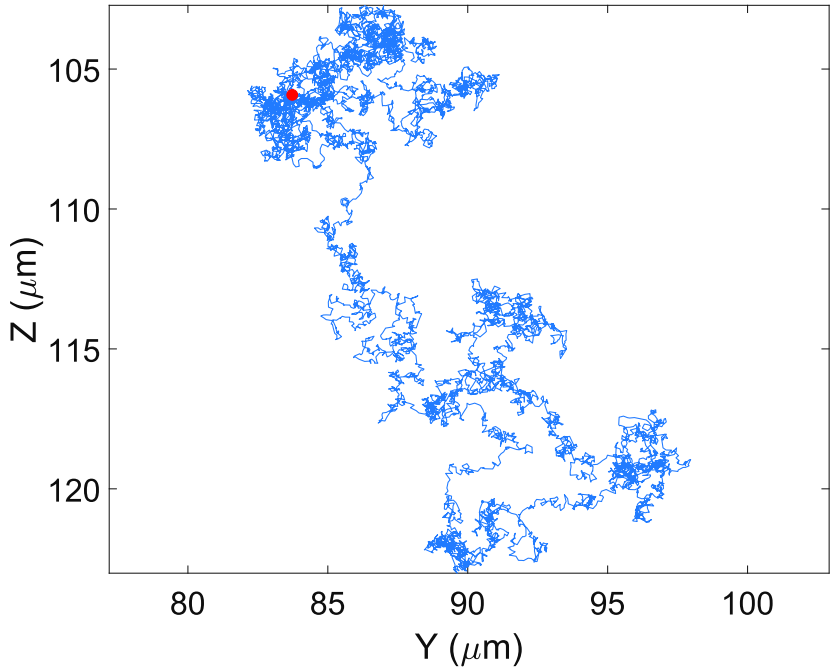

Figure 1.1 – Recorded Brownian trajectory of a Melamine bead of radius $R = 470$ nm, immersed in water at room temperature. The "jiggling" of the particle is caused by thermal fluctuations. The red dot represents the initial position.

The probability $\mathcal{P}(x,t)$ to find a Brownian particle in x at time t follows the diffusion equation :

$$\frac{\partial \mathcal{P}(x,t)}{\partial t} = D_x \frac{\partial^2 \mathcal{P}(x,t)}{\partial x^2}, \tag{1.1}$$

with D_x is the 1D diffusion coefficient. The solution of the equation assuming that at t=0 the particle starts from x=0 is the Gaussian distribution :

$$\mathcal{P}(x,t) = \frac{1}{\sqrt{4\pi D t}} e^{-\frac{x^2}{4Dt}}, \tag{1.2}$$

Taking the first moment m_1 of the distribution gives the expected value of the stochastic variable X, the positions of the particle, which is:

$$m_1 = E[X] = \int_\omega xP(x,t)\,dx, \tag{1.3}$$

with ω is the ensemble of all the positions that X can take . For a Brownian particle, this average is zero, meaning that the particle explore with an equal probability "positive" and "negative" displacement regions. In contrast, the second moment m_2 is non zero and given by :

$$m_2 = E[X^2] = \int_\omega x^2P(x,t)\,dx, \tag{1.4}$$

which defines, for Brownian particle, the MSD:

$$\overline{\delta x^2(t)} = m_2 = 2Dt, \tag{1.5}$$

expressing the relationship between the mean squared displacement $\overline{\delta x^2(t)}$ of the particle and time. The proportionality coefficient is the diffusion coefficient D given for a spherical particle of a radius R, diffusing in a fluid of viscosity η, by Stokes-Einstein equation :

$$D = \frac{k_B T}{6\pi\eta R}, \tag{1.6}$$

where k_B is Boltzmann constant and T the equilibrium temperature of the fluid. In 1908 Perrin[24] measured the Avogadro constant N_A by studying the Brownian motion of an emulsion of mastic diffusing in water.
In the same year Langevin [25] proposed a mechanistic description of Brownian motion. Langevin equation will be described in details in chapter III. We will also describe the tools that can be used in order to extact, from the stochastic behavior of Brownian motion, the observables that can provide a quantitative measurement of the strength of the external force field within which the Brownian motion can be performed. This approach has first been introduced by Uhlenbeck and Ornstein in their well-known paper [26].

1.2 COLLOIDAL SUSPENSIONS

A colloidal suspensions is a heterogeneous mixture composed of solid particles dispersed in a fluid. Such a system constitutes a toy system for probing fundamental interactions [27, 28] and understanding the

underlying complex dynamics in biological systems [29].

The stability of colloidal suspension is crucial, because aggregation can introduce inhomogeneity of the size of the dispersion and eventually precipitation of the colloidal assembly that turn the ensemble into a non-exploitable phase. In general, stabilization, a delicate task, is done by using electrostatic charges and thereby balancing unwanted force effects that can destabilize the assembly.

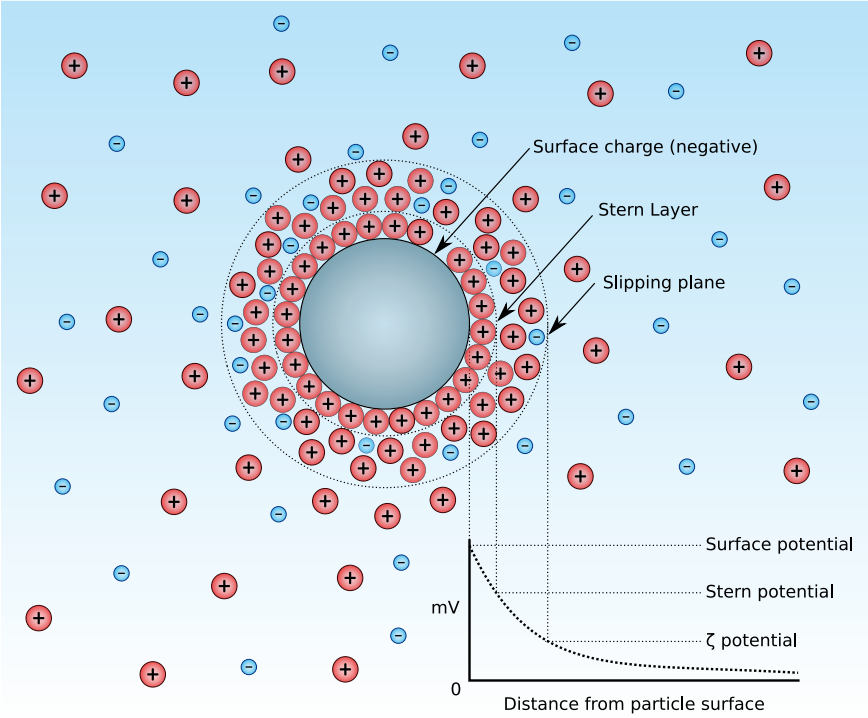

Figure 1.2 – Schematic view of the electric double layer mechanisms for charge stabilization of colloidal particles. The negatively charged particle attract positive counter ions, defining then the Stern layer. Furthermore, when the particle moves the surrounding fluid is displaced, which defines the slipping plane and the corresponding Zeta potential as the value of the electric potential at the boundaries of this slipping plane. The electric potential drop to zero as we move from the surface of the charged particle. Source : Modified and converted to SVG by Mjones1984. Original work by Larryisgood. — Modified image based upon http://en.wikipedia.org/wiki/File:Zeta_Potential_for_a_particle_in_dispersion_medium.png by Larryisgood., CC BY-SA 3.0, https://commons.wikimedia.org/w/index.php?curid=18238739

In our colloidal systems, the main source of aggregation stems from Van der Waals attractive forces. Such forces can be neutralized by Coulomb repulsive forces between two charged particles. The zeta potential is defined as the value of the electric potential at the slipping plan presented in figure (1.2). The important parameter in charge stabilization is the Zeta potential, which gives the strength of the electrostatic repulsion with

respect to attractive interactions, larger value of Zeta potential leading to more stable colloidal particles.

The colloidal particles used in this manuscript are charge-stabilized, and highly diluted with a volume fraction $\phi = 10^{-5}$. Melamine and Polystyrene particles are purchased from MicroParticles Gmbh, with a low size polydispersity (with a coefficient of variation C.V.<3%) and a Debye screening length in the order of 0.5 μm.

1.3 DYNAMICAL BEHAVIOR OF COLLOIDAL PARTICLES UNDER EXTERNAL FORCE FIELDS

Controlling the dynamics of a particles by exotic light fields is an emerging field of research.

Recently, "pulling" optical forces have been demonstrated in the absence of intensity gradient [30, 31]. This counter intuitive "pulling" force emerge from the increasing of the forward scattering along the direction of the incident beam.

Figure (1.3) displays an example of pulling force demonstration. A gradient-free optical beam is used to illuminate small droplets of dodecan, trapped in water-air interface, with a power $P \sim 35\ \mu W/\mu m^2$. We can see clearly that the particles localized in the center of the beam are "pulled" in the opposite direction of propagation of the beam. We can see clearly that the pulling in localised at the center of the illumination spot confirming that the origin of this effect is indeed the irradiation laser.

Opticaly efficient mass transport is also demonstrated in an other experiment [32]. In this experiment optically induced flow is used to efficiently move the particles. The motion of the particles under the action of a constant optical force, drag the fluid creating then a flow that increase the velocity of the ensemble. This enhancement is understood from hydrodynamical interaction point of view.

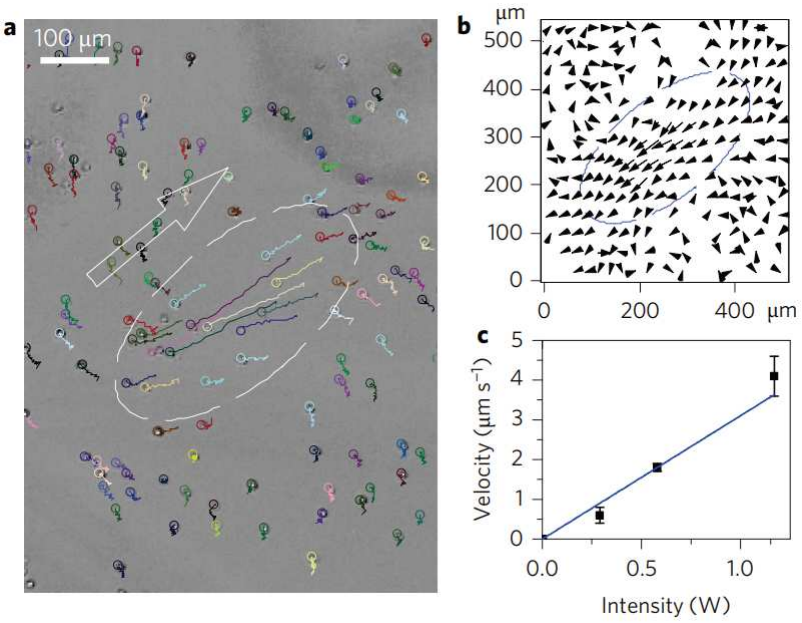

Figure 1.3 – Pulling optical force on oil droplet localized at the water-air interface. a) represents the detected trajectories of the droplets during 45 s, the small circles are the final positions and the dashed ellipsoid represents the illumination spot. The arrow is the direction of propagation of the light beam. b) the corresponding force induced mean velocities close to the beam center. The arrow lengths are related to the average velocities. c) The mean velocity at different laser power and the errorbars are the standard deviation around the mean value. This figure is directly taken from [31].

Actually, the applied force field induce a particle velocity V_i, defined as:

$$\vec{V}_i = \sum \mu_{ij} \vec{F}_j, \tag{1.7}$$

with F_j is the applied force on the particle j. The summation is done over all the particles j that "feel" the force field. The hydrodynamic interaction is taken into account *via* Oseen tensor $\mu_{ij} = \mu(r_i - r_j)$ for two interacting colloidal particles i and j localised at r_i and r_j, defined as :

$$\mu_{ii} = \frac{1}{6\pi\eta a}\mathbb{I}, \quad \mu_{ij} = \frac{1}{8\pi\eta R_{ij}}\left(\mathbb{I} + \hat{R}_{ij}\hat{R}_{ij}\right), \tag{1.8}$$

where :

- a is the radius of the particles, supposed mono-dispersed,
- η is the dynamic viscosity of the surrounding fluid,
- R_{ij} is the distance between the particles i and i, $\hat{R}_{ij}$ is the unit vector in a direction from particle j to particle i,
- $\mathbb{I}$ is a unitary matrix.

In the case of a single particle we recover the Stokes force : $F_S = \gamma V$. From equation (1.7), using a uniform force field one can increase significantly the velocity of the particles, because the summation is done over terms that sum up with the same sign.

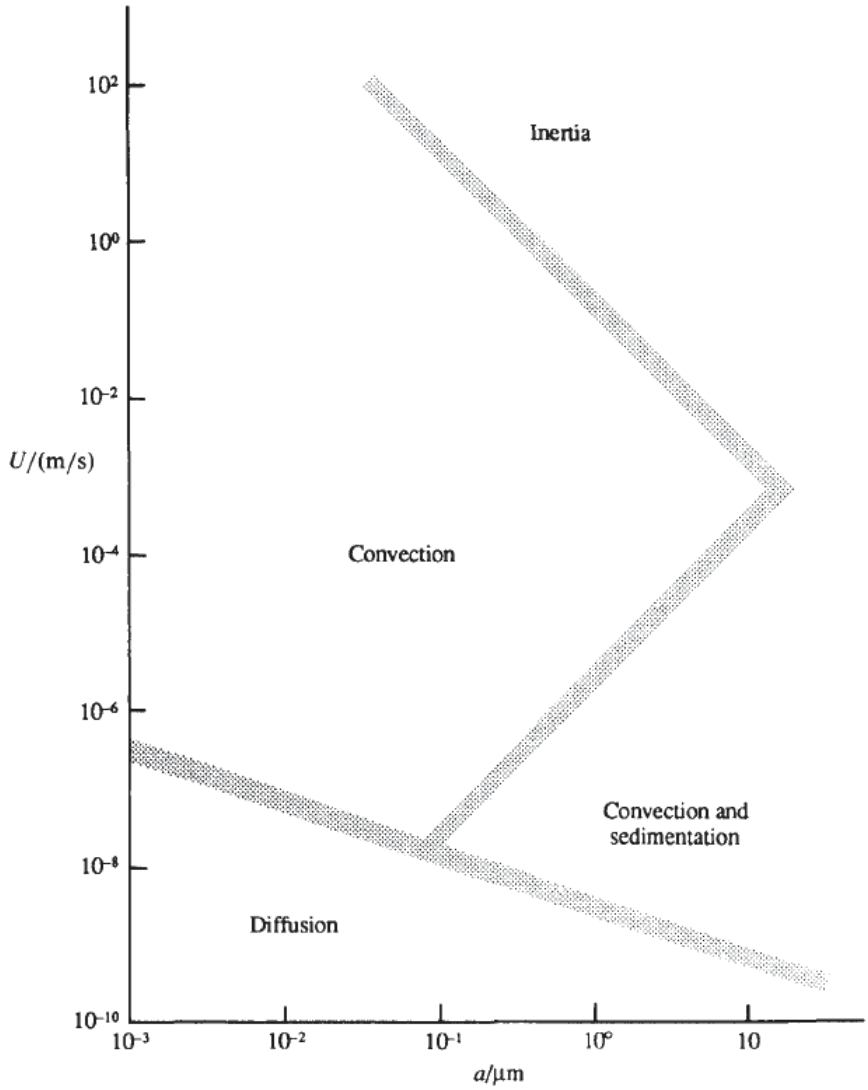

Figure 1.4 – Dominant mechanism in colloidal suspensions depending on the size a and the velocity U of the colloidal particle. In our experiments the typical velocities are in the order of $U \sim 1\ \mu ms^{-1}$ and the particle size is $a \sim 0.5\ \mu m$. This figure is taken from [33].

The system constituted by an ensemble of colloidal suspension appears as an interesting system to exploit in the context of optically induced motional dynamics [3, 19, 30–32, 34].

But when dealing with such assemblies, it will be very important to keep in mind that they constitute by definition a type of "complex system" at the level of which the tools of non-equilibrium statistical physics are necessary. The example of sedimentation is in this regard

interesting to discuss. Constituting the realization of a non-equilibrium steady state, sedimentation, despite its apparent simplicity, is accompanied by very complex dynamics. This is essentially related to the fact that a colloidal dispersion is, by construction an heterogeneous system, with local fluctuations of concentrations. Such fluctuations can alter throughout the volume of the dispersion the sedimentation dynamics via hydrodynamic interactions (as discussed above) and local advective effects [34]. Figure (1.4) summarizes the different mechanisms involved when studying the dynamical behaviour of colloidal suspensions, and strikingly reveals the richness and complexity of colloidal systems.

Optical micro manipulation is more efficient at low Reynolds number which is the ratio between the inertial and the viscous forces. The applications of such mechanical light-matter interaction are tremendous in physics, chemistry and biology. This type on interaction is that small that the effects are noticeable only at the micro and nano scales. Indeed the development of lasers and colloidal science permits the study of such small optical forces.

The intrinsec stochastic character of colloidal suspensions, leads to the emergence of stochastic thermodynamics [35], which combines statistical mechanics and stochastic variables. The work presented in this manuscript lies within this context.

Our experimental apparatus consists of a nano-optics setup coupled to a video microscope. The typical spatial and temporal resolutions in our experiments are $\Delta r = 20$ nm and $\Delta t = 8.3$ms, respectively. The Single Particle Tracking (SPT) methods enable the acquisition of Brownian trajectories for colloidal particles suspended in water at room temperature and illuminated by a collimated Gaussian beam. Nevertheless, the irradiating laser, in addition to the mechanical pushing of the particle, slightly heats the fluid and induces a convective flow, changing then the collective dynamics of the colloidal assembly. Furthermore, the laser beam is prepared in such a way that the radiation pressure applied at the level of a single particle is close to the thermal stochastic force limit which is the mean thermal force applied on the particle due to thermal fluctuations. An other aspect of colloidal suspension is accessible with our experiment which is the observation of rare events of anomalous diffusion.

This manuscript is organized as follows :

- In the **second chapter**, we describe the optical system built in the laboratory. From the video tracks, recorded by our dark field microscope, we extract the Brownian trajectories. We analyse then this trajectories by exploiting the probability density function and the mean squared displacement.

- In the **third chapter**, we use the methods presented in the first chapter in order to quantify the dynamics of our Brownian particles. We then show the existence of three regimes of dynamics depending on the injected laser power into the system. We propose a model to predict the convective velocity due to water absorption of the illuminating laser radiation. This model connect Navier-Stokes and Fourier's equations to estimate this induced convective velocity. We clearly observe a compensation of the sedimentation of the particles by the convectively induced flow for a given laser power.

- In the **fourth chapter**, we counter-balance the injected power to exert weak radiation pressure forces on the colloidal assembly. We demonstrate, in the context of Brownian motion, the stationary ergodic aspects of the detected displacements. Indeed, in addition to noise stability, these aspects are crucial in the "concatenation" strategy we use in order to decrease the uncertainties of our measurements. Furthermore, we present a method for reconstructing the applied force field profile via the Brownian trajectories of the particles diffusing within the extension of the laser beam.

- In the **fifth chapter**, we report our observation of anomalous diffusion. we exploit our dark field microscope in order to identify the hindered motion of targeted particles. The trajectories of such particles are anomalous from the mean squared displacement point of view, but remain ergodic and Gaussian. This observations do not fit any known model, opening then the door for theoretical investigations. Unfortunately, this exercise is not done in this work.

2

SINGLE PARTICLE TRACKING IN COLLOIDAL SUSPENSIONS

Since the last couple of decades, digital video microscopy has developed as a powerful tool to study the fluctuating dynamics of micron-scaled objects. With typical temporal resolution of the order of few milliseconds and spatial resolution of about tens nanometres, Single Particle Tracking (SPT) as implemented for instance by Crocker and Grier[36] has allowed intensive studies of the dynamics of biological systems such as : cell membranes [37], biomolecules [38],...

In this manuscript, we have used SPT to analyse the dynamics by tracking micro particles suspended in water at room temperature and subjected to radiation pressure optical force. Our task in particular has been to adapt such video microscopy methods to the measure of weak radiation pressure forces.

This first chapter describes the setup built in our laboratory on which we acquired, through SPT, Brownian trajectories of colloidal particles under the external force fields both of gravity and radiation pressure. The features of the dark field microscope that we built are described in detail. The core of our methodology in the statistical treatment of the recorded trajectories is also presented.

2.1 AN OPTICAL MICROSCOPE FOR COLLOIDAL TRACKING AND OPTICAL FORCE MEASUREMENTS

The optical setup used to study the dynamics of colloidal particles is presented in this section. Our home-built experimental setup for single particle tracking is described including the Gaussian beam optics from which our dark field microscopy proceeds.

2.1.1 *Experimental Setup*

The experimental setup consists of a spectroscopic cell, filled with water within which colloidal particles are dispersed. A laser beam is sent through the cell and a microscope objective, placed transversally with respect to the beam, allows imaging the light either scattered by the colloidal particles diffusing inside the beam extension or the photo luminescence induced by the laser beam when using fluorescent doped particles. The experiment is sketched in figure (2.1).

The illumination beam is from a pigtailed Laser Diode with a single mode fiber and emission wavelength $\lambda = 637$ nm, coupled to the forward focal plane of an inverted Newport objective 10X and NA =0.25 corrected to infinity, in order to work in collimated beam condition. The beam is linearly polarized with a nano particle linear film polarizer (LP) with an extinction ratio of 1:1000. The beam then passes through a polarizing beam splitter (PBS) which cross-polarizes the transmitted vs reflected beams. Before the PBS, a half wave plate (HWP) is used to finely tune the injected laser power in each arm. This is done by rotating the linear polarisation of the incoming beam. Hence, if the input polarization before the PBS is set at 45^o, the powers P_1 and P_2 injected in the two beams are equal. The two beams are then weakly focused by two identical convergent lenses (L1) and (L2). The two mirrors M1 and M2 are adjusted in such a way that, at the level of the sample, the two beams are precisely superimposed.

The (L1,L2) focal length $f = 400$ mm is choosen so that the observed area of the sample lies within the Rayleigh range of the focused Gaussian beams. The experimental setup can be used in two configurations :

- Single-beam configuration : all the available laser power P is injected in one arm by matching the input polarization before the PBS to the polarization of the arm of interest.

- Counter propagating two-beam configuration : the injected power is set by the input polarization. As mentioned before, for an input polarization of 45^o, the powers P_1 and P_2 in the two arms are equal. The linear polarizations of the beams are set to be orthogonal in order to avoid interferences inside the cell.

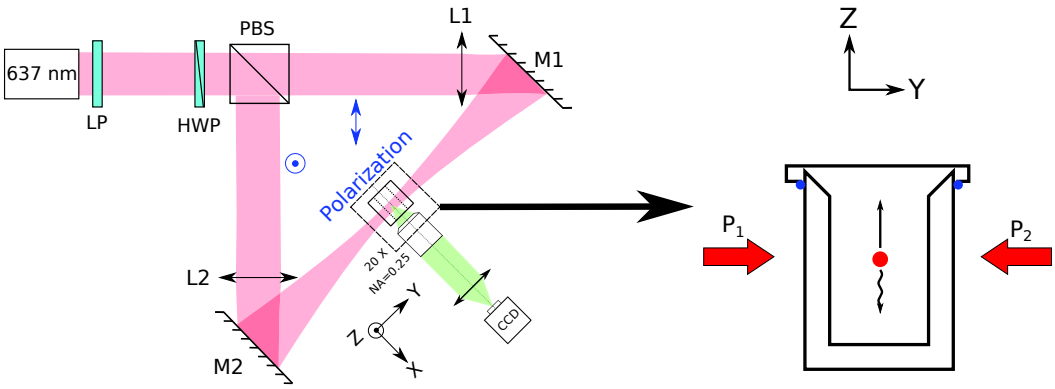

Figure 2.1 – Scheme of our optical setup. The left hand side shows the different optical components involved. A HWP is placed before the PBS to tune the injected power in each arm. The converging lenses (L1) and (L2) have the same focal length f=400mm. The two mirrors (M1) and (M2) are aligned such that the two waists of the two cross polarized beams are superimposed in the middle of the fluidic cell. The detection part will be detailed in the following section. The right panel represents a schematic view of the fluidic cell in the (YZ) focal plane of our imaging system. The fluidic cell is filled with a diluted colloidal suspension in water room temperature. On one hand, if non doped micro particles are used, the collected photons scattered by the particles are collected by the objective. One the other hand when doped micro-particles are used, the objective collects the photo-luminescent light. The dynamics are the same either the used particles are doped or not. The sample preparation is described in the main text.

Each configuration will be exploited in the context of small optical forces measurements, as discussed throughout the manuscript.

2.1.2 *Gaussian beam optics*

The intensity profile $\mathcal{I}(r,t)$ of the laser beam is Gaussian with:

$$\mathcal{I}(r,t) = I_0 \left(\frac{w_0}{w(Y)}\right) \exp\left(-\frac{2r^2}{w^2(Y)}\right), \tag{2.1}$$

where

- I_0 is the peak intensity,
- w_0 is the waist of the beam,
- $w(Y)$ is the radius of the beam at the a position Y :

$$w(Y) = w_0 \sqrt{1 + \left(\frac{Y}{Y_R}\right)^2},$$

with $Y_R = \frac{\pi w_0}{\lambda}$ is the Rayleigh range,

- $r = \sqrt{X^2 + Z^2}$ is the radial position from the center of the beam (optical axis).

The parameters are presented in figure (2.2). Experimentally, we measure, with a power meter, the mean power of the beam defined as :

$$< P >= \int_0^{+\infty} \mathcal{I}(r,t) r dr d\theta = \frac{I_0 w_0^2 \pi}{2} = \frac{P_{max}}{2}, \tag{2.2}$$

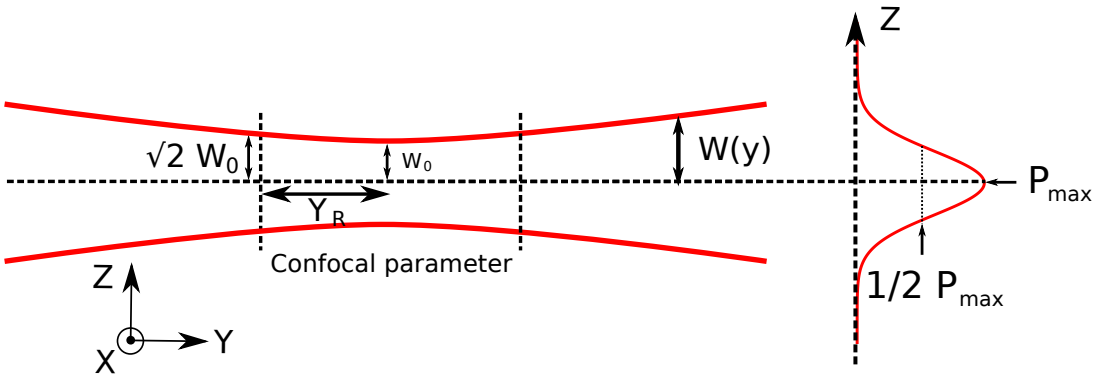

Figure 2.2 – Gaussian beam parameters : w_0 the beam waist is the transverse extension of the beam at the focus. The beam width at the position y is : $w(y) = w_0\sqrt{1+\left(\frac{y}{Y_R}\right)^2}$, where $Y_R = \frac{\pi w_0^2}{\lambda}$ is the Rayleigh range which is the distance over which the beam size is increased by a factor of $\sqrt{2}$. The right hand side panel represents a sketch of the power profile of a Gaussian beam : the maximum power is in the center of the beam, on the optical axis. In our experimental conditions, using a focal length of 400 mm, $Y_R \sim 12mm$

The important parameter here is the Rayleigh range (or length) of the beam. As discussed below, an imaging field of view smaller than the Rayleigh range will essentially probe, from both sides of the waist, a "collimated" laser beam, with a practically a planar phase front. This aspect plays an important role in chapter three for our optical force measurements.

2.2 COLLOIDAL SUSPENSIONS IN A FLUIDIC CELL

Colloidal particles are used throughout this manuscript as force probes in our experiments. We work with charge stabilized colloidal particles, commercially available at MicroParticles GmbH. The particles are charge-stabilized in order to avoid aggregation. Our samples consist

of spherical micro-particles dispersed in water. We use a spectroscopic cell (see figure (2.3)) filled with micro-particles made of Melamine or polystyrene. The dispersion in size of the particles is 5%, as determined by the manufacturer.

We choose a relatively low concentration of particles for two main reasons :

- first in order to avoid particle particle interaction[1];
- then to have enough statistics to estimate Brownian parameters with sufficiently good confidence levels (see below).

The volume fraction defined as follows :

$$\phi = \frac{V_p}{V_t}, \tag{2.3}$$

where V_p is the volume of all the particles in the cell, and V_t is the total volume of water including the volume occupied by the particles. In our experiments $\phi = 10^{-5}$ so that in practice for a typical measurement there is at least ten particles in the field of view of our microscope (cf. figure (2.4)).

The sample is then sealed by a home made cup formed by a glass slide and a PDMS mask. In addition, to improve the sealing, we use vacuum grease to avoid any evaporation of the water and any induced flow. The seal has turned out to be a crucial element for our experiments, playing a central role for the reproducibility of our data.

The sample is left for 1 hour on the sample holder before starting any SPT recording, in order to let the particles reach the steady state sedimentation. Finally, we ground the cell to remove any electrostatic charges on the surface of sample. This experimental protocol has been fixed and carefully repeated for each new experiment. Before starting any experiment, we verify that we are working in a laminar flow regime along the Z axis by recording the dynamics of the particles for 1 min and verifying that the particles stays in the YZ plane. Any failure on the seal, electrostatic grounding, and relaxed sedimentation in the laminar regime led to erratic and non reproducible results.

1 at least most of them. We will however discuss in chapter four a few observations induced by such, rare, interactions.

We present is figure (2.3) a sketch of the sample. There is no boundary wall effect because the Field Of View of the microscope is much smaller than the distance between the walls and the sample cell.

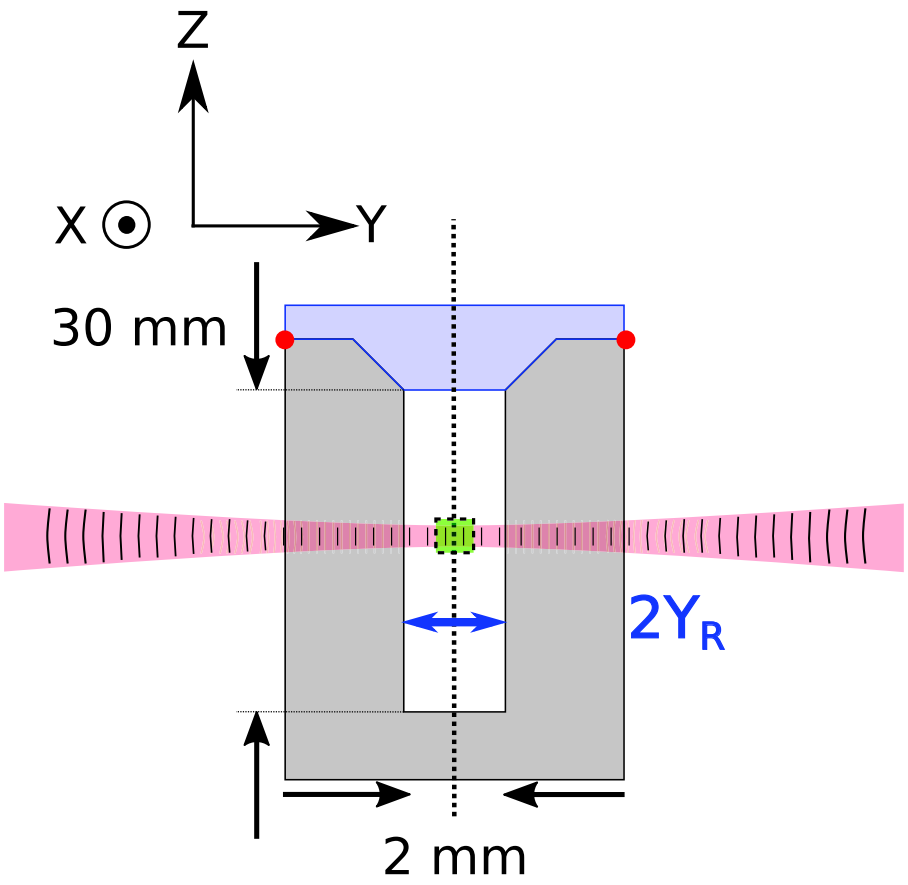

Figure 2.3 – Sketch of the sample cell. The cell is a "spectroscopic cell" (purchased at Hellma Analytics) made of optical glass with four windows. The dimensions are : height 45 mm, width 12.5 mm and depth 12.5 mm. The dimensions inside of the cuvette are 30 mm height, 2 mm width and 10 mm depth. The red dots represent the vacuum grease sealing. The blue segment shows the confocal parameter. F.O.V is the field of view of the dark field microscope.

2.3 DARK FIELD MICROSCOPY AND SPATIAL CALIBRATION

Our dark field microscope is designed in such a way as to collect the light scattered by spherical particles (or emitted by doped-fluorescent particles) when passing within the illumination laser beam. The collection is done in a direction perpendicular to the optical axis (hensce 'dark field') using an imaging objective Olympus 20X, NA = 0.25 with a very long working distance 26.5 mm.

An example of a recorded image is displayed in figure (2.4) : the image is diffraction-limited, each particle being seen as an Airy spot. The field of view (FOV) is defined as the extension of the region observed by the microscope. In our experiments the dimensions of the FOV are 350µm x 250µm. We stress that the FOV is much smaller than the laser beam Rayleigh length evaluated to be 12 mm.

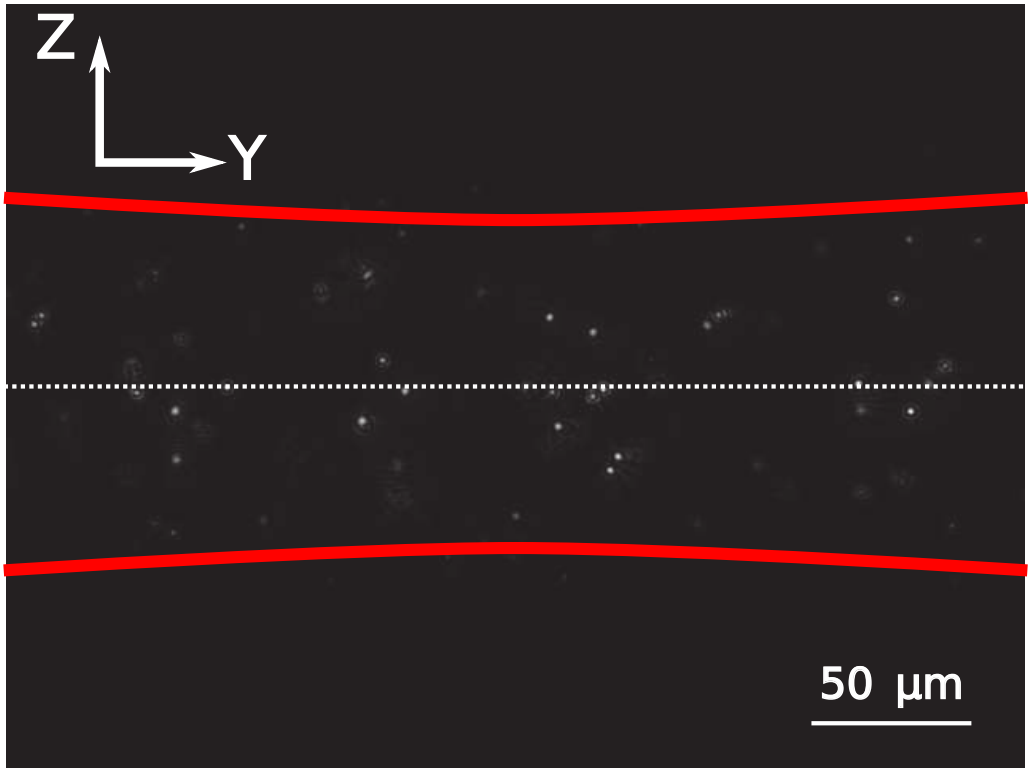

Figure 2.4 – Example of an image recorded by our dark field microscope. The red lines highlight the contour of the laser beam and the dashed line indicate the optical axis. Each spot is a diffraction limited image of one particle. The depth of field of our imaging system is 11.2µm. When the particle is leaving the focal volume, higher diffraction orders appear and the scattered intensity is reduced.

The theoretical (Y,Z) two-dimensional Point Spread Function (2D-PSF) is compared to the experimental recorded Airy spots. The theoretical 2D PSF is approximated by a Gaussian distribution [39] :

$$I(y,z) = I_0 \exp\left(-\frac{(y-y_0)^2+(z-z_0)^2}{2s_0^2}\right) \tag{2.4}$$

with (y_0, z_0) is the center of the PSF. I_0 is the peak intensity and depends on the brightness of the spot, the pixel size and the exposure time. The width of the distribution is given by s_0^2.

The results of the comparison are presented in figure (2.5).

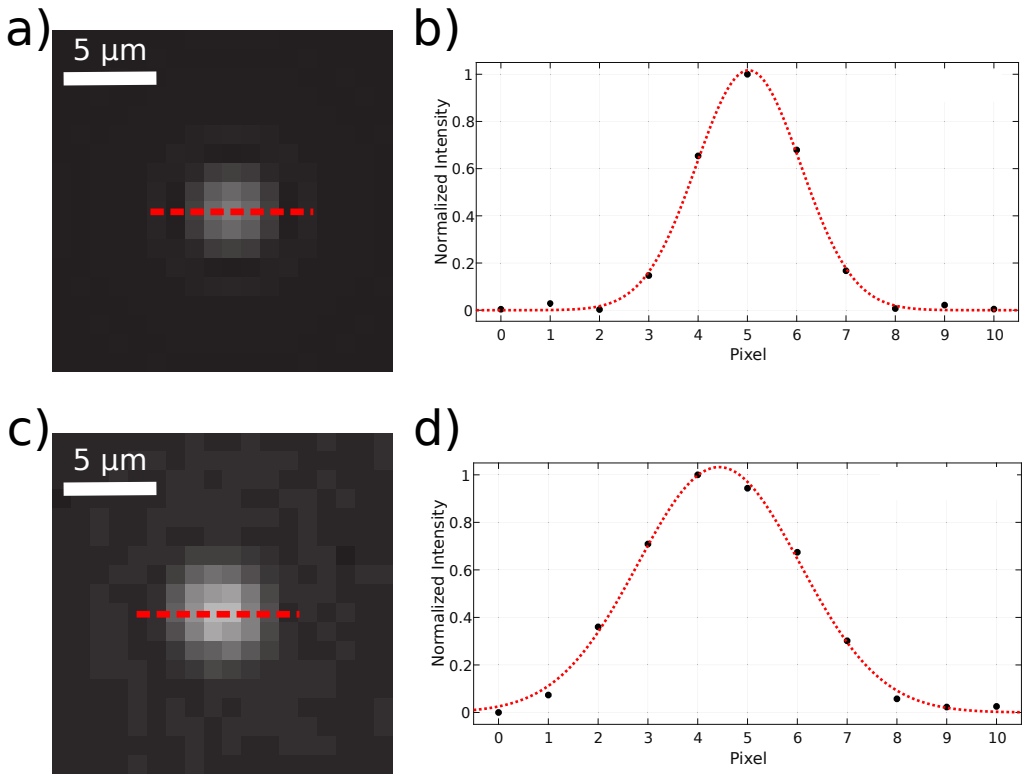

Figure 2.5 – Point Spread Function and corresponding cross cuts. Panel (a) shows the theoretical 2D-PSF calculated from the optical parameters of our imaging system. Panel c) displays the experimental diffraction limited image of one bead. The red dashed line is a cross cut and the corresponding profiles are presented in panel (b) and (d) where the black dots are the normalized intensity values in each pixel and the red discontinuous lines are the corresponding fit using the model represented in equation (2.4). The standard deviation of experimental spot in c) and d) are respectively : $s_0^{exp} = 621 \pm 75$nm and $s_0^{th} = 405 \pm 30$nm. The experimental profile is wider than the theoretical one because of the presence of noise. The corresponding Rayleigh resolution is: 2.95 pixel=1.5µm which defines the minimal resolvable distance between two spots.

The experimental profiles can be described using a Gaussian PSF, with a width however larger than expected due to inevitable noise in the recorded image.

2.3.1 *Pixel size calibration*

In order to perform the spatial calibration of our imaging system, a resolution target is used. The target consists of vertical and horizontal lines with known separation length. Figure (2.6) displays an image of such a the target used to quantify the pixel size of our imaging system.

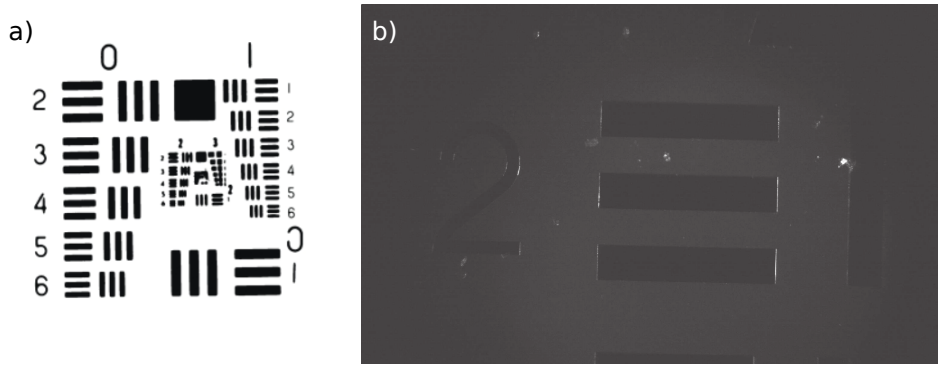

Figure 2.6 – Calibration target used for the determination of the pixel size of our imaging system. Panel (a) shows the calibration target and in panel (b) an image recorded by the microscope is displayed.

From the target data sheet, we know exactly the physical size of each segment. After imaging the target with our microscope, we can match the known physical length with the number of pixel. This allows us to extract the size of one pixel. Using this method, we measure a pixel size $p_s = 540\text{nm} \pm 5\text{nm}$. The error is determined by repeating the measurement of the pixel size several times.

Now that we know the experimental pixel size of our imaging system, we will describe how we acquire the trajectories of the colloidal particles and how we measure the localisation errors of our microscope.

2.3.2 *Tracking the positions of the particles*

We here present the SPT methods used in this work. In order to record the trajectories of the particles we have implemented TrackMate[2], an open source plugin of ImageJ software. TrackMate offers a lot of flexibility for tracking particles through the possibility to write a Python program where different algorithms can be called, aimed at tracking the positions of the Airy spots associated with the particles imaged through the microscope.

The input parameters for the tracking are :

- the apparent diameter of each spot in pixel units;
- the threshold value which determines the minimum intensity for a spot to be considered as a particle diffusing in the focal volume of the microscope;
- the maximum displacement allowed between two successive frames for linking two detected spots.

The algorithm for particle tracking we adopt is the one first introduced by Cooker and Grier [36]. The first step of the algorithm is to find the centroid of each spot by performing a Gaussian fit of the spots. Then, the center of the fitted distribution is considered as the real position of the bead. The second step is to link the detected centroids between successive frames. The plugin is designed to use each PC processor to treat one image, hence permitting fast tracking. For example, for a video of 5 min the tracking software needs between 5 and 15 minutes to track and link the spots depending on the concentration of the colloids.

2.3.3 *Localisation errors*

The algorithmic determination of the position of the particle is accompanied by certain errors which depend on :

- the diffusion coefficient D of the particle,
- the exposure time t_E used to record the motion,
- the size of the PSF s_0.

There are two main sources of error in determining the positions of the particles [40] :

- static localisation error : the physical origin of the static error is the fluctuation in the number N of photon illuminating the particle, corresponding through the chain of detection to the fluctuations in the collected scattering intensity

$$\sigma_0 = \frac{a}{\sqrt{2\pi I_0}} = \frac{s_0}{\sqrt{N}} \tag{2.5}$$

  where :
  - a is the pixel size,
  - I_0 is the peak intensity recorded by the camera,
  - s_0 is the dimension of the PSF.

  We can measure σ_0 by tracking the trajectory of a fixed particle. The particle is fixed to the surface of a glass substrate by dispersing a droplet of diluted solution of water and micro-particles. After the evaporation of the water, the particles remain stuck to the surface due to electrostatic charges. The static localisation error is given by the standard deviation of the distribution of the detected positions. An

example of a tracked trajectory for an immobile particle is presented in figure (2.7). The measured static localisation uncertainty is 10 nm.

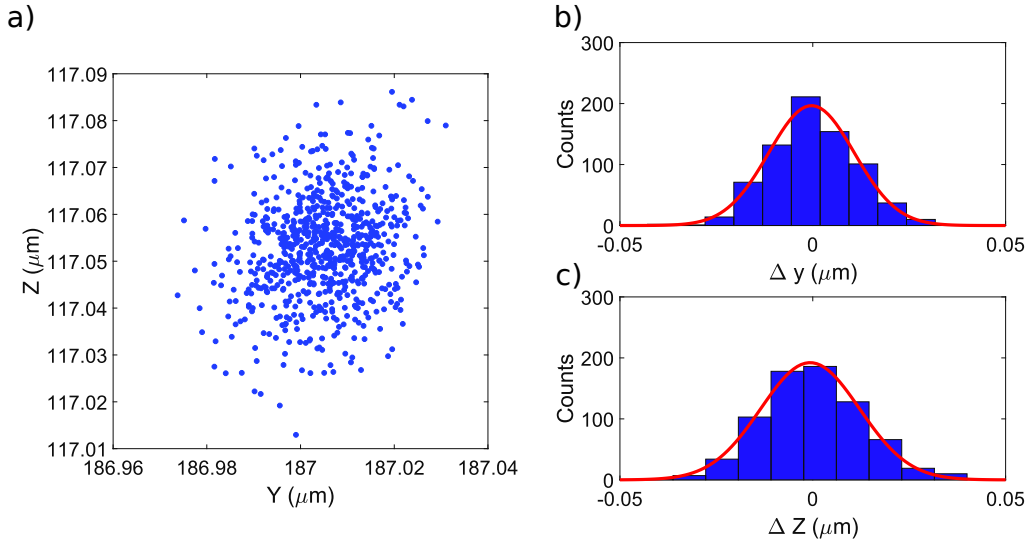

Figure 2.7 – (a) Tracked positions of a fixed bead. Panels (b) and (c) shows respectively the displacement histogram along Y and Z directions. The counts are the number of times that the displacement lies within the bin width which is in this case 7 nm. The localisation uncertainties are given by the width of the distribution : $\sigma_0^y = 8 \pm 1\text{nm}$ and $\sigma_0^z = 9 \pm 0.5\text{nm}$.

- dynamic localisation error : the finite exposure time over which the particle diffuses is a source of additional localisation error. This "dynamic" localisation error is defined as follows [40] :

$$\sigma = \sigma_0 \sqrt{1 + \frac{D_0 t_E}{s_0^2}}, \tag{2.6}$$

  - D_0 is the Stokes-Einstein diffusion coefficient,
  - t_E is the exposure time of the camera in the tracking process, in the order of few ms,
  - σ_0 is the static localisation error,
  - s_0 is the size of the PSF.

For slow diffusion or short exposure time : $D_0 t_E \ll s_0$, the error is dominated by the static error. Although when the diffusion of the particle is sufficiently high or large exposure time : $D_0 t_E \sim s_0$, the error is dominated by the diffusion. Using the adimensional reduced localisation error defined in [40] by :

$$x = \frac{\sigma^2}{D_0 \Delta t} \tag{2.7}$$

we evaluate that under our experimental conditions, $\frac{D_0 t_E}{s_0^2} \ll 1$. This implies that localization errors are dominated by σ_0, i.e. the static localisation error contribution.

In order to verify this experimentally, we track the motion of a particle fixed on a glass substrate. Then, we move with different steps the substrate using a piezo electric stage. The results for a step size of 50 nm are displayed figure (2.8) where we can clearly see that a displacement of 50 nm is well resolved by our microscope.

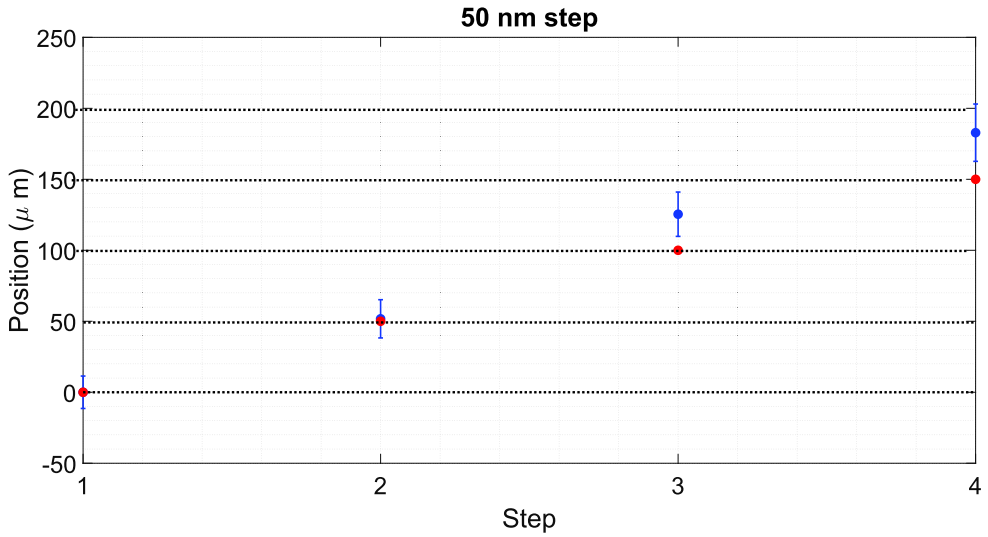

Figure 2.8 – Displacement resolution for 50 nm step. The error bars are the standard deviations around the mean position calculated from the ensemble of displacements. There is a good agreement between the real position and the detected one for the two first points. There is an issue for the two other measurements but the difference between the two detected positions and the two real position is the same, confirming that a displacement of 50 nm is well resolved by our microscope.

We look then for the minimal resolved displacement by setting a step size of 10 nm. Figure(2.9) displays the results for 10 nm step displacement.

The static localisation errors are in the order of 20 nm and as shown in figure (2.9) the error bars are basically in the order of $2\sigma_0$.

We can compare this results with the root mean square (rms) displacement of a particle diffusing in water at room temperature $:\sqrt{2D_0\Delta t} = 93\text{nm}$, which represents the typical displacement of a particle under the influence of thermal fluctuations. This displacement is of courses well resolved by our microscope.

This section allows us to conclude that our setup can resolve displacements in the order of 20 nm which is below the typical displacement of a particle diffusing under to thermal fluctuations.

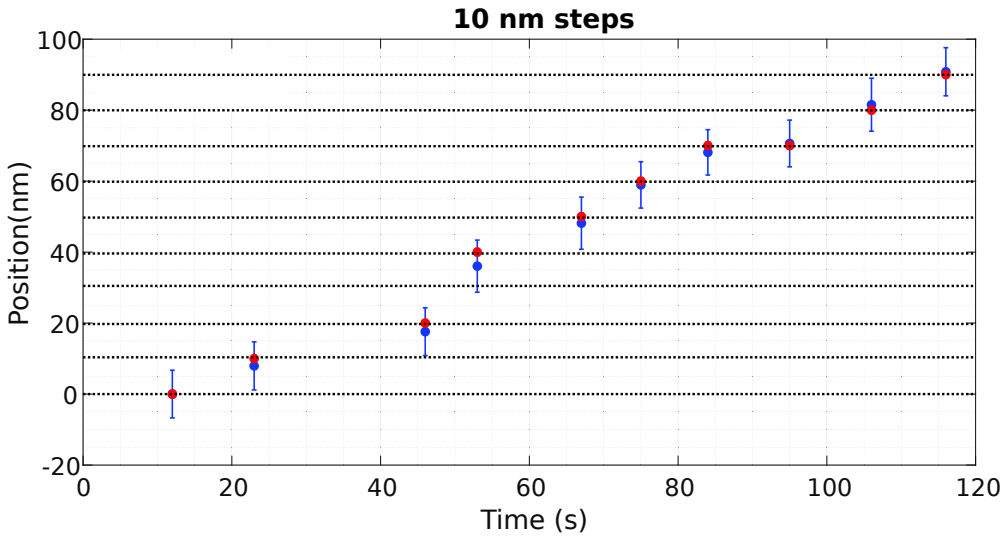

Figure 2.9 – Displacement resolution for 10 nm step. The error bars are the standard deviation around the mean position computed from the statistical ensemble composed from the detected displacements. There is a good agreement between the real position and the detected one. Nevertheless, the error bars overlaps demonstrating that a displacement of 10 nm is not resolved and this expected because the static error are dominant considering that σ_0 is precisely in the order of 20 nano meter.

2.4 STATISTICAL PROPERTIES OF BROWNIAN MOTION

In this section, we present some important statistical tools used to quantify our measurements are presented. The Probability Density Function (PDF) associated with an ensemble of particle position x at time t is described, together with the important tool of the Mean Squared Displacement (MSD).

2.4.1 *Probability density function (PDF)*

The trajectories recorded by video microscopy represents a rich source of information about the dynamics of the particle. From the tracking software, we get as two time series $Y(t)$ and $Z(t)$ the projections of the trajectory along the Y and Z axes where time t is sampled at a frequency f=120Hz. An example of a tracked trajectory and the corresponding projections are displayed in figure (2.10). We obtain here an ensemble of discretized positions along Y and Z axis :

$$Y(t_n) = Y_n,\ Z(t_n) = Z_n, \tag{2.8}$$

with $Y(t_n)$ and $Y(t_n)$ the tracked positions of the particle in the video frame n. The time interval between two successive frames is $\Delta t = 1/f$.

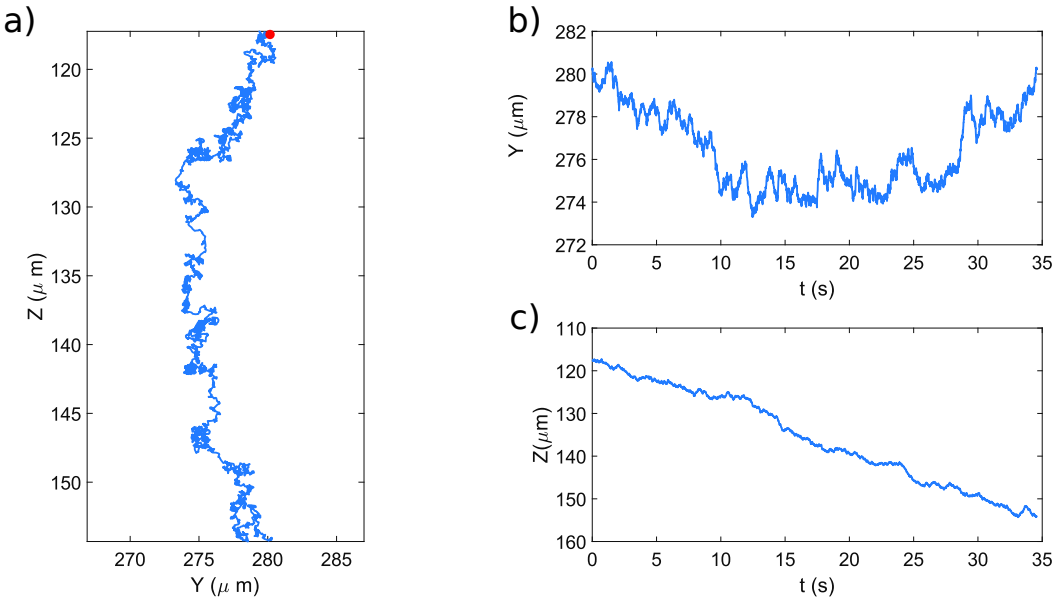

Figure 2.10 – Recorded trajectory of a Melamine bead sedimenting in water. Panel a) shows the 2 D trajectory where the red dot representing the initial positions recorded at t=0. Panels b) and c) are the projection along Y and Z axis.

From the position $\{Y_n\}$ and $\{Z_n\}$ ensembles, we can compute the displacements ensembles $\{\Delta Y_n\}$ and $\{\Delta Z_n\}$ where Δ is the difference operator defined as :

$$\Delta Y_n = Y_{n+1} - Y_n. \tag{2.9}$$

The discrete PDF of displacements represents the probability that a particle diffuses over a distance ΔY_n during the time interval Δt. It is defined as :

$$\mathcal{P}(\Delta Y_n, \Delta t) = \frac{1}{\sigma\sqrt{2\pi}} e^{-\frac{(\Delta Y_n - \mu)^2}{2\sigma^2}} \tag{2.10}$$

where μ and σ^2 are respectively the true mean and the true variance of the PDF of displacements. This PDF is constructed from the ensemble of displacements ΔY_n in the following way.

For an ensemble of N detected displacements, we start by choosing the appropriate number of bins which we choose following the empirical Rice rule[2] as :

$$nbins = 2\sqrt[3]{N}, \tag{2.11}$$

2 http://onlinestatbook.com/

This chosen number of bins defines a bin width as:

$$\delta b = \frac{max(\Delta Y_n) - min(\Delta Y_n)}{nbins} \tag{2.12}$$

with the condition that $\delta b > \sigma_0$.

We then count the number of displacements that lies within the adjacent intervals $[min(\Delta Y_n) + j\delta b, min(\Delta Y_n) + (j+1)\delta b]$ where $j = [\![0, nbins - 1]\!]$. With this method, figure (2.11) displays the constructed PDF of displacements for the trajectory presented in figure (2.10).

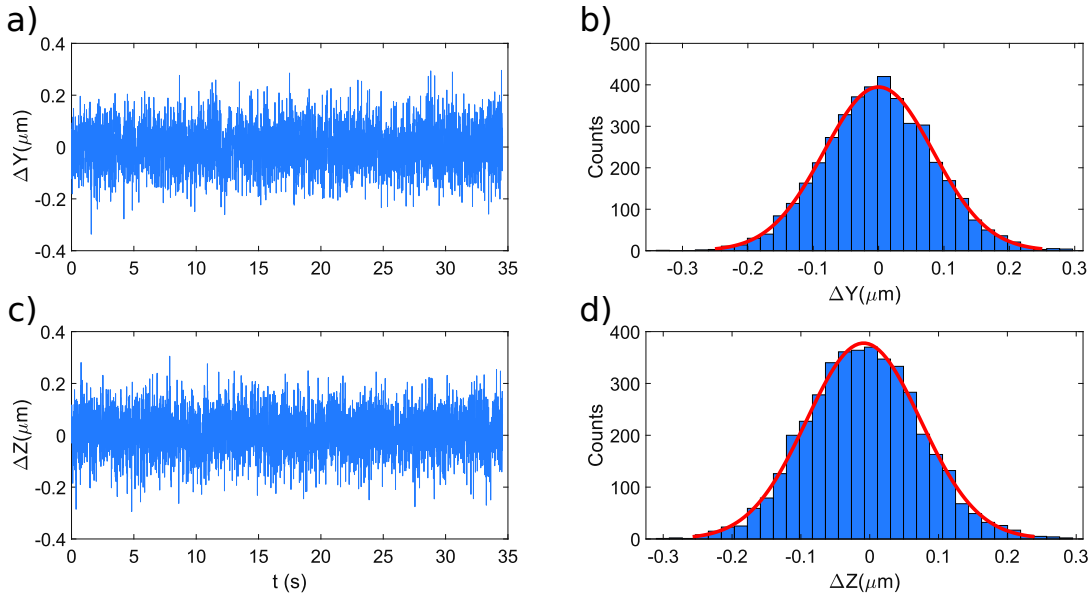

Figure 2.11 – Constructed PDF of displacements of the trajectory presented in (2.10). Panels a) and c) shows respectively the temporal displacements along the Y and Z axis. The panels b) and d) represents the PDFs of displacements constructed using the method described in the main text.

As always using a finite set of N measurements, the parameters μ and σ are not respectively the tue mean and true variance of the PDF of displacements, but estimators of these parameters. They can be estimated from the statistical sample of detected displacements using the moments of the PDF. Assuming that the stochastic variable ΔY_n follows the normal distribution $\mathcal{N}(\mu, \sigma^2)$, an estimator of μ the mean displacement along the Y axis is given by :

$$\hat{\mu} = \frac{\sum_{n=1}^{N} \Delta Y_n}{N - 1} \tag{2.13}$$

The estimator of the variance is given by :

$$\hat{\sigma}^2 = \frac{\sum_{n=1}^{N} (\Delta Y_n - \hat{\mu})^2}{N - 1} \tag{2.14}$$

A close discussion on the uncertainties associated with the mean and the variance are presented in more details in chapter III.

2.4.2 *Mean Squared Displacement (MSD)*

The MSD gives important informations on the transport properties of particles diffusing in water. An estimator of the MSD defined in equation (1.5) is the Time Averaged MSD $\delta Y^2(\tau_n)$ [37] :

$$\delta Y^2(\tau_n) = \frac{1}{N_I} \sum_{i=1}^{N_I} [x_{i+n} - x_i]^2 \tag{2.15}$$

with $N_I = N + n - 1$ the number of overlapping[3] intervals of length n, and $\tau_n = n\Delta t$ the time lag over which we compute the mean squared displacement. In practice, we do not compute the MSD over the length of the trajectory N, but we rather use a length reduced to $N/3$ because for long time intervals, the statistical accuracy of our estimate drops down. This is due to the decrease in the size of the statistical sample over which we average the displacements. This $N/3$ value is usually recognized as a "safe" value [37].

The standard error associated with the determination of the MSD is given by:

$$SE(\delta Y^2(\tau_n)) = \frac{\sigma_{\delta Y^2(\tau_n)}}{\sqrt{N_I}}, \tag{2.16}$$

where $\sigma_{\delta Y^2(\tau_n)}$ is the standard deviation around the mean squared displacement averaged over the time interval τ_n.

In our experiments we track an ensemble of N_T trajectories. In order to smooth the time averaged MSD we define the Ensemble time averaged MSD :

$$< \delta Y^2(\tau_n) >= \frac{1}{N_T} \sum_{i=1}^{N_T} \delta Y^2(\tau_i), \tag{2.17}$$

which is simply the ensemble average over the individual (single trajectory) time average MSDs. An example of the time averaged MSDs and the ensemble time averaged MSD are displayed in figure (2.12). There is a good agreement between the theoretical and the measured MSDs.

3 We can average the mean squared displacements over dependant or independent (overlapping or non overlapping) time intervals. Using independent interval decreases the size of the sample over which we estimate the MSD. In reference [37] a closer comparison between the two methods is done and they yield the same results. We chose the overlapping method because of the larger size of the sample.

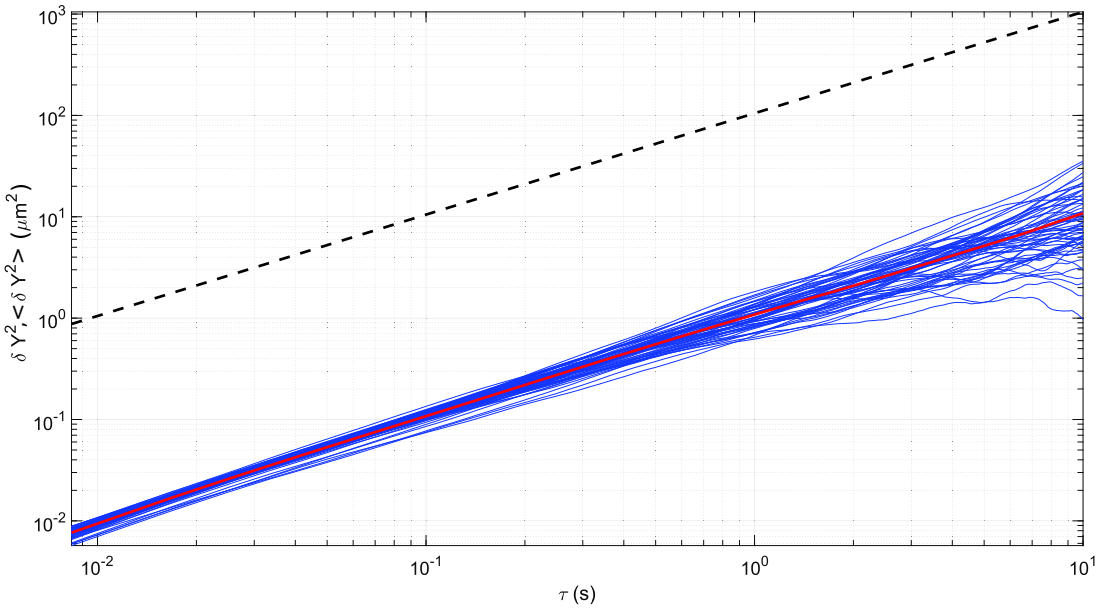

Figure 2.12 – Mean Squared displacement for Melamine beads diffusing in water at room temperature. The black dashed line in the theoretical time averaged MSD defined by equation (1.5) where we took the theoretical value of the diffusion coefficient (the offset with respect to the experimental MSDs is made for the sake of clarity). The blue continuous line represents the measured time averaged MSDs for different trajectories and the red continuous line is the ensemble time averaged MSD defined in equation (2.17). The poor statistics issue explained in the main text is visible for long time lags.

2.5 CONCLUSION

We described in this chapter our experimental setup build to track the real-time Brownian trajectories of colloidal particles. The setup consists of contra-propagating cross-polarized Gaussian beams, combined with a dark field microscope. The temporal resolution of our experiment is $\Delta t = 1/120s$ determined by the inverse of the frame rate, and a positional resolution of the order of 20 nm is demonstrated. Furthermore, the statistical properties of Brownian motion are analysed by introducing the probability density function of the displacements and the mean squared displacement. The methods of measuring, from the experimental trajectories, Brownian parameters relevant in the following chapters such as the PDF of displacements and the MSDs have been described here in details.

In the following chapters indeed, we will show how this setup and these methods can be efficiently implemented in order to analyse and

quantify colloidal Brownian dynamics in various types of external force fields.

3

BROWNIAN COLLOIDAL PARTICLES IN EXTERNAL FORCE FIELDS : FROM SEDIMENTATION TO CONVECTIVE TRANSPORT

As presented in the first chapter, colloidal suspensions are good candidates for the study of the mechanical interaction between light and matter. It is a straightforward fact that colloidal dispersion displays collective motions : sedimentation of an ensemble of colloidal particles suspended in water is an obvious example [34]. Furthermore, mass transport in the fluid can modify the motion of the particles : convective drag is an example of an external flow modifying the dynamic of the particles lying within the convective flow. In this chapter, we exploit a competition between sedimentation and convection in order to control the motion of the particle assembly. This competition stems from the heat dissipated in the fluid under laser illumination. Three dynamical regimes can be describer :

1 Sedimentation regime : when the particles sediment because of gravity.

2 Convection regime : when the particles are lifted up because of the convective flow induced by the temperature gradient generated by the absorption by water of the laser beam sent through the fluid.

3 Suspended regime : when the particles remain in the field of view due to the compensation of sedimentation by the convective flow.

In the second part, we will model the convective flow induced by the laser as a consequence of a change of fluid density. Our model will allow us to estimate the convection velocities in the steady state. This estimates turns out to be in good agreement with the experiments.

In the first section, we will present our experimental results revealing the existence of such three different regimes of dynamics. We will

characterize, from the Brownian motion analysis, the induced fluid currents as the manifestation of an external force field. We will carefully compare the dynamics each of the three regimes, and look in detail at the properties of the suspended regime.

3.1 CONTROLLING THE COLLOIDAL ASSEMBLY WITH TUNABLE LASER IRRADIATION

In this section, we will present the experiments we performed in order to describe and characterize the dynamical regimes that depend on the power of the laser sent through the system. We will start with low laser power for which the sedimentation of the particles determines the colloidal dynamics. We then show that by progressively increasing the laser power, a convective flow is induced, that eventually drags the particles upward. Finally, we reveal the existence of an intermediate regime between sedimentation and convection where the falling of the particles is compensated by the convective flow.

Our experiments consists in tracking as many particles as possible that are illuminated by the laser beam, and monitoring the evolution of the particle motions as the power of the laser is increased.

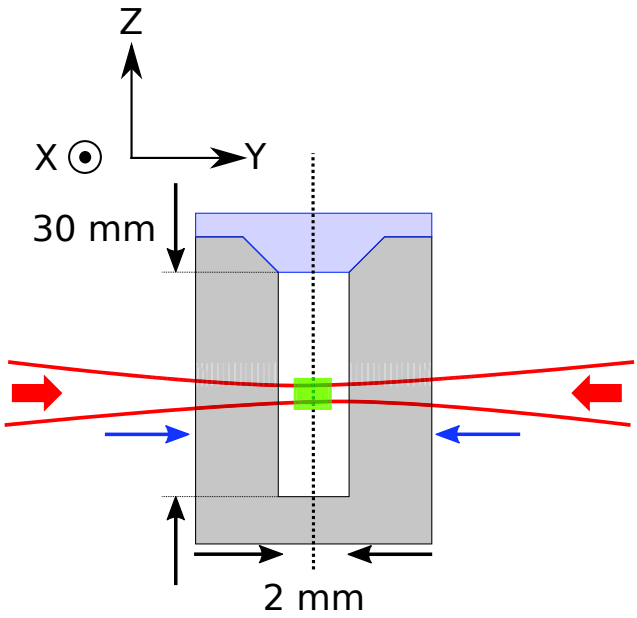

Figure 3.1 – Experimental SetUp in the contra propagating scheme. The red arrows represents the direction of propagation of each beam, the blue arrows is the confocal parameter which is in the experiment $2Y_R = 12mm$. The green area is the field of view of our microscope $350\mu m \times 250\mu m$. For our measurements we use Melamine bead with a diameter d = 940 nm.

This monitoring will essentially consists in averaging over the ensemble of trajectories the Brownian motion of the colloids in order to provide estimators of mean velocities along the vertical and the horizontal axes - see figure (3.1).

3.1.1 *Force balance point of view*

Let us consider the simple case of a single particle, of a density $\rho_p = 1.6$ g.cm^{-3} for Melamine and radius R, immersed in water at room temperature. If the density of the particle is larger than the density of water $\rho_w = 1$ g.cm^{-3}, then the particle will settle with a final velocity V_{Stokes}. The final velocity is determined through the second law of Newton applied on the particle :

$$F_s + F_b = F_g, \tag{3.1}$$

with $F_s = 6\pi\eta R U_{Stokes}$ is Stokes viscous force (η being the dynamical viscosity of the fluid), F_b is the buoyancy force from Archimedes' principle, and F_g the gravity force. This situation is schematized in the left hand side of figure (3.2).

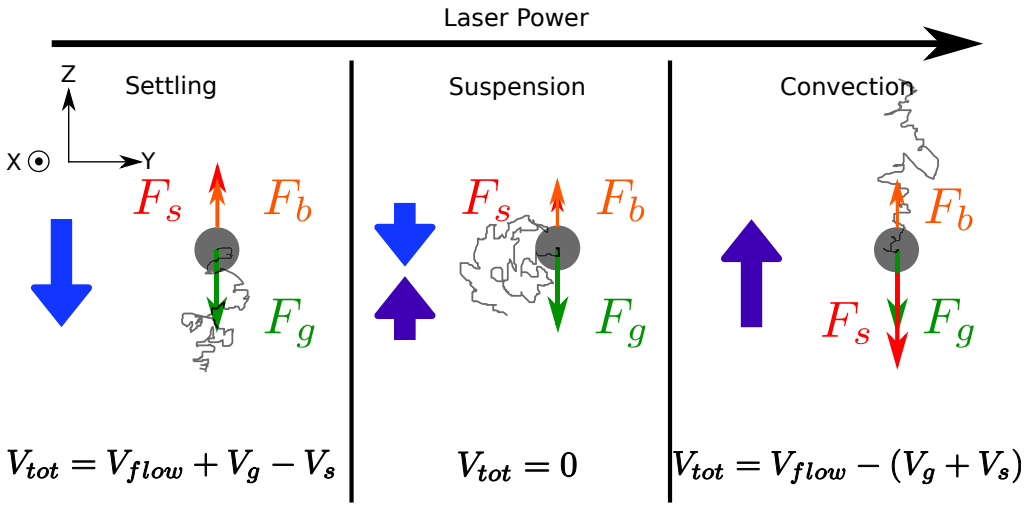

Figure 3.2 – Applied force analysis on a single particle : F_b buoyancy force, F_g gravity force, F_s Stokes force. The blue arrow represents the settling flow direction, and the purple arrow represents the induced convective flow. From left to right :
Settling regime : The sedimentation flow leads the motion,
Suspension regime : the convective flow compensates the sedimentation flow,
Convection regime : the convection current dominates the dynamic.

By replacing each force term in equation (3.1), we get the Stokes final velocity of the particle :

$$\Delta\rho g\frac{4}{3}\pi R^3 = 6\pi\eta R U_{Stokes} \Rightarrow \vec{U}_{Stokes} = \frac{2\Delta\rho g}{9\eta}R^2\hat{z}, \tag{3.2}$$

where $\Delta\rho = \rho_w - \rho_p < 0$.

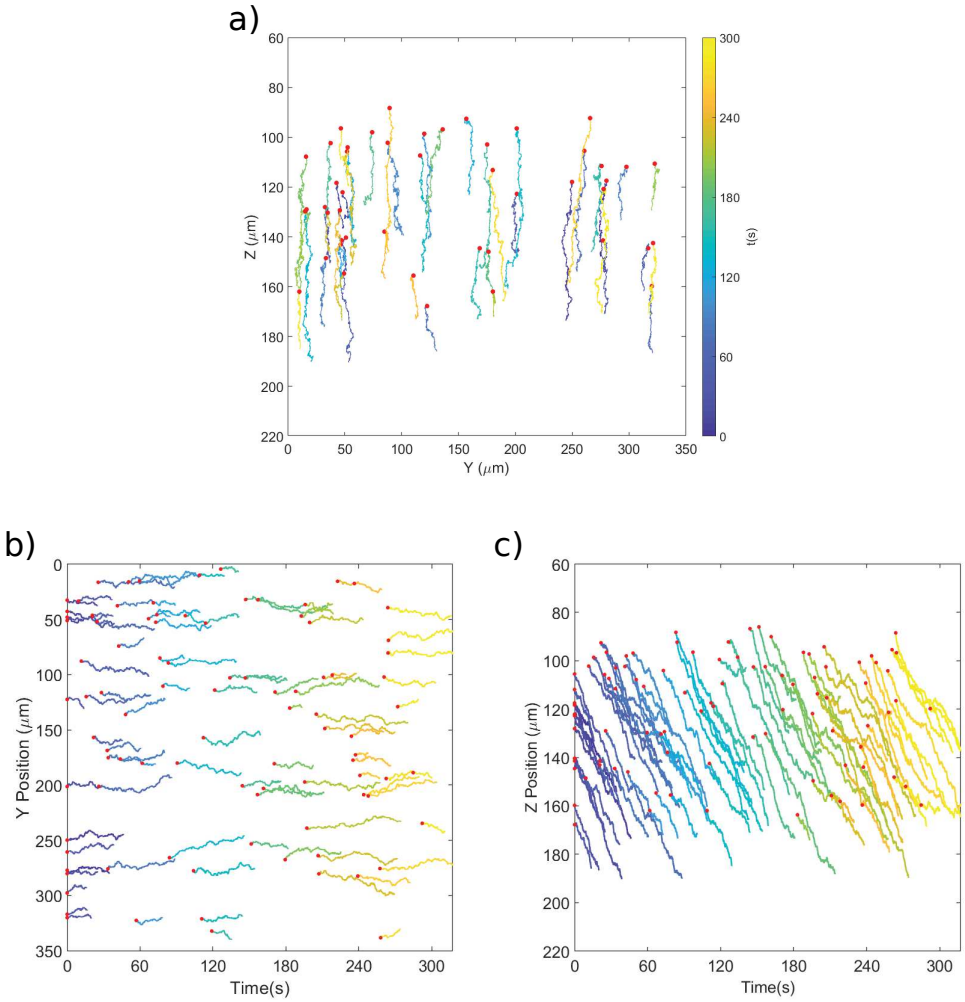

Figure 3.3 – Tracked trajectories of Melamine particles with radius R = 0.47µm at low laser power : panel a) trajectories in the Y-Z plan, panels b) projection along Y axis where the motion is diffusive and panel c) projection along the Z axis where the motion is ballistic and directed downward due to gravity. The color bar represents the time when we start tracking the particle. The red dots represents the initial positions. We remind that the filed of view is 250µm and 350µm along Z and Y axis respectively.

This analysis is done for a single particle, settling within a large cell with no influence of finite volume effects, such as no slip boundary

conditions. For our experiments, performed with an ensemble of particles, the situation is more complex. First, each particle creating its own flow dynamics, interparticle long range interactions must be considered. Such interactions can be described using the Oseen tensor[41, 42]. Then, from the collective nature of the colloidal assemblies, the local concentration of particles is inhomogeneous and change with time due to the formation of more or less dense "blobs"[34]. Considering this, any measurement of a velocity averaged over the ensemble of particles will depend on every initial configuration, obviously different from one sample to another and one experiment to the other.

We show in figure (3.3) an example of trajectories of particles tracked using a low laser power. We can see clearly from the trajectories that all the particles are sedimenting along the vertical axis, The motion remains diffusive along the Y axis only determined by the thermal fluctuations.

3.1.2 *Laser induced convective flow*

If we now increase the power of the irradiating laser, we progressively observe a reduction of the sedimentation velocity. In fact, heating the fluid, the laser reduces its density along the optical beam. As a consequence, buoyancy driven flow is induced that can eventually drag the particles upward - see figure (3.2). We show in figure (3.4) an example of tracked trajectories of Melamine micro particles transported by this induced convective flow. In such upward transport, the motion is ballistic along Z axis, while remaining diffusive along the Y direction, as expected. In these experiments, we work in the contra-propagating laser beams configuration presented in the first chapter, so that there is no external force along the Y axis.

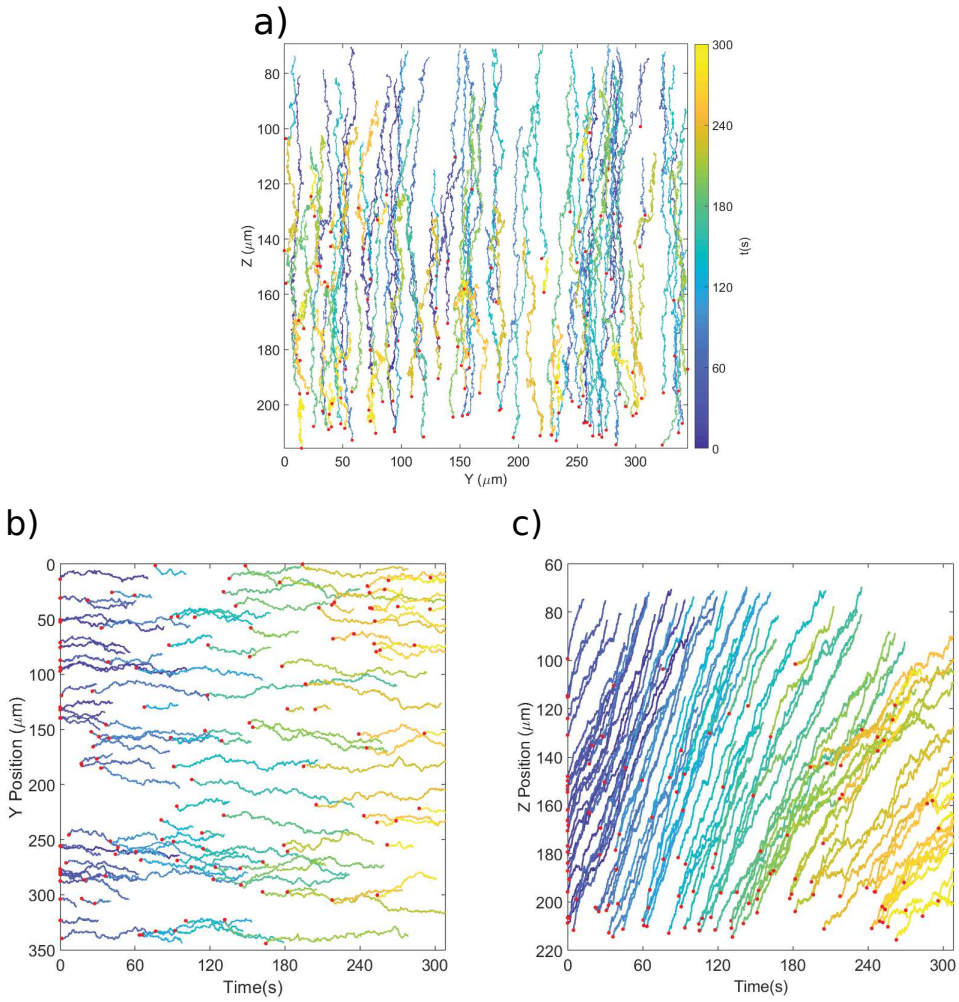

Figure 3.4 – Tracked trajectories of Melamine particles with radius R = 0.47µm at high laser power : panel a) trajectories in the Y-Z plan, panels b) projection along Y axis where the motion is still diffusive and panel c) projection along the Z axis where the motion is ballistic and directed upward. The color bar represents the time when we start tracking the particle.

As seen comparing figures (3.3) and (3.4), the dynamics in the sedimenting and convecting regimes are similar, apart of course from the the change of direction in the Z direction.

3.1.3 *Quantitative analysis of both regimes*

This similarity will allow us using the same statistical tool to describe quantitatively the colloidal motion. We measure the estimator of the mean

velocity along the z-direction for one particle tracked among the assembly, this estimator is defined as :

$$< V_z >_{N_i} = \frac{\mu_i^{\Delta z}}{\Delta t} = \frac{F_{ext}^i}{\gamma} \tag{3.3}$$

where $< ... >_{N_i}$ is the ensemble average over all the (independent) elementary displacements $(N_i - 1)$ of the particle i tracked on the CCD camera and N_i is the number of detected positions. $< V_z >_{N_i}$ corresponds to the ballistic component of the motion under the external force field induced by sedimentation or convection . The external force applied to the particle i is F_{ext}^i, and γ is the dragg coefficient given by $\gamma = 6\pi\eta R$, for a spherical particle with a radius R immersed in a fluid of viscosity η. The large volume of our sample and the position of our region of interest over which we perform our tracking experiments allow us to assume for η the bulk tabulated value for water at room temperature.

In equation (3.3), $\mu_i^{\Delta z}$ is an estimator of the mean displacement for the particle i along z , defined in the first chapter by :

$$\mu_i^{\Delta Z} = \frac{\sum_{n=1}^{N_i} Z_{n+1} - Z_n}{N_i - 1}, \tag{3.4}$$

where Z_n is the absolute tracked position of the bead at $t = n\,\Delta t$.

Our tracking experiment, as schematized in figure (3.2), consist of collecting the light scattered by the particles entering the laser beam extension within the sample. By construction , this "field of view" of our dark field microscope also defines the volume within which the convective force field is applied. By construction too, we actually track not a single particle but an ensemble of N_T such particles.
Assuming that this ensemble is made of N_T mono dispersed particles (i.e. identical radii), a mean velocity can be measured as:

$$< V_z >_{N_T} = \frac{< \mu^{\Delta Z} >_{N_T}}{\Delta t}. \tag{3.5}$$

where $< ... >_{N_T}$ is an ensemble average, but this time defined over N_T in contrast with equation (3.3). Here then the estimator of the mean displacement along z, is given by averaging over the N_T trajectories :

$$< \mu_z >= \frac{\sum_{i=1}^{N_T} \mu_i^{\Delta Z}}{N_T - 1},$$

with $\mu_i^{\Delta Z}$ given by equation (3.4).

In figure (3.5), we gather measured estimators of the mean velocity along z, obtained at different laser powers by averaging over the tracked particles during at least 5 min for each measurement and repeating twice the measurement for each laser power. The error bars are the standard deviation around the mean value averaged over a minimum of two experiments at a set laser power.

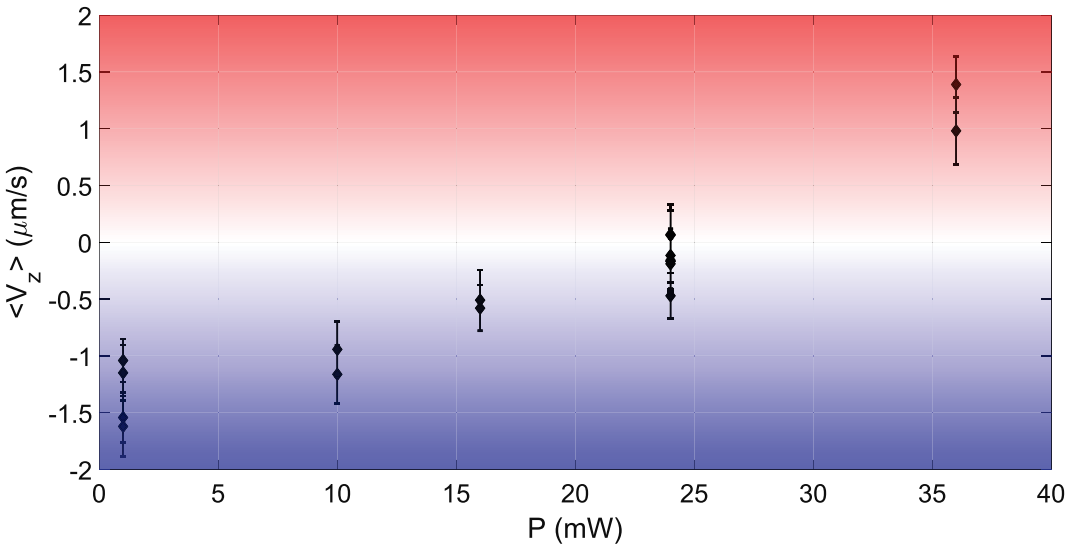

Figure 3.5 – Mean velocity along the z-axis for different laser power P_0 for 1 μm melamine beads. The blue region is the sedimentation regime,the green region is the convective regime, and the white region is the suspension regime. The errorbars are the standard deviation around the estimator of the mean velocity.

We can see that at low laser power, the mean velocity along z, is negative which means that the particle is settling. However, at high laser power the mean velocity is positive indicating an ascending convective

flow. At maximal power P = 35 mW, the convective velocity corresponds to :

$$< V_z >_{convection} - < V_z >_{settling} = 3 \pm 0.5\ \mu m/s, \tag{3.6}$$

We will try to evaluate the convective velocity by modelling, in the second part of the chapter, the colloidal dynamics under laser irradiation.

3.1.4 *Intermediate laser power : a colloidal suspension regime*

As seen in figure (3.5), the vertical velocity of the ensemble of particles can drop to values close to zero for an intermediate laser power (around 25 mW). In this case, the ballistic contribution of gravity to the colloidal Brownian motion is cancelled by the opposed ballistic drag of the assembly due to the convective flow as described in figure (3.2). In this compensation regime the particles perform a diffusive motion along both the Y and Z directions. In figure (3.6), we show the trajectories of such a regime.

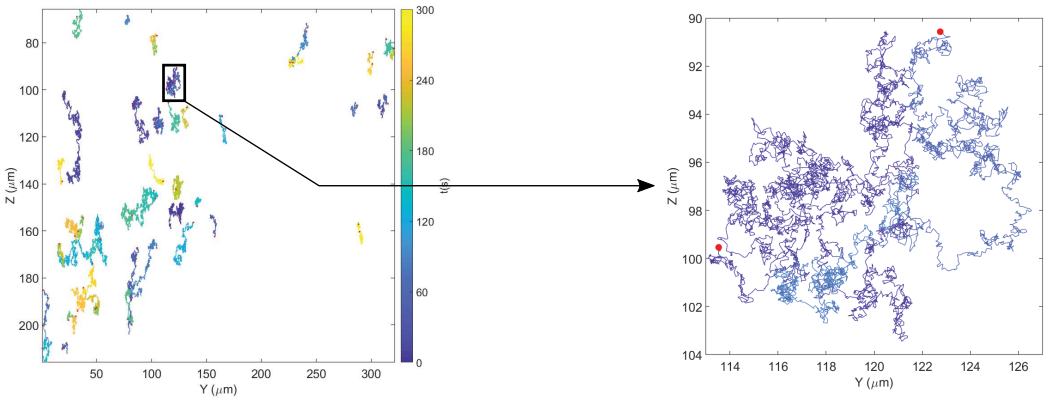

Figure 3.6 – Tracked trajectories of Melamine particles with radius R = 0.47μm at a laser power P = 24 mW. In the right hand side a zoom is presented to displays the "Free Brownian motion" character of the suspended regimes.

The projections of the recorded trajectories shows free Brownian motion, the motion is indeed much more diffusive than the two others regimes. We will quantify this feature below.

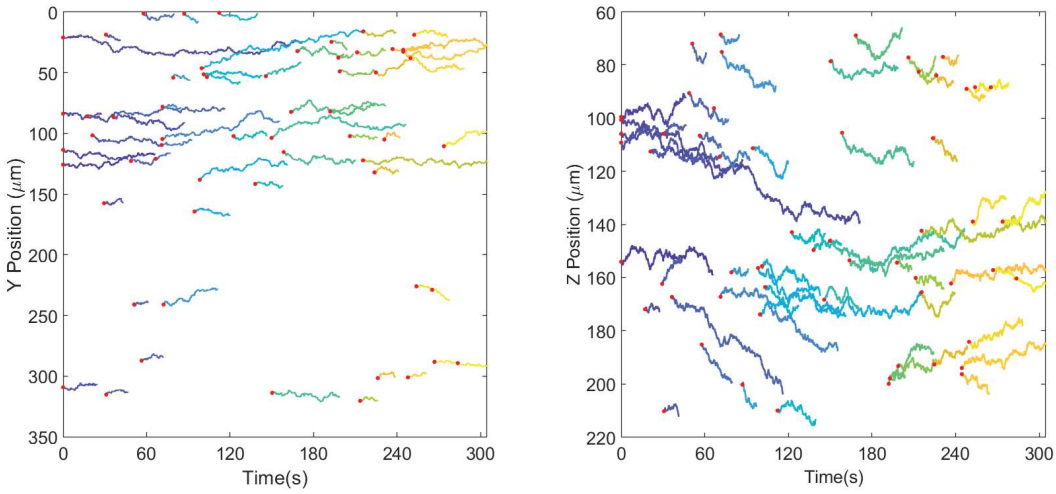

Figure 3.7 – Projections of the trajectories showed in figure (3.6). The "free" Brownian motion character is clear along the Y and Z axes. The red Dots are the initial positions.

3.1.5 *Mean-square displacement*

The Brownian dynamics of a particle can be efficiently analysed looking at the time evolution of the MSD. Figure (3.8) displays the expected evolution of the MSD associated with free Brownian motion and Brownian motion performed in an external force field.

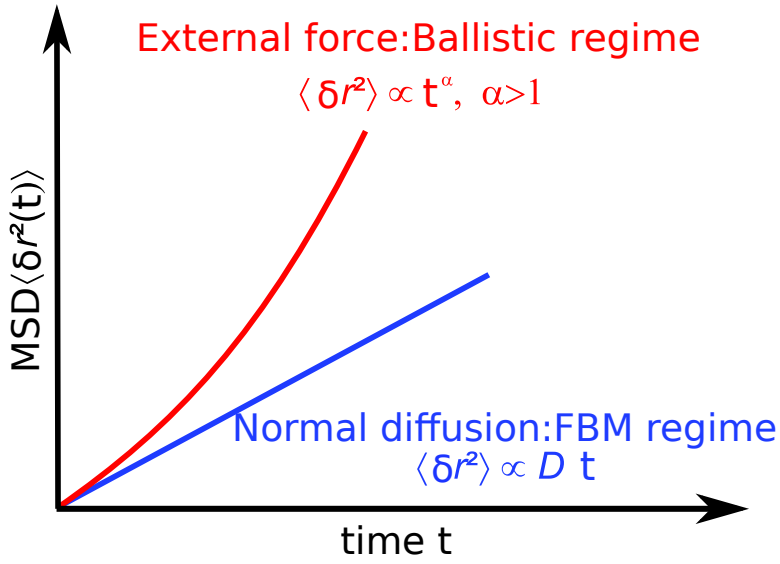

Figure 3.8 – The MSD for different particle dynamics.

These evolutions follow simple laws, we present in figure (3.8) the MSDs for three different particle dynamics :

- For free diffusive motion, the MSD grows linearly with time :

$$< \delta r^2(t) >= 2Dt, \tag{3.7}$$

  with D is the diffusion coefficient, we analyse projected trajectories on vertical and horizontal axes, the MSD is defined in one dimension[1].

- Under an external force field the motion is directed : the MSD is quadratic with respect to time :

$$< \delta r^2(t) >= V_0^2 t^2 + 2Dt, \tag{3.8}$$

  where V_0 is the velocity induced by the force field with $V_0 = \frac{F_{ext}}{\gamma}$, as discussed in equation (3.3).

The quadratic term, known as the ballistic contribution, plays also an important role in the context of active Brownian motion [43]. At the level of single recorded trajectory j the Time Averaged MSD (TAMSD) $\delta r^2(\tau)$ is defined a follows[37], with r=Y or r = Z in our experiments :

$$\delta_j r^2(\tau_n) = \frac{1}{N_j} \sum_{i=1}^{N_j} [r_{j+i} - r_j]^2 \tag{3.9}$$

with N_j the number of time lags used to compute the MSD over the trajectory length. In addition, $\tau_n = n\Delta t$ represents the time interval over which the squared displacements are averaged.

When tracking multiple trajectories, it is interesting to define the Ensemble Time Averaged MSD (ETAMSD) for an ensemble of N_T particles as :

$$< \delta r^2(\tau) >_{N_T} = \frac{\sum_{j=1}^{N_T} \delta_j r^2(\tau)}{N_T}. \tag{3.10}$$

We displays in figure (3.9), such ETAMSD in the three different regimes of experiment. For P_{Low} and P_{High}, the ballistic contributions from settling and convection gives a clear parabolic shape to the ETAMSD along the Z

1 For free Brownian Motion that develops in d-dimension, one has:

$$< \delta^{(d)} r^2(t) >= 2dDt,$$

axis ($< \delta Z^2(\tau) >_{N_T}$) in agreement with the the model presented in equation (3.8). In contrast $< \delta Y^2(\tau) >_{N_T}$ is linear with time, showing how the motion remains freely diffusive, according to the equation (3.7). It is striking that, in the suspension regime both $< \delta Y^2(\tau) >_{N_T}$, and $< \delta Z^2(\tau) >_{N_T}$ are linear with time. Under the compensation of the settling by the convective flow, the colloidal assembly develops a dynamic which ressemble in all directions the dynamics of free Brownian motion.

By fitting the experimental ETAMSD to the equations (3.7) and (3.8) a measure of the diffusion coefficient is obtained :

Laser power P	$D_y(\mu m^2/s)$	$D_z(\mu m^2/s)$
P=1mW	$0.528 \pm 5 \times 10^{-4}$	$0.573 \pm 900 \times 10^{-4}$
P=24mW	$0.616 \pm 5 \times 10^{-4}$	$0.622 \pm 10 \times 10^{-4}$
P=36mW	$0.596 \pm 1 \times 10^{-4}$	$0.623 \pm 150 \times 10^{-4}$

and also the drag velocities :

Laser power P	$V_y(\mu m/s)$	$V_z \mu m/s)$
P=1mW	0.012 ± 0.016	-0.983 ± 0.071
P=24mW	0	0.131 ± 0.02
P=36mW	0.125 ± 0.015	1.1 ± 0.031

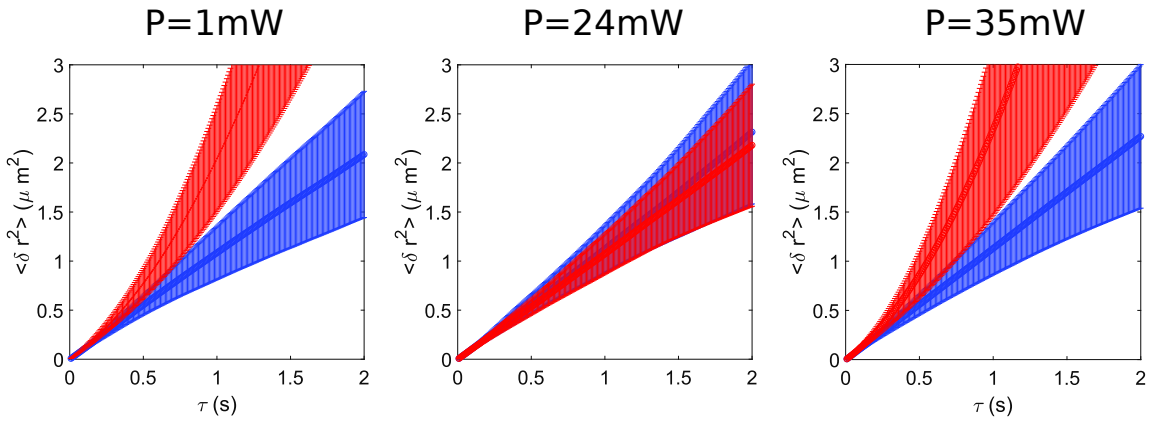

Figure 3.9 – ETAMSD in the three regimes. In the suspended regime both the TEAMSD along Y and Z are diffusive. The errorbars represents the standard deviation around the ETAMSD value defined in equation (3.10) for a given time lag.

3.1.6 *Diffusion Coefficient from the probability density function of displacement*

The diffusion coefficient is the ratio between the thermal fluctuations and the dissipation within the fluid due to the viscous drag[21]. Defined by Stokes- Einstein equation, the diffusion coefficient writes as :

$$D = \frac{k_B T}{\gamma} = \frac{k_B T}{6\pi\eta R}, \tag{3.11}$$

As discussed in equation (1.5), the diffusion coefficient can be measured from the MSD calculated over a Brownian trajectory. But it can also be measured, from a statistical point of view, using the variance σ^2 of the displacements probability distribution, known as Probability Density Function (PDF).

For free Brownian motion, such distribution follows a normal law, with a Gaussian shape and a variance for a single particle i, defined as :

$$\sigma^2 = 2D_i\Delta t \tag{3.12}$$

where Δt is the sampling time given by the inverse of the frame rate and D_i the diffusion coefficient associated with the particle i.

In our experiment however, and just as for the mean displacement, we are dealing with an ensemble of N_T particles. Two possible methods, that turn our to be equivalent, to determine the diffusion coefficient :

Method I: This method is based on the concatenation of all the detected displacement in a single, large statistical ensemble for which the variance is computed. The result is presented in figure (3.10). This method assumes that all the particles are indiscernible, with identical radii and developing the same type of Brownian motion (ballistic or diffusive) with stationary PDF of displacements. The Melamine beads have a certain level of size dispersion that we will account for when comparing the experimental diffusion coefficient and the corresponding evaluation from Stokes Einstein law (3.11).

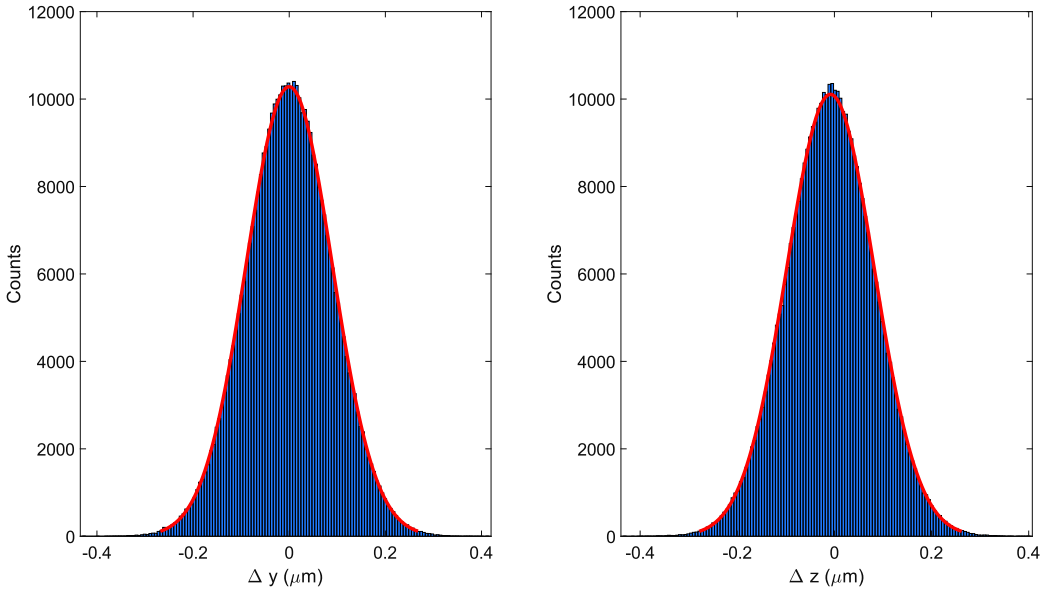

Figure 3.10 – Distribution of all detected displacement for Ml beads at P = 1 mW. The total number of points used to compute the distribution is $N_{tot} = \sum_i N_i = 4.10^5$ displacements. The histograms are constructed as presented in the methods section in chapter I. The red continuous line is a Gaussian fit of the PDF.

Measuring the diffusion coefficient using the variance of the PDF is more sensitive to localization errors[44], introduced in the first chapter, than the diffusion coefficient measured by fitting the MSD. The measured diffusion coefficient along Y and Z axes are : $D_Y^I = 0.478 \pm 0.002 \mu m^2/s$ and $D_Z^I = 0.486 \pm 0.002 \mu m^2/s$. The estimator of the mean velocity given by equation (3.3) is $< V_Z >_{N_{tot}} = 0.973 \pm 0.035$. Nevertheless, the estimators of the mean velocity along the vertical axis from the variance method and the MSD are in agreement.

Method II: This method computes the diffusion coefficient for each N_T trajectories and uses the ensemble of N_T diffusion coefficients to get a mean ensemble diffusion coefficient. An example of the PDF of displacements for one trajectory is presented in figure (3.11). The width of this distribution gives the variance given in equation (3.12).

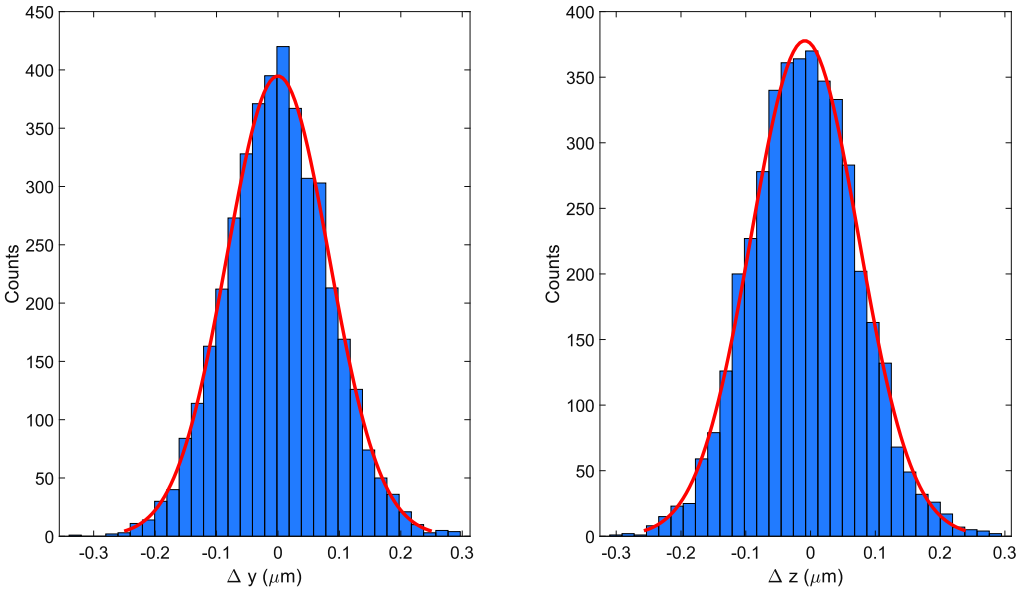

Figure 3.11 – Distribution of displacements for one Ml bead at P = 1 mW. The red continuous line is a Gaussian fit of the PDF. The total number of points used to compute the distribution is $N_i = 4150$.

Using this second method, we present in figure (3.12) the distributions of diffusion coefficient for different powers. In order to have a better insight about the distributions we present in figure (3.13) the top view of figure (3.12). The distributions are computed from the N_T diffusion coefficient of the detected particles during each experiment, and we repeat at least twice each experiment in order to assess the reproducibility of our measurements for each laser power that we use.

The measured diffusion coefficient using the second method is $< D_y >^{MII} = 0.491 \pm 0.005\,\mu m^2/s$ where the errors are the standard errors calculated by dividing the estimator of the standard deviation by the square root of the size of the statistical ensemble used to measure the estimator of the mean diffusion coefficient. This value is comparable from the statistical point of view to the diffusion coefficient measured using method I : $< D_y >^{MI} = 0.473 \pm 0.003\,\mu m^2/s$.

This values are to be compared with the theoretical diffusion coefficient, calculated at room temperature and the uncetainties are taken around the size dispersion around the mean radii, which is : $D_0 = 0.521 \pm 0.025 \mu m^2/s$.

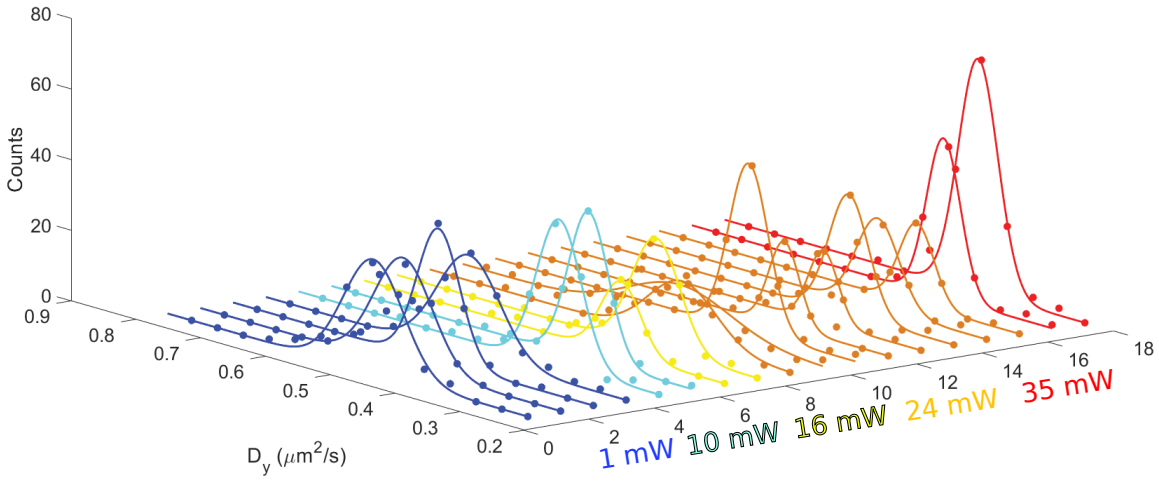

Figure 3.12 – PDF diffusion coefficient along y for different experiments. The numbers of bins used to present the distributions is determined by the Rice rule define chapter I. The counts as presented in the methods section is the number of times we count a diffusion coefficient within the intervals defined by the bin width.

As a conclusion of this section, the measured diffusion coefficient using the MSDs or the variance of the PDF of displacements gives comparable results, taking into account the sensitive aspect of the variance based method due to localisation errors. We demonstrate that the diffusion coefficient is independent from the laser power, taking into account the increase of the SNR by increasing the laser power. This indicates that the heat dissipated within the fluid by the laser irradiations induces thermal changes small enough as not to modify neither the dynamical viscosity of the fluid nor the diffusion coefficient itself.

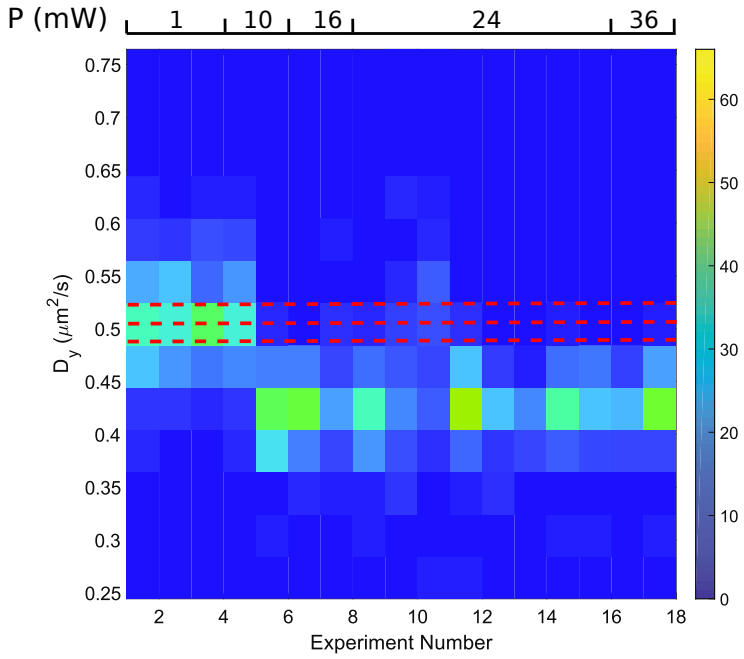

Figure 3.13 – Color map of PDF diffusion coefficient along y for different experiments. The red dashed line are the theoretical diffusion coefficient calculated from Stokes Einstein relation taking into account the size dispersion.

At a constant Stokes drag coefficient $\gamma = 6\pi\eta R = 7.88 \times 10^{-9} Kg.s^{-1}$ for our colloidal particles of radius $R = 0.47\mu m$ and taking the dynamic viscosity of water at $25^0 C$, the expected change in diffusion coefficient as temperature of the fluid is modified is :

$$\frac{\delta D}{\delta T} \propto \frac{k_B}{\gamma} = 1.75 \times 10^{-3} \mu m^2.s^{-1}.K^{-1}.$$

As our model will indicate, thermal gradients created by the laser under our experimental conditions are much too small to induce any significant change in the diffusion coefficient.

3.1.7 *Suspension regime : Influence of the density of the colloidal particles*

As determined by the laser power at which sedimentation is balanced by the convective grag, the suspension regime is obviously expected to depend on the density difference $\Delta\rho = \rho_w - \rho_p$, as already discussed in equation (3.2). To see this, we moved from Melamine particles to polystyrene ones, keeping the same radii between the 2 samples. Melamine has a density 1.5 higher than that of polystyrene. The results of our vertical velocity measurement at different laser power are presented in figure (3.14).

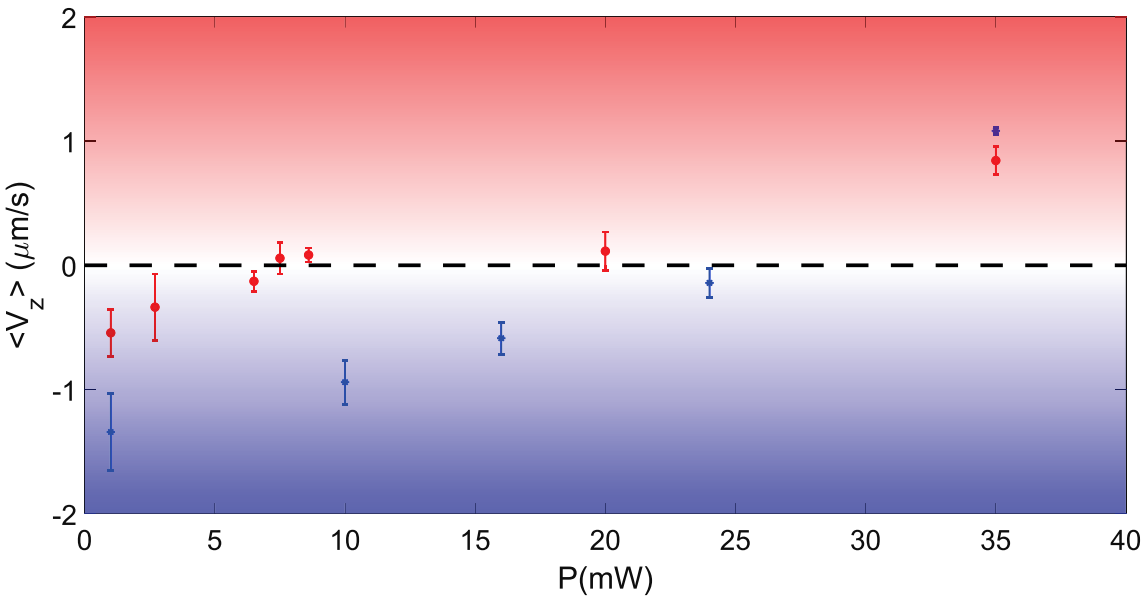

Figure 3.14 – The suspension power for melamine beads is greater than the one needed to suspend polystyrene beads. The red dots and the blue stars are the measured velocities for polystyrene and Melamine respectively, and the error bars represents the standard error with a confidence interval of 0.95%.

This clearly shows these influence of density on the onset of the suspending regimes, with $P_{susp} = 7.5mW$ for polystyrene and $P_{Susp} = 24mW$ for Melamine.

3.1.8 *Steady state dynamics*

The steady state condition is one important assumption in analysing our data . This assumption is also important with respect to the model presented below. In order to verify this experimentally, we fix the laser power and repeat the mean velocity measurements. The results are displayed in figure (3.15) which do reveal that, at a fixed laser power, the dynamics of the colloidal particles reaches a steady state in term of vertical velocities. This is confirming the assumption of steady state velocities used to model the absorption by water of laser irradiation and to calculate the induced velocities within the fluid.

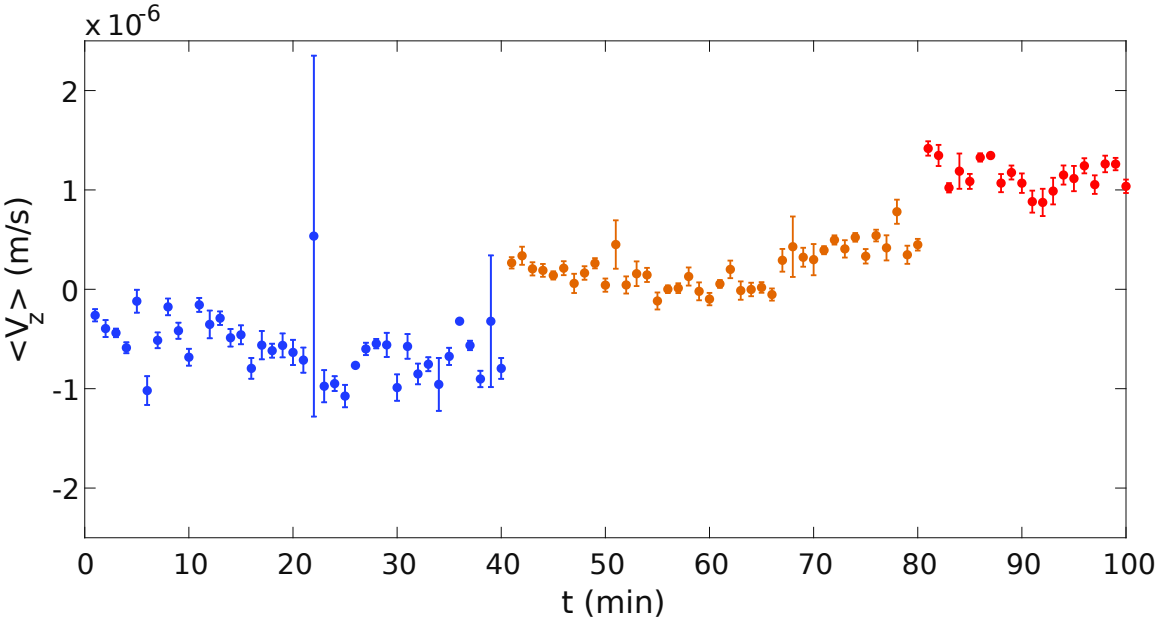

Figure 3.15 – Evolution of the estimator of the mean vertical velocity of polystyrene beads of radius $R = 0.5\mu m$. Each data point represents the mean velocity averaged over the mean displacements detected during one minute. The error bars are the standard deviation around the mean velocity. The blue, orange and red colors represents laser powers at 1 mW, 8 mW and 35 mW respectively.

3.2 MODELING THE LIGHT-INDUCED CONVECTIVE CURRENTS

In this section, we propose to model the observed effects induced by a laminar convective effect with the combination of mass and heat transports. This model relies on a boundary layer formulation of our experiment, which allows simple scales to be derived [45, 46].
The experiment is schematized in figure (3.16). It consists of a Gaussian beam immersed within a fluidic cell which lateral dimensions are much larger than the waist of the beam but which thickness is smaller than the Rayleigh length ($Y_R = \frac{\pi w_0^2}{\lambda}$) of the beam. Within such dimensions, any effect related to confinement within the fluidic sample is neglected. The laser beam is then considered as a cylindrical 'hot' wall which induces mass transport in a simple laminar way.

3.2.1 *Formulation of the problem*

Our aim is to describe the flow induced by the temperature gradient generated by the irradiation laser which energy is (partially) absorbed by the water surrounding the beam.

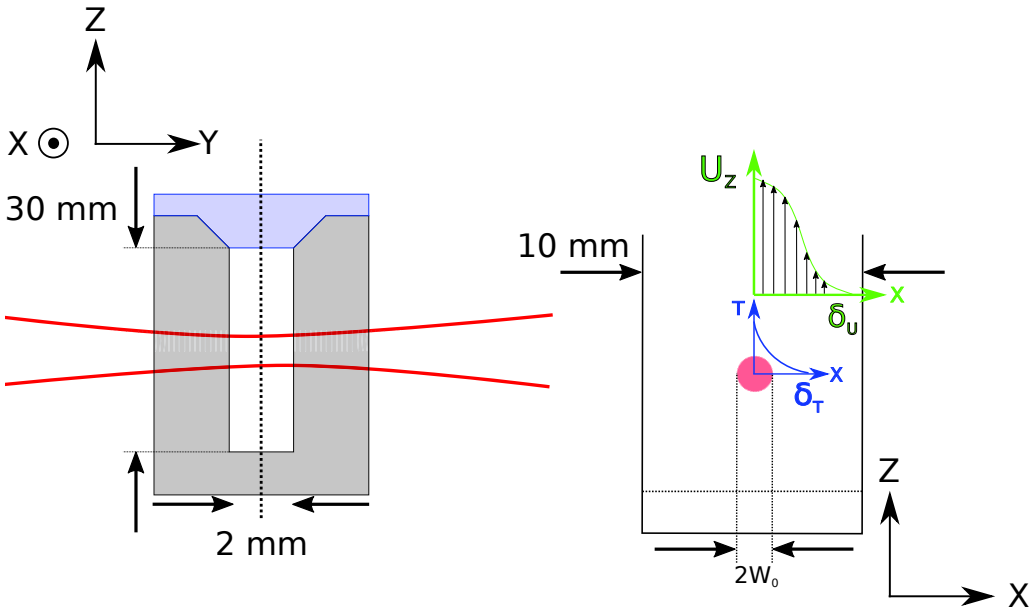

Figure 3.16 – Left hand side : front view of the sample, with the dimensions : $L_x = 10mm$, $L_y = 2mm$, $L_z = 30mm$. Right hand side : Cross cut in the (XZ) plan, $W_0 = 50\mu m$ is the beam waist with a Rayleigh length $Y_R = 12mm$, and δ_T and δ_u are the thermal and velocity boundary layers respectively.

Fluidic velocity profiles are determined through the Navier-Stokes equation (incompressible fluid) [47] :

$$\rho_0 \frac{D\vec{v}}{Dt} = \eta \vec{\nabla}^2 \vec{v} - \vec{\nabla} P + \rho_0 \vec{g} \tag{3.13}$$

where $\vec{v}$ is the velocity of a fluid cell of unit mass, density ρ_0, dynamic viscosity η (entering the Stokes drag for a spherical bead of radius Z : $\gamma = 6\pi\eta R$), under a gravitational acceleration $\vec{g}$ and pressure P. We adopt the Lagrangian description of the fluid motion with :

$$\frac{D\vec{v}}{Dt} = \frac{\partial \vec{v}}{\partial t} + (\vec{v}.\vec{\nabla}).\vec{v}, \tag{3.14}$$

the term $\vec{v}.\vec{\nabla}$ describing the advective contribution when following a fluid cell in its motion. Each term of equation (3.13) has a clear physical meaning :

- $\eta \vec{\nabla}^2 \vec{v}$ corresponds to the viscous force generated by the flow on the cell within the fluid,
- $-\vec{\nabla} P$ is the pressure force exerted of the fluid cell,
- $\rho_0 \vec{g}$ is the weight exerted by gravity on the cell.

When the fluid is at rest ($\vec{v} = \vec{0}$), one recovers the hydrostatic equilibrium condition : $\rho_0 \vec{g} - \vec{\nabla} P = 0$.

But when turned on, the laser will heat the fluid and thereby modify its density. We assume that this modification is a small change $\delta\rho$ in density with $\rho = \rho_0 + \delta\rho$, $\delta\rho \ll \rho_0$. In the line of the Boussinesq approximation [48], this small change breaks the hydrostatic equilibrium with:

$$\rho_0 \vec{g} - \vec{\nabla} P = -\delta\rho \vec{g} \tag{3.15}$$

and puts the fluid into motion along the vertical (Z) axis. This induced motion is described by the Navier-Stokes equation:

$$\rho_0 \frac{Dv_z}{Dt} = \eta \vec{\nabla}^2 v_z + \delta\rho g, \tag{3.16}$$

together with the mass conservation equation including the change of density :

$$\frac{D\rho}{Dt} + \rho \vec{\nabla}.(v_z \hat{z}) = 0 = \frac{D\rho_0}{Dt} + \rho_0 \vec{\nabla}.(v_z \hat{z}) + \frac{D\delta\rho}{Dt} + \delta\rho \vec{\nabla}.(v_z \hat{z}) \tag{3.17}$$

and obviously $\frac{D\rho_0}{Dt} = 0$ and $\frac{D\delta\rho}{Dt} + \delta\rho \vec{\nabla}.(v_z \hat{z}) = 0$. This implies that $\vec{\nabla}.(v_z \hat{z}) = 0$ so that $v_z = v_z(x)$ and $\vec{\nabla}^2 v_z = \frac{\partial^2 v_z}{\partial x^2}$ in equation (3.16), and $\frac{Dv_z}{Dt} v_z = \frac{\partial v_z}{\partial t}$ considering that $v_z \frac{\partial v_z}{\partial z} = 0$.

Finally then, the Navier-Stokes equation (3.16) takes the simple form :

$$\rho_0 \frac{\partial v_z}{\partial t} = \eta \frac{\partial^2 v_z}{\partial x^2} + \delta\rho g. \tag{3.18}$$

We limit our solution to the steady state regime, with $\frac{\partial v_z}{\partial t} \sim 0$.

3.2.2 *Modeling the heat transfer.*

The main task for our description is to model the change in density $\delta\rho$ of the fluid induced by the laser heating mechanism. The change in density is related to the change in temperature δT through the thermal expansion coefficient β (at constant pressure) with :

$$\delta\rho = -\beta \rho_0 \delta T, \tag{3.19}$$

the change of temperature $\delta T = T(r) - T_{bath}$ being the difference between the temperature at a given radial distance from the optical axis ($r = 0$) and

the unperturbed fluid temperature T_{bath}.

This change of temperature is determined along the displacement of the fluidic cell, from the heat equation :

$$\rho_0 C_p \frac{D\delta T}{Dt} + \vec{\nabla} \cdot \vec{J} = Q_L, \tag{3.20}$$

where C_p is the heat capacity of the fluid (water), $\vec{J}$ the heat flux and Q_L the heat generated (per unit of volume and time) in the cell by water absorption of the laser power.

The heat flux $\vec{J}$ is related to the temperature gradient through Fourier's law with $\vec{J} = -\lambda \vec{\nabla} T$ where λ is the thermal conductivity of water ($0.6\ W.m^{-1}.K^{-1}$). We will here restrict our description to local changes, assuming that we can neglect the convective contribution $(\vec{v}\cdot\vec{\nabla})\delta T$. Considering that for the fluid (as discussed above) $v_x \propto 0$, this assumption amounts to neglect $\rho_0 C_p (v_z \frac{\partial \delta T}{\partial z})$ with respect to Q_L, which can be done following simple estimates :

- the heat generated by water absorption of the laser beam $Q_L = A\frac{2P_0}{\pi w_0^2} e^{-r^2/a^2}$ with $a^2 = w_0^2/2$ is ca. $9.8 \times 10^5\ W.m^{-3}$ for a laser power of 35 mW with a waist of 50 μm and an absorption coefficient for water $A = 0.3 m^{-1}$ at $\lambda = 637 nm$. This estimate is done at the edge of the waist $r \propto a$ where the convective contribution is expected to be maximal.

- while the convective contribution along the z-axis $\rho C_p v_z \frac{\partial \delta T}{\delta z}$ is estimated from the typical velocities $v_z \propto 10^{-6} m.s^{-1}$ measured in the first part of the chapter. Considering temperature changes of the order of 1K over μm distance, this contribution is ca. $4.18\ W.m^{-3}$, i.e. much smaller than Q_L.

Under such assumptions, the steady state ($\frac{\partial \delta T}{\partial t} = 0$) heat equation simply writes :

$$-\lambda \vec{\nabla}^2 \delta T = Q_L,$$

that is explicitly as

$$\lambda \frac{1}{r} \partial_r [r \partial_r \delta T] = -A \frac{2P_0}{\pi w_0^2} e^{-2r^2/w_0^2}. \tag{3.21}$$

This equation can easily be solved assuming two boundary conditions :

- $r\frac{\partial \delta T}{\partial r} = 0$ on the optical axis at r=0, cylindrical symmetry of temperature gradient.
- $\delta T(r = \delta_T/2) = 0$ at a distance away from the optical axis given by the thermal boundary layer thickness δ_T.

With such boundary conditions, we solve equation (3.21) as:

$$\delta T = \frac{A.P_0}{4.\pi.\lambda}\left(-2\ln\left(\frac{2.r}{\delta_T}\right) - E_1\left(\frac{r^2}{w_0^2}\right) + E_1\left(\frac{\delta_T^2}{4w_0^2}\right)\right). \tag{3.22}$$

where $E_1[...]$ is the exponential integral. The detailed calculation to find this solution are presented in the appendix A.

3.2.3 *Thermal vs velocity boundary layer thicknesses*

The ratio between mass and thermal diffusion rates is fixed by the Prandtl number. In water, $Pr = 7$ implying that the fluid velocity induced by the change of density $\delta\rho$ is controlled by the slow thermalisation of unit volume fluid cells displaced from thermal equilibrium[47]. As a consequence, the ratio between the velocity δ_ν and the thermal δ_T boundary layer thicknesses is :

$$\frac{\delta_\nu}{\delta_T} \propto Pr^{1/2} > 1. \tag{3.23}$$

With such $Pr > 1$, the thermal boundary layer thickness simply scales as [49] :

$$\delta_T = Ra^{-1/4}L \tag{3.24}$$

where Ra is the Rayleigh number characterizing the flow driven by buoyancy for the maximal temperature change δT_{max} of the system :

$$Ra = \frac{g\beta\rho_0}{\eta\lambda}\delta T_{max}.L^3 \tag{3.25}$$

with L the characteristic length over which the heat transfer is defined. For our Gaussian laser beam heating the fluid, we will take $L \propto 2a$.

The maximum temperature change δT_{max} is given by equation (3.22) evaluated on the optical axis, at r=0. But since δ_T is itself a function of δT_{max}, this equation becomes implicit. A few approximation can however be made.

First, $E_1(x) \sim -\gamma - \ln(x)$ when $x \to 0$ with γ the Euler-Mascheroni constant. This gives from equation (3.22) :

$$\delta T_{max} \sim \frac{A.P_0}{4.\pi.\lambda}\left(2\ln\left(\frac{\delta_T}{2a}\right) + \gamma + E_1[\frac{\delta_T^2}{4a^2}]\right). \tag{3.26}$$

Of course, the thermal boundary layer extends much beyond the mere extension of the laser beam. With $\delta_T >> 2a$ therefore, $E_1[\frac{\delta_T^2}{4a^2}] \sim 0$.

We graphically solve therefore the simple equation :

$$f = IA\delta T_{max} + 1/2\ln(\delta T_{max}) + 2\ln(IB) - \gamma = 0 \tag{3.27}$$

with :

$$IA = \left(\frac{AP_0}{2\lambda\pi}\right)^{-1} = 114.2\ m^2K^{-1}$$

$$IB = \left(\frac{g\beta\rho_0}{\eta\lambda}\right)^{1/4}(2a)^{3/4} = 4\times10^{-3}\ W^{-1}.s^{-1}$$

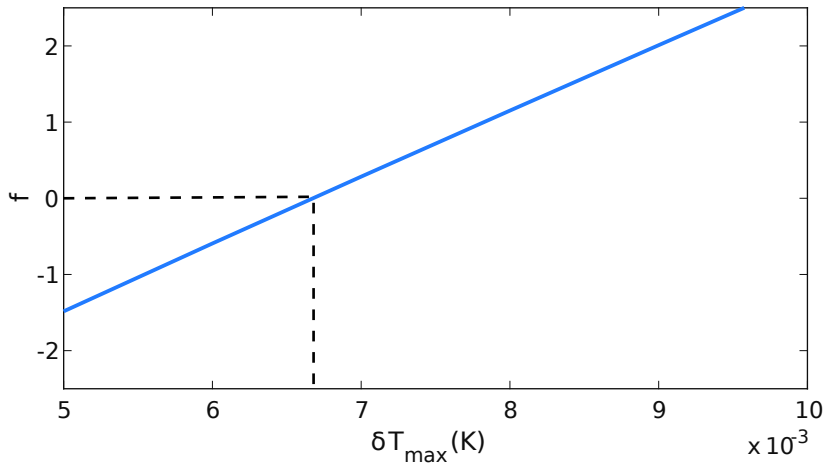

Figure 3.17 – The function f is defined in equation (3.27) and the solution is given for : $\delta T_{max} = 6.7$ mK..

The solution is determined as $\delta T_{max} = 6.7mW$ which corresponds to a thermal boundary layer thickness of $\delta_T = 0.94\times10^{-3}$m. The thickness of the corresponding velocity boundary layer follows with $\delta_v = \sqrt{Pr}\delta_T = 2.5\times10^{-3}$m.

Starting from δT_{max} along the optical axis, the full profile of the temperature change can now be calculated from equation (3.26), in the (X,Z) plane and also as a function of the laser power, a critical quantity for the experiments presented in the first part of the chapter.

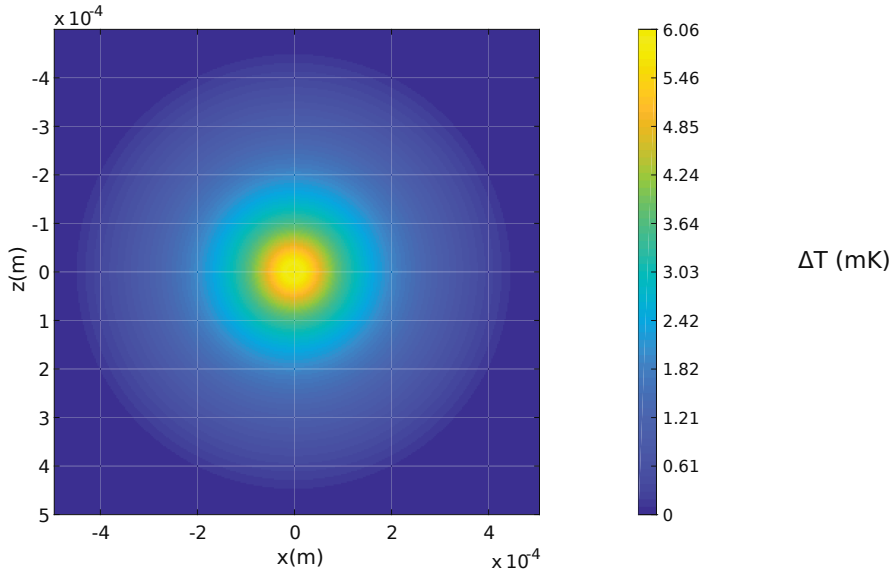

Figure 3.18 – Temperature change profile map in the $(\vec{e}_x, \vec{e}_z)$ plane for a laser power P_0= 35 mW, taking the absorption of water at $\lambda_L = 637$ nm.

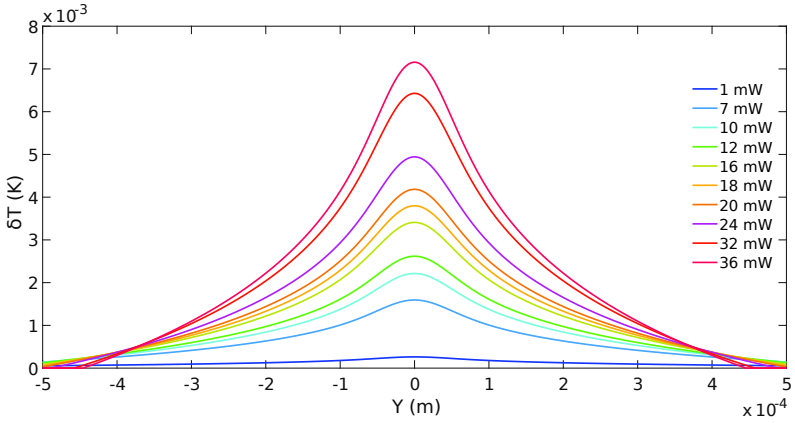

Figure 3.19 – Temperature change profiles for different laser powers ine the same conditions as in figure (3.18).

3.2.4 *Fluidic velocity profile*

Now that the temperature change δT induced by the laser is calculated, we can derive the corresponding fluid density change $\delta\rho = -\beta\rho_0\delta T$. We will thereby calculate the steady state velocity profile of the heated fluid with the thermal boundary layer δ_T from the Navier Stokes equation described above. In fact, the width Δ of the field of view of our microscope is such that $\Delta < \delta_T$. In such conditions of observation, we will approximate equation (3.26) as $\delta T(r) \sim \delta T(x)$.

Beyond the thermal boundary layer, the temperature is not evolving any more ($\delta T = 0$) so that the system to be solved is split in two regions :

$$\begin{cases} \eta \frac{\partial v_z^{(1)}}{\partial x^2} = \beta \rho_0 \delta T(x) \quad \text{for} \quad |x| < \frac{\delta_T}{2} \\ \eta \frac{\partial v_z^{(2)}}{\partial x^2} = 0 \quad \text{for} \quad \frac{\delta_T}{2} < |x| < \frac{\delta_v}{2} \end{cases} \tag{3.28}$$

keeping in mind that in water, $\delta_v > \delta_T$. We impose the boundary conditions for the velocity and its derivative as :

- $\left.\frac{\partial v_z^{(1)}}{\partial x^2}\right|_{x=0} = 0$
- $v_z^{(2)}\left(\pm\frac{\delta_v}{2}\right) = 0$, considering that the fluid is at rest at the end of the velocity boundary layer,

and we impose at the merger of the thermal and velocity boundary layers the continuity of v_z and $\frac{\partial v_z}{\partial x}$:

- $\left.\frac{\partial v_z^{(1)}}{\partial x^2}\right|_{x=\pm\frac{\delta_T}{2}} = \left.\frac{\partial v_z^{(2)}}{\partial x^2}\right|_{x=\pm\frac{\delta_T}{2}}$
- $v_z^{(1)}\left(\pm\frac{\delta_T}{2}\right) = v_z^{(2)}\left(\pm\frac{\delta_T}{2}\right)$

The system (3.28) supplemented by the boundary and continuity conditions yields the velocity profile $v_z(|x|)$ from the optical axis to the end of velocity boundary layers. This profile is drawn on figure (3.20).

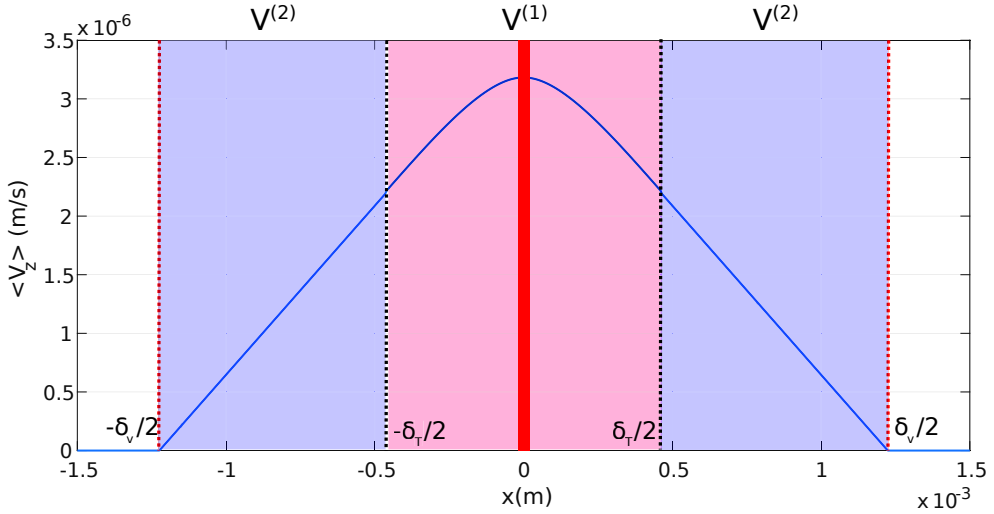

Figure 3.20 – Velocity profile for P_0 = 36 mW, the maximum velocity is in the center of the beam V_{max}=3.2 µm/s. The black and the red dotted line shows the thermal and the velocity boundary layer, respectively. The blue region is the region where the temperature gradient drops to zero, the light red region is the region where the gradient is non zero, and the dark red line represents the width Δ of the field of view of the imaging system with $\Delta = 11.4$ µm.

We have highlighted in figure (3.20) how the width of the microscope field of view probes only a small region of the thermal boundary layer where the induced fluid velocity can be considered as uniform, hence providing the appropriate conditions for performing experiments under laminar flows.

The predicted convective velocity on the optical axis $v_{max} = v_z(0) = 3.2\ \mu m.s^{-1}$ for an irradiating laser power $P0 = 35\ mW$, thus associated with a temperature change of $\delta T = 7,3.10^{-3}$ K, appears to be consistent with our experiments, where we measured -see figure (3.5) :

$$\begin{aligned} < V_z >_{P_{Low}} &= -1.5 \pm 0.25\ \mu m/s, \\ < V_z >_{P_{High}} &= 1.5 \pm 0.3\ \mu m/s, \\ \delta < V_z >_{exp} = < V_z >_{P_{High}} - < V_z >_{P_{Low}} &= 3 \pm 0.55\ \mu m/s. \end{aligned} \tag{3.29}$$

These values clearly shows that in our experiments, the convective motion of the fluid dominates over diffusive transport. This is quantified through the Péclet number. Figure (3.21) display on the evolution of Pe as a function of the convective velocity under our experimental conditions.

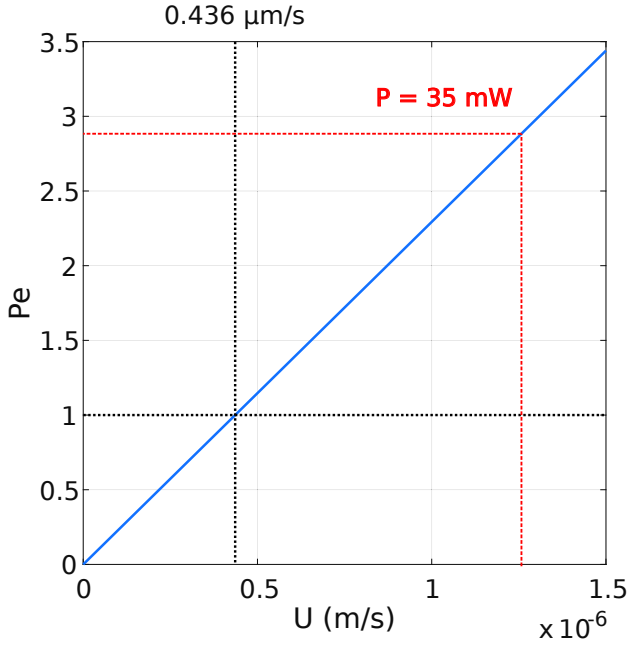

Figure 3.21 – Dependence of Peclet number on the flow velocity. When the flow velocity exceeds 0.436 µm/s, the advective motion starts dominating over the the diffusive motion. The red dotted line correspond to our experimental regime of induced convection with $P_{High} = 35\ mW$

3.3 CONCLUSION

The existence of the three different regimes depending on the laser irradiation has been demonstrated by tracking the colloidal assembly using Single Particle Tracking methods. Two ballistic regimes have been observed for the lower and higher limits of laser power, and a diffusive regime mimicking free Brownian motion in all directions.

The diffusion coefficient was then measured and we demonstrated that the diffusion coefficient does not depends on the laser power.

In addition, a model was proposed to calculate the convective drag velocity induced by the heating of water by laser irradiation, which combines Navier-Stokes and Fourier's equations. The predicted convective flow velocity is in good agreement with the estimators of the mean velocity measured from Brownian trajectories.

The possibility to compensate sedimentation using a laser that irradiate the fluid is an interesting example where a buoyancy effect is induced by changing the fluid density through an increase of the local temperature of the fluid. In other words, the laser, used for tracking the particle trajectories within the colloidal suspension, injects a given quantity of heat that is fixed by its power. Our results describe therefore dynamical regimes of a colloidal suspension which steady states are modified by this external injection of heat. In the next chapter, we will show that, beside heat, the irradiating laser can also inject work on the system. This takes the form of the action of optical forces on the colloidal particles which can be measured with high resolution and levels of confidence by using similar statistical tools.

4

MEASURING RADIATION PRESSURE AT A FEMTO NEWTON RESOLUTION LEVEL WITH BROWNIAN COLLOIDS

Manipulation of particles at the micro and nano scales through light-induced forces is most efficient at low Reynolds number [50, 51], because of buoyancy and the dominance of viscous force over inertial force. In such conditions, Brownian motion becomes an efficient tool for measuring small forces. This seems paradoxical. On the one hand indeed, thermal agitation that drives Brownian motion is an inevitable source of noise. But on the other hand, this noise has equal intensity at all frequencies so that the statistical properties of Brownian motion follow specific laws. In the first section of this chapter, we will show how these laws can lead to efficient methods for measuring small forces on a Brownian micro particle. We will then discuss a statistical force resolution criteria valid for an ensemble of Brownian particles. Finally, we will show experimental results obtained for measuring radiation pressure force applied on an ensemble of Brownian particles. We will explain how optical force field profiles can be reconstructed through such type of measurements involving Brownian motion.

4.1 OPTICAL FORCES MEASUREMENT.

The mechanical interaction between light and matter is very weak at our scales. Nevertheless, at the micro and nano scales the force resulting from momentum exchange between photons and particles can become significant. Observing and measuring such forces has a long history. In 1970, A. Ashkin, had the idea to exploit such mechanical action in order to immobilize and trap micro-particles in water at room temperature [52]. Using radiation pressure force to trap micro-particles, Ashkin *et al.*, were able to induce a ballistic velocity $V_{Particle}^{ballistic} = 26 \pm 5\mu m/s$ on the particle under low laser power P = 19 mW. Such manipulation of micro particles

led to a lot of practical applications [53], among which of course Ashkin's optical tweezers for which he was awarded the 2018 Nobel prize is physics.

In our experiments we are working with Melamine micro particles of radius $R = 0.47\mu m$. We present in the next section the theoretical framework for radiation pressure on particle for which the size is comparable to the wavelength of the light field.

4.1.1 *Optical forces in Mie regime*

The different regimes of light scattering on a homogeneous sphere can be classified by comparing the diameter $a = 2R$ of the sphere to the wavelength of the light λ interacting with the particle:

- Rayleigh scattering regime : $a \ll \lambda$, where the amplitude of the scattered light is proportional to $1/\lambda^2$, and the volume of the particle.
- Ray optics regime : $\lambda \gg a$, where the beam propagate according geometrical optics laws.
- Mie scattering regime : $\lambda \propto a$. This is the regime of our experiments. Shape and permetivity of the sphere determine the scattering patterns through the motion of scattering and extinction cross sections.

In order to compute the radiation pressure in the regime of Mie scattering, we need to calculate the extinction σ_{ext}, scattering σ_{scat}, and absorption σ_{abs} cross sections of the spherical particles involved in the problem[54–56]. In the case of spherical particles, radiation pressure can easily be evaluated from the "radiation pressure cross section" [57] :

$$\sigma_{radiationpressure} = \sigma_{ext} - < \cos\theta > \sigma_{scat}, \tag{4.1}$$

where $< \cos\theta >$ is the asymmetry factor who characterize the relative importance of forward vs. backward scattering and $\sigma_{ext} = \sigma_{scat} + \sigma_{abs}$ (in our case $\sigma_{abs} = 0$ because we work with dielectric particles) . We thus get the mean radiation pressure force applied in the Mie regime as:

$$\begin{aligned} F_{RP}^{Mie} &= \frac{\sigma_{RP}\mathcal{P}_{inc}}{c}, \\ &= \frac{P}{\pi w_0^2 c}\sigma_{ext}(1 - < \cos\theta >), \end{aligned} \tag{4.2}$$

where P is the power of the incident beam in (W), w_0 is the waist of the beam (m) , and c is the speed of light. We use the online Mie scattering calculator[1] to compute Mie cross sections. For our experimental conditions, we get :

$$F_{RP}^{Mie} = 0.98610^{-13}P. \tag{4.3}$$

We will compare this prediction to our measurements in section (4.6).

4.1.2 *Optical Setup*

The optical setup is sketched in chapter 3 figure (2.1). For all our force measurements, we set the input polarization at the PBS at 45° so that the power in each beam is the same. After that, we can finely tune the power difference ΔP in order to increase the power in one arm and decrease the power in the other arm, keeping the total power P_{tot}

4.2 BROWNIAN MOTION IN AN EXTERNAL FORCE FIELD

In this section we detail our method of measurement used to extract the features of the external force field applied on a Brownian micro-particle [3, 58]. We consider a single particle of a diameter $d = 2R$, made in a material of density ρ_p immersed in water at room temperature. The particle undergoes Brownian motion due to thermal fluctuations. In the following we will present the dynamical properties of Brownian motion.

4.2.1 *Langevin equation*

Langevin equation is the stochastic version of Newton second law. It consists in describing the effect on the particle due to thermal excitations of the fluid as the sum of a random force $F_{Thermal}$ and a viscous force given by the Stokes drag $-\gamma v$, with v the velocity of the particle in the fluid and $\gamma = 6\pi\eta R$, η the dynamic viscosity of the fluid. Both forces are related through the Fluctuation Dissipation theorem with $F_{thermal}(t) = \sqrt{2k_BT\gamma}L(t)$ where k_BT is the thermal energy and $L(t)$ is a random (Wiener) process with the following properties :

I. $L(t)$ is erratic, rapidly fluctuating function with :

$$< L(t) >= 0, \tag{4.4}$$

1 https://omlc.org/calc/mie_calc.html

<...> is the average over all the realization of the process.

II. L(t) does neither influence L(t<t') nor L(t>t') :

$$< L(t)L(t') >= \delta(t-t'), \tag{4.5}$$

the realizations of L(t) are uncorrelated in time. With this property the process is called a Markov process : the future state x_{n+1} depends only on the present state x_n and not on the past $\{x_i\}_{i=0,1,2,...,n-1}$ ones.

III. L(t) is a Gaussian process $\Leftrightarrow$ $< L(t) >$ and $< L(t)L(t') >$ characterize the process completely.

A random process with the properties (I), (II) and (III) is called "Gaussian White Noise".

From Newton's second law, the motion of the particle is then given by the simple equation:

$$m\dot{v} = -\gamma v + F_{Therm}(t) + F_{ext} \tag{4.6}$$

including the presence of an external (non stochastic) force F_{ext} exerted on the particle. Note that equation (4.6) is a projection taken on a given axis of the reference frame. In our experiments, following its description given in chapter 2 figure (3.1), the external optical force is exerted on the particle along the optical Y-axis. Equation (4.6) is defined over the momentum relaxation frequency $\Omega = \frac{\gamma}{m}$. In our conditions, working with a particle of radius $R = 470$ nm immersed in water with $\eta = 0,89.10^{-3}$ Pa.s one derives $\Omega = 1,36.10^6$ Hz. This high value clearly indicates that in the spectral bandwidth available in our experiments [0.01 to 10^3] Hz, the inertial term $m\dot{v}$ in equation (4.7) can safely be neglected . This corresponds to the low Reynolds number limit of the equation of motion and corresponds to the "over-damped" regime of Brownian motion.

4.2.2 *Free Brownian Motion in the over-damped regime*

With no external force, i.e $F_{ext} = 0$, the Brownian motion of the particle is said to be "free" and Langevin equation is simply :

$$\gamma \frac{\partial Y}{\partial t} = \sqrt{2k_B T\gamma} L(t), \tag{4.7}$$

where the left hand side represents the dissipation of energy as a result of friction. The right hand side represents the fluctuations due to the

collisions between the molecules of the solvent that keep the particle moving. The probability to find the particle at the position x at time t is given by the diffusion equation first derived by Einstein [59] :

$$\frac{\partial \mathcal{P}(r,t)}{\partial t} = D\frac{\partial^2 \mathcal{P}(r,t)}{\partial x^2}, \tag{4.8}$$

where $D = \frac{k_B T}{\gamma}$ is the diffusion coefficient, and where r can stand either for the spatial coordinate variables Y and Z. The solution of equation (4.8) is the Gaussian probability density function (PDF) :

$$\mathcal{P}(r,t) = \frac{1}{\sigma_r\sqrt{2\pi}} e^{-(\frac{r-\mu_r}{\sigma_r})^2}, \tag{4.9}$$

where $\sigma^2 = 2Dt$ is the variance of the position PDF. Experimentally we track the trajectories Y(t) and Z(t) projected along Y and Z axis (see chapter 1), where t is sampled at f=120 Hz. In this way we generate a series of positions along both axes

$$Y(\tau_n) = Y_n, \quad Z(\tau_n) = Z_n \tag{4.10}$$

where $Y(\tau_n)$ and $Z(\tau_n)$ are the measured positions of the particle recorded in the frame n at each time $\tau_n = n\Delta t$, where $\Delta t = 1/f$ is the time between two successive frames. We then construct experimentally the discrete version of the PDF (4.9):

$$\mathcal{P}(r_n,t_n) = \frac{1}{\sigma_{r_n}\sqrt{2\pi}} e^{-(\frac{r_n}{\sigma_{r_n}})^2}, \tag{4.11}$$

by measuring all the trajectories from the same initial position (0,0) at time step t_n.

From the dynamic point of view, the discrete version of (4.7) gives the Root Mean Squared RMS displacement due to thermal fluctuations:

$$\begin{aligned} &\frac{1}{\Delta t}(r_{n+1} - r_n) = \sqrt{2D}L_n, \\ &< (r_{n+1} - r_n) > = \sqrt{2D}\Delta t < L_n >, \text{with} \quad < L_n >= 0 \\ &(r_{n+1} - r_n)^2 = 2D\Delta t^2 L_n^2. \end{aligned} \tag{4.12}$$

where D is the diffusion coefficient defined by Stokes-Einstein equation. This last relation can be connected to the MSD, defined (Chapter I for more details) as:

$$< (r_{n+1} - r_n)^2 >_j = \frac{\sum_{i=1}^{N_I} (r_{i+j} - r_i)^2}{N_I} = 2D\Delta t, \tag{4.13}$$

where $\tau_j = j\Delta t$ defines the time lag over which we compute the mean squared displacement and N_I is the number of temporal intervals over which we calculate the mean squared displacement.

From (4.12) and (4.13) we get :

$$\begin{aligned} < (r_{n+1} - r_n)^2 > &= 2D\Delta t^2 < L_n^2 > = 2D\Delta t, \\ \Rightarrow < L_n^2 > &= \frac{1}{\Delta t}. \end{aligned} \tag{4.14}$$

Hence we know the variance[2] of L_n:

$$V(L_n) = < L_n^2 > - < L_n >^2 = \frac{1}{\Delta t}. \tag{4.17}$$

In order to work with discrete random variable following normalized normal law $\mathcal{N}(0,1)$, we replace L_n by :

$$l_n = L_n \sqrt{\Delta t} \tag{4.18}$$

hence with $< l_n >= 0$ and $< l_n l_{n'} >= \delta_{nn'}$, where $\delta_{nn'} = 0$ when $n \neq n'$ and $\delta_{nn'} = 1$ when $n = n'$.

Figure(4.1) panel (a) displays the experimental 1D trajectories along both the Y and Z axes, reported from a common $(0,0)$ origin.. Panel (b) displays the corresponding PDF of positions. Projected along the Y-axis, the motion of the particles does not experience any external force : the Brownian motion is therefore free. As seen the mean displacement in indeed zero and the variance grows linearly with respect to time as expected from Einstein's relation $\sigma^2 = 2Dt$. Along the vertical axis, the

2 The variance is defined as follows :

$$V(X) = E(X^2) - E(X)^2, \tag{4.15}$$

where $m = E(X) = \sum_{i=1}^{n} p_i X_i$ is the expected value of the random variable X, and p_i are the probabilities that $X = x_i$. The standard deviation is defined as:

$$\sigma_X = \sqrt{V(X)}. \tag{4.16}$$

trajectories and the evolution of the position PDF appear clearely different in panels c) and d) of figure (4.1), manifesting along this Z-axis the presence of gravity as an external force field.

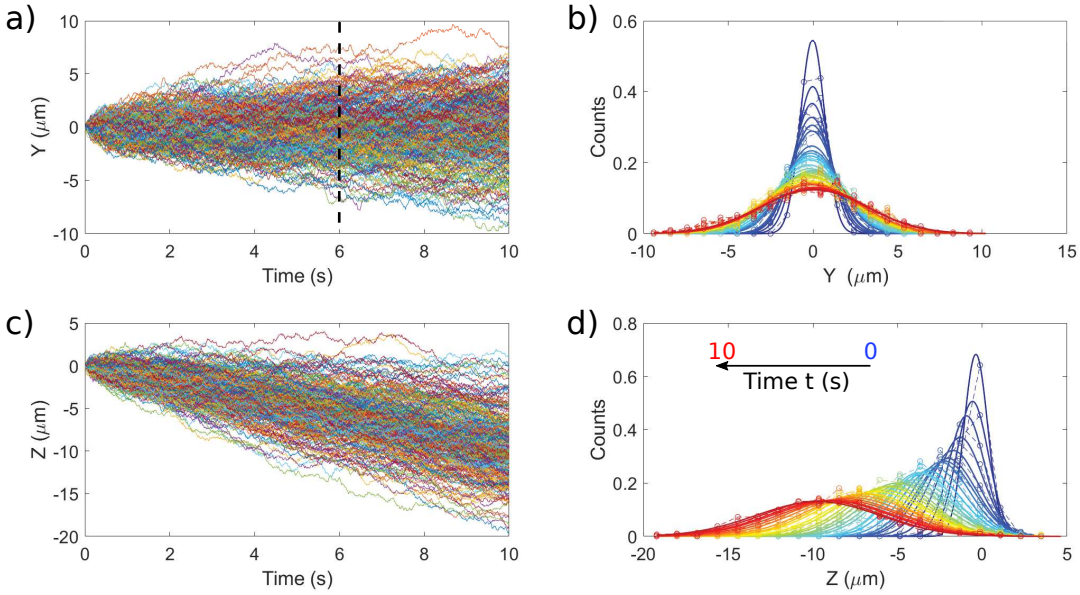

Figure 4.1 – Experimental Brownian trajectories projected along the horizontal Y-axis in panel a), and along the vertical Z-axis in panel c). The PDF of positions $P(x,t)$ shown in panels b) and d) are constructed by the histogram of position at a given time t (The black dashed line in panel a) is an example of the statistical ensemble, consisting of the positions of the particles at time t, over which we construct the histogram). The Y and Z axes are the same axes defined in figure (3.1). The counts in panels b) and d) are normalized by the total number of trajectories.

4.2.3 *External conservative force on a Brownian particle*

The PDF of a Brownian particle subjected to an external force field F_{ext} (constant in space and time) follows the Smoluchowski diffusion equation[3, 60] :

$$\frac{\partial \mathcal{P}(r,t)}{\partial t} = D\frac{\partial^2 \mathcal{P}(r,t)}{\partial r^2} - \frac{1}{\gamma}\frac{\partial}{\partial r}(F_{ext}\mathcal{P}(r,t)). \tag{4.19}$$

The solution in that case is, just like for the case of free Brownian motion, a Gaussian PDF :

$$\mathcal{P}(r,t) = \frac{1}{\sigma_r\sqrt{2\pi}} e^{-(\frac{r-\mu_r^{ext}}{\sigma_r})^2}, \tag{4.20}$$

but this time with a mean shifted from zero by a mean displacement μ_r^{ext} simply related , in the over-damped regime, to the external force through

$\mu^{ext} = \frac{F_{ext}}{\gamma} t$ where t is the time of observation. This type of time dependent PDF is observed in panel d) of figure (4.1) in the situation of our Brownian particles diffusing under the gravity force field. The shift of the mean of the distribution with time is clearly seen. Remarkably, the variance of the distributions remain determined by Einstein's relation and therefore are equal to the one presented panel b) where there is no external force field.

From Einstein coarse-grained approach, the positions are considered as rapidly fluctuating stochastic variables over a characteristic time τ_E. Langevin coarse-grained time scale τ_L for which the velocities are considered fast and fluctuating stochastic variables, is smaller than Einstein's characteristic time τ_E. In terms of stochastic process from one hand, Langevin used an Ornstein-Uhlenbeck process [61], and from the other hand Einstein used a Wiener process [62] to analyse the trajectory of a Brownian particle. The two points of view are equivalent. In our analysis, we are more interested in the dynamics of the particles so we will work with Langevin approach. In that case, Langevin equation (4.6) in an external force field F_{ext} is written for an elementary displacement monitored on a time interval Δt :

$$\begin{aligned} < r_{n+1} - r_n > &= \frac{F_{ext}}{\gamma}\Delta t + \sqrt{\frac{2k_B T \Delta t}{\gamma}} < l_n >, \text{ where } < l_n >= 0 \\ &= \mu^{ext}, \end{aligned} \tag{4.21}$$

where μ^{ext} is the ballistic contribution to the mean displacement due to the applied external force. Experimentally, using a finite set of N_t displacements, we never measure the actual mean value μ^{ext} but only an estimator of it, as discussed in chapter one. The estimator of the ballistic mean is given by averaging over the ensemble of N_t detected displacement as :

$$\overline{\mu}_{\Delta r} = \frac{\sum_{n=1}^{N_t} r_{n+1} - r_n}{N_t - 1}. \tag{4.22}$$

with Δr is the ensemble of N_t displacements.

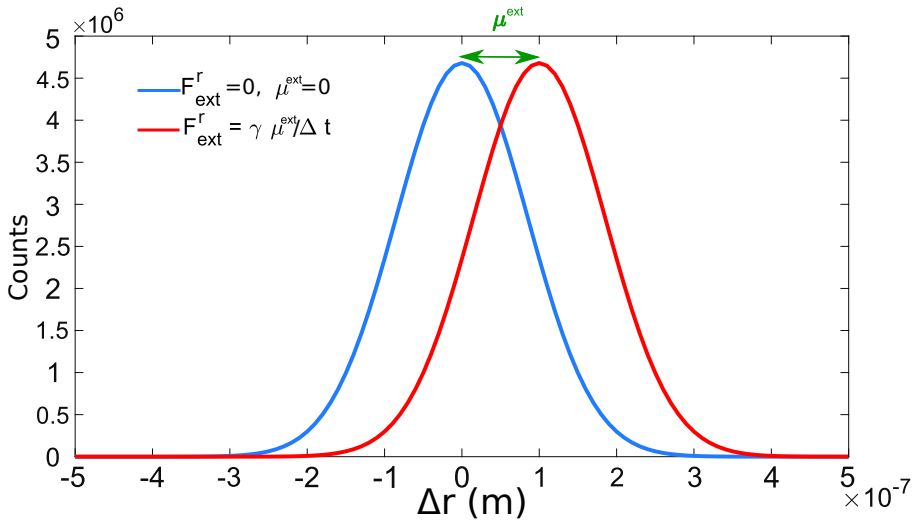

Figure 4.2 – Simulated Displacement distribution $P(\Delta r, \Delta t)$ for a Brownian particle. Blue line : free Brownian motion without external force, red line : Brownian motion under an external force F_{ext} directed along r, with the corresponding μ^{ext} ballistic shift.

From the estimator, we can obtain a mean value for the external force applied on the particle, as :

$$< F^r_{ext} >_{\Delta r} = \gamma \frac{\overline{\mu}_{\Delta r}}{\Delta t} = \frac{\gamma}{\Delta t} \frac{\sum_{n=1}^{N_t} r_{n+1} - r_n}{N_t - 1}. \tag{4.23}$$

4.2.4 *Measurement uncertainties*

There are two statistical quantities that characterize measurement errors. The first one is the standard deviation σ (SD), which gives the dispersion of a random variable around its mean value. SD quantifies the variability of the measurement with respect to the mean value of the statistical ensemble the measurement is drawn from. The second quantity is the standard error (SE) which measures the precision by which the mean of the sample can be determined. The SE therefore gives the uncertainty of a measurement performed. The standard error is defined from the standard deviation, as now discussed.

Let us consider the example of our statistical sample composed of N_t Brownian displacements $\{\Delta y\}_N$ measured on the Y-axis as the direction

along which the force F_{ext} is exerted in our experiment. The variance is defined as follows :

$$\sigma^2_{\Delta y} = \frac{1}{N-1}\sum_{i}^{N}(\Delta y_i - \mu_{\Delta y})^2 \tag{4.24}$$

where $\Delta y_i = y_{i+1} - y_i$ and $\mu_{\Delta y} = \frac{\sum_{i=1}^{N_t}\Delta y_i}{N_t - 1}$. The SD $\sqrt{\sigma^2_{\Delta y}} = \sigma_{\Delta y}$ can obviously be defined even though the random variable is not normally distributed. The meaning of the SD is that 95% of the random variables falls within 2σ from the sample mean $\mu_{\Delta y}$.

Now, the value of the SD of the means themselves expected from several samples can be estimated from a single sample through the standard error defined as :

$$SE(\Delta y_i) = \frac{\sigma_{\Delta y}}{\sqrt{N}}, \tag{4.25}$$

where N_t giving the sample size. The SE thus measures the uncertainty of a statistical dtermination of the external force and is used to compute confidence intervals given as :

- for a 68% confidence interval :

$$\left[\mu_{\Delta y} - \frac{\sigma_{\Delta y}}{\sqrt{N_t}}; \mu_{\Delta y} + \frac{\sigma_{\Delta y}}{\sqrt{N_t}}\right] \tag{4.26}$$

- for a 95 % confidence interval :

$$\left[\mu_{\Delta y} - 2\frac{\sigma_{\Delta y}}{\sqrt{N_t}}; \mu_{\Delta y} + 2\frac{\sigma_{\Delta y}}{\sqrt{N_t}}\right] \tag{4.27}$$

- for a 99.7% confidence interval :

$$\left[\mu_{\Delta y} - 3\frac{\sigma_{\Delta y}}{\sqrt{N_t}}; \mu_{\Delta y} + 3\frac{\sigma_{\Delta y}}{\sqrt{N_t}}\right] \tag{4.28}$$

The interpretation of the confidence interval is simple: if we repeat the measurement there is 95% chance that the mean value falls within the confidence interval and 5% that the mean value is outside the confidence interval.

It is then clear that in order to determine with the best resolution the external force field an interesting strategy is to increase the size of the statistical sample over which we estimate the mean ballistic displacement. A simple way to do this is to concatenate all the measured displacements

in one large ensemble of displacements[3]. We then reconstruct one single long trajectory and estimate the mean ballistic displacement induced by the external force. However, some important underlying assumptions are hidden behind the use the concatenation strategy :

- I) The particles are all indiscernible : this is only true to a certain extent, essentially due to the unanvoidable dispersion in particles radii as discussed in chapter I.
- II)The processes are stationary : statistical distributions are invariant though time translation.
- III) The system is ergodic[3] : time average and ensemble average are equal (converge to be equal in the long time limit).
- IV) The background noise remains spatially the same over the total measurement time.

We will verify in the following that assumptions II), III) and IV) correspond indeed to our experimental conditions. This will allow us to exploit the concatenation strategy at the end of this chapter.

4.3 STATIONARITY AND ERGODICITY ASPECTS

In order to to verify the stationary feature of the system, we will look at the evolution of the PDF of position $\mathcal{P}(r,t)$ and the PDF of displacement $\mathcal{P}(\Delta r,\Delta t)$ with respect to time. A distribution $\mathcal{P}(r,t)$ will be defined as stationary if

$$\mathcal{P}(r,t+T)=\mathcal{P}(r,t), \tag{4.29}$$

for all chosen time-delays T. From this definition, it is clear that the position based (r,t) or displacement based (Δr,Δt) distribution yield different results.

4.3.1 *PDF of position*

For Free Brownian motion, as discussed above, the position-based PDF takes specific form $\mathcal{P}(r,t)=\mathcal{N}(0,2Dt)$, corresponding to a normal distribution of mean $\mu_r=0$ and time dependent variance $\sigma_r^2=2Dt$. For Brownian motion under external force field F_{ext} [3], $\mathcal{P}(r,t)=\mathcal{N}(\frac{F_{ext}}{\gamma}t,2Dt)$

3 Composed of two greek words : Ergon which means Energy or work, and hodos which means path or trajectory.

where now the mean evolves in time as the manifestation of the ballistic contribution of F_{ext} on the Brownian motion. These evolutions are clearly seen through our experiments, as discussed on figure (4.1). We will compute the PDF of position by constructing the probability distribution of position at a given time t. We start, for a fixed laser power P_i, by concatenating the detected trajectories into a single long trajectory $\mathcal{T}_{P_i}$. In figure (4.3) are presented the concatenated trajectories $\mathcal{T}_{P_i}$ in the three different regimes. At t=0, $\mathcal{T}_{P_i}$ starts at (0,0). The ballistic contribution dominates the motion of the particle in the sedimentation and convective regimes, namely for $P_i^s = \{1mW\}$ for the sedimentation regime, and $P_i^c = 36mW$ for the convective one. In contrast, the motion is "freely" diffusive in the suspension regime for a laser power of $P_i^{Sus} = 24mW$. We note that the length of the trajectory in the convective regime is larger because of the convective flow recycles the number of particles entering the field of view of our microscope.

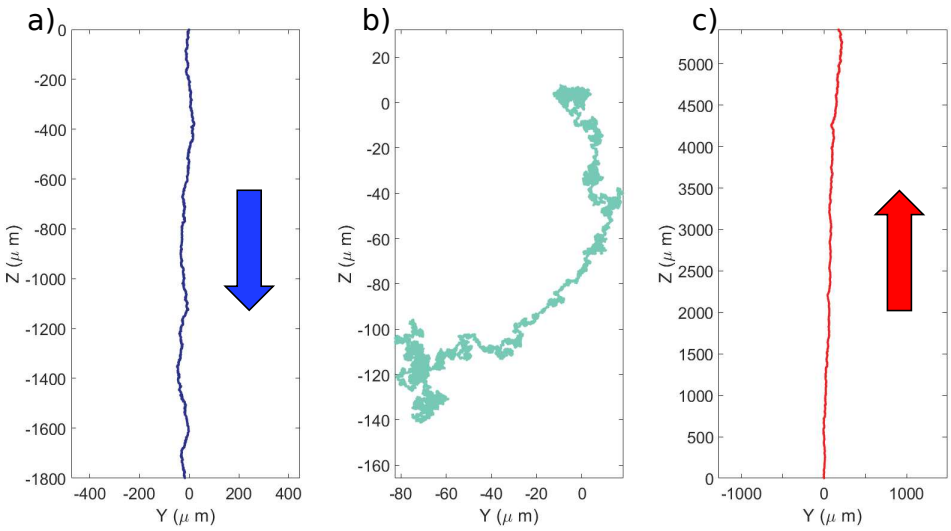

Figure 4.3 – Panel a) shows the concatenated trajectory over 1830s under laser illumination of power $P = 1mW$, the sedimentation dynamics is clearly seen. In panel b) the laser power is $P = 24mW$ and the duration of the trajectory is 1170s, and the dynamic of the trajectory resembles free Brownian motion. The panel c) displays the concatenated trajectory for a laser power $P = 36mW$ with a duration of 5070s and the convective flow dominates the motion. We use Melamine spheres $R = 470\ nm$ to conduct this experiment.

In order to verify the stationarity, we sub-sample $\mathcal{T}_i$ into N_{sub} sub trajectories. This essentially defines a time delay T_{sub}. We then look at the evolution of the statistical properties of successive $\mathcal{T}_{N_{sub}}$ sub-trajectories, in other words for successive multiple values of T_{sub}. This strategy is described in figure (4.4).

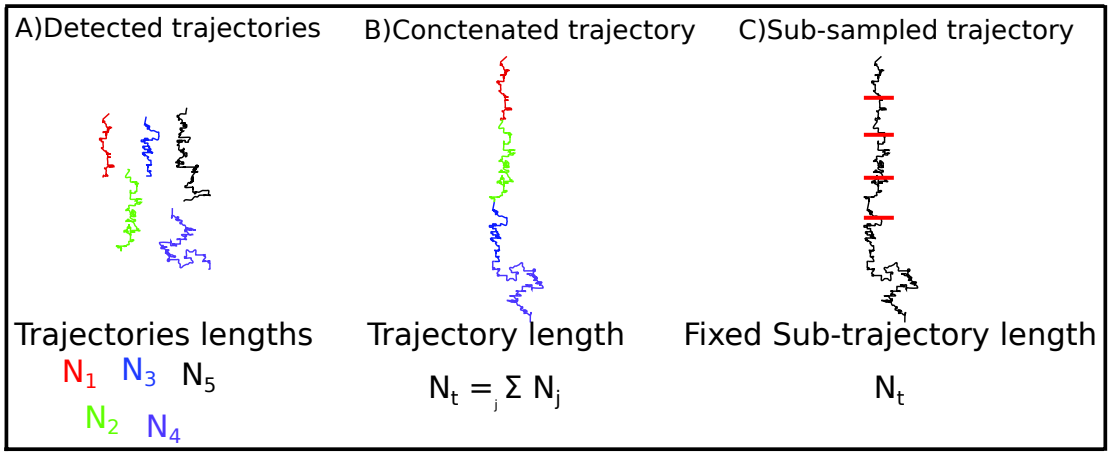

Figure 4.4 – Sketch of the concatenation strategy starting from individual trajectories first, we link the tracked trajectories as shown in panel b). Then, for a chosen time delay T_{sub} we divide the concatenated trajectory into equal trajectories. The number of sub trajectories is by construction defined from the ratio between the total duration of the concatenated trajectory and T_{sub}.

Figure (4.5) display sub trajectories along the Y and Z axes. As expected along the Y-axis, the particles perform free Brownian motion, and along Z, the ballistic contributions from gravity and convection are clearly seen.

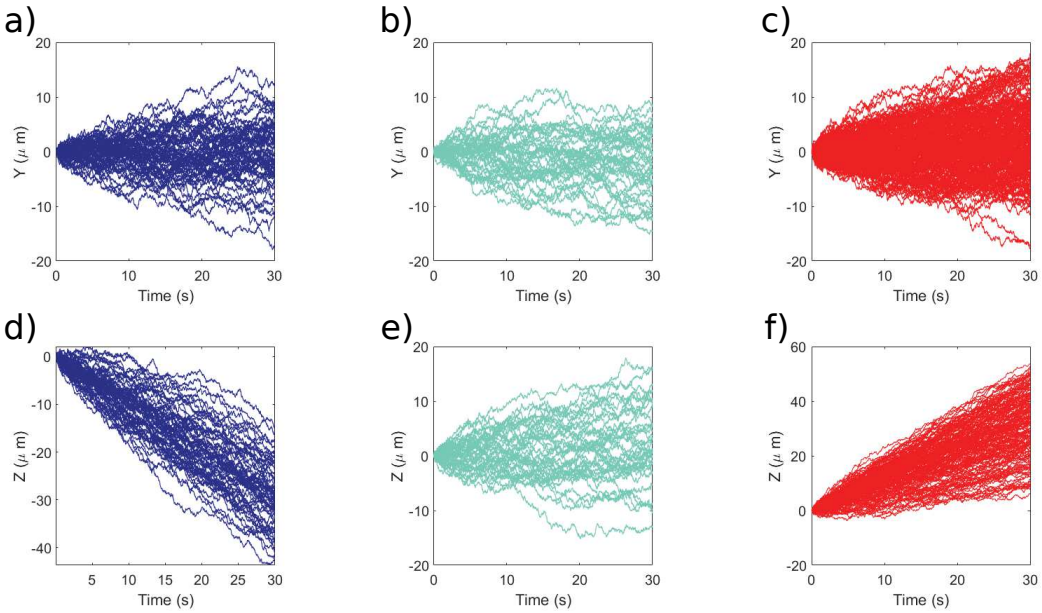

Figure 4.5 – 1D sub-trajectories along Y and Z axes, corresponding to the trajectories displayed in figure (4.3). The drift seen in panels d) and f) is induced by sedimentation and convective flow respectively. The free Brownian character of the suspended regime is clearly seen in panels b) and e). The number of sub-sampled trajectories for the sedimentation, suspension and convective regimes are respectively 61, 39 and 169.

The evolution of the PDF of positions in the three regimes are presented in figures (4.6) for all the N_{sub} realizations. In the three regimes, the PDFs of positions along Y are centered around 0, confirming that the particle is seen undergoing free Brownian motion when its motion is projected along the Y-axis. The PDFs of positions along Z show in contrast a clear drift from 0, revealing the ballistic contribution in the low and high power limits from gravity and convection respectively. In the suspended regime, the particles experience free Brownian motion along both Y and Z axes. In addition to that, and as expected for $\mathcal{P}(r,t)$, the variance widths of the PDFs of positions evolve with time.

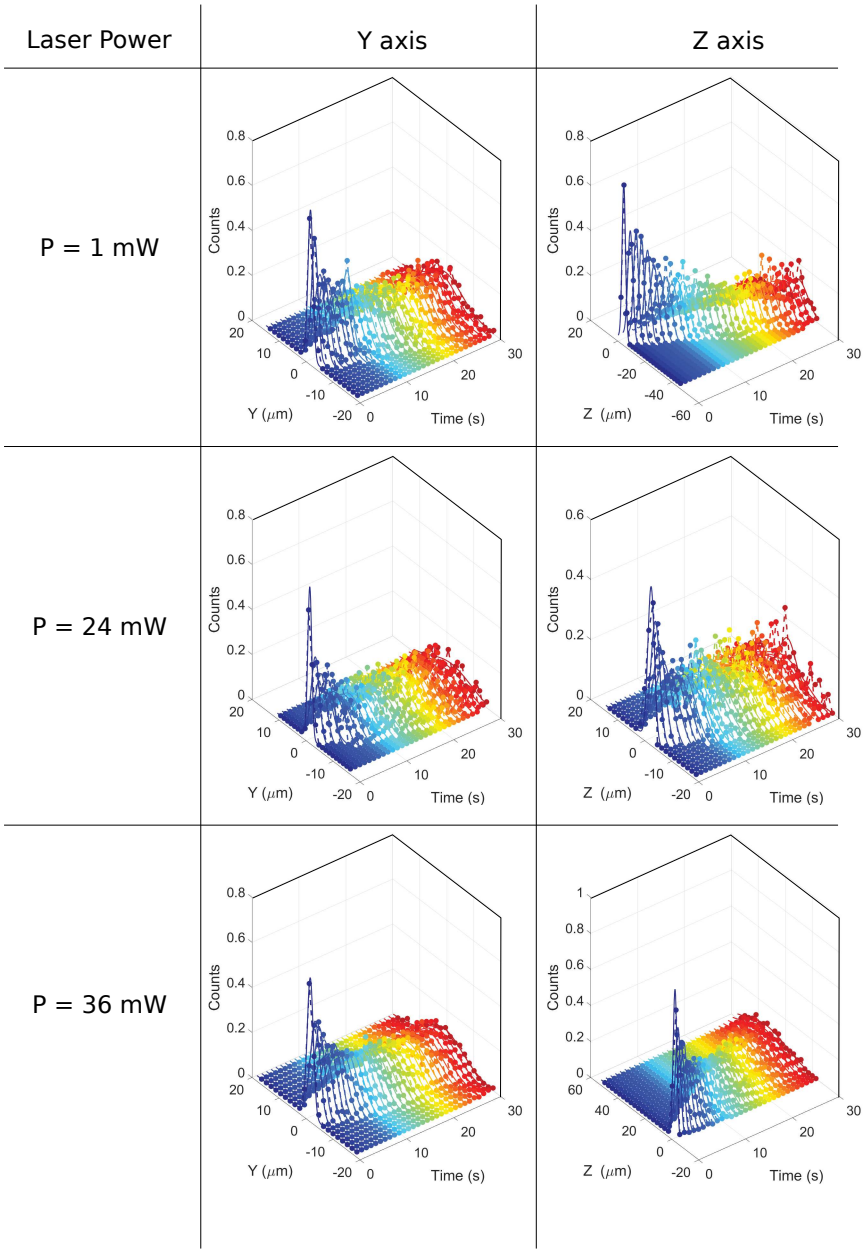

Figure 4.6 – Position based PDFs in the three regimes : sedimentation (P=1 mW), suspension (P=24 mW) and convection for Melamine beads (R=470 nm). The PDFs are computed the same way presented in labels b) and d) of figure (4.1) by adding the time as a third dimension.

The time evolution of the mean and the variance of $\mathcal{T}_{N_{Sub}}$ sub trajectories in the three regimes are presented in figure (4.7). The slope, in panel a), gives a measure of the mean ballistic velocity $\frac{F_{ext}}{\gamma}$, clearly in agreement with what is expected from the distribution of Brownian motion under external force field. The same slope, in panel b), corresponds to the diffusion coefficient. Here, the data are more noisy which is a consequence of the strong impact of the low signal-to-noise ratio on the

variance of the distribution, as discussed in the first chapter. In this context of position based PDF, stationarity has to be understood from the "single" slope character of the mean and variance time evolutions. In panel c), the slope is close to zero, which is a clear evidence of suspension and free Brownian motion along Y and Z axis. The slope in panel d), is similar to the slope in panel b) confirming the stationary aspect. Furthermore, in panel f) the strongly non linear behaviour of the variance along z in the convective regime reveals a non stationary dynamics at play. In contrast, and remarkably, the dynamical evolution along the Y-axis remains stationary as seen in panel e).

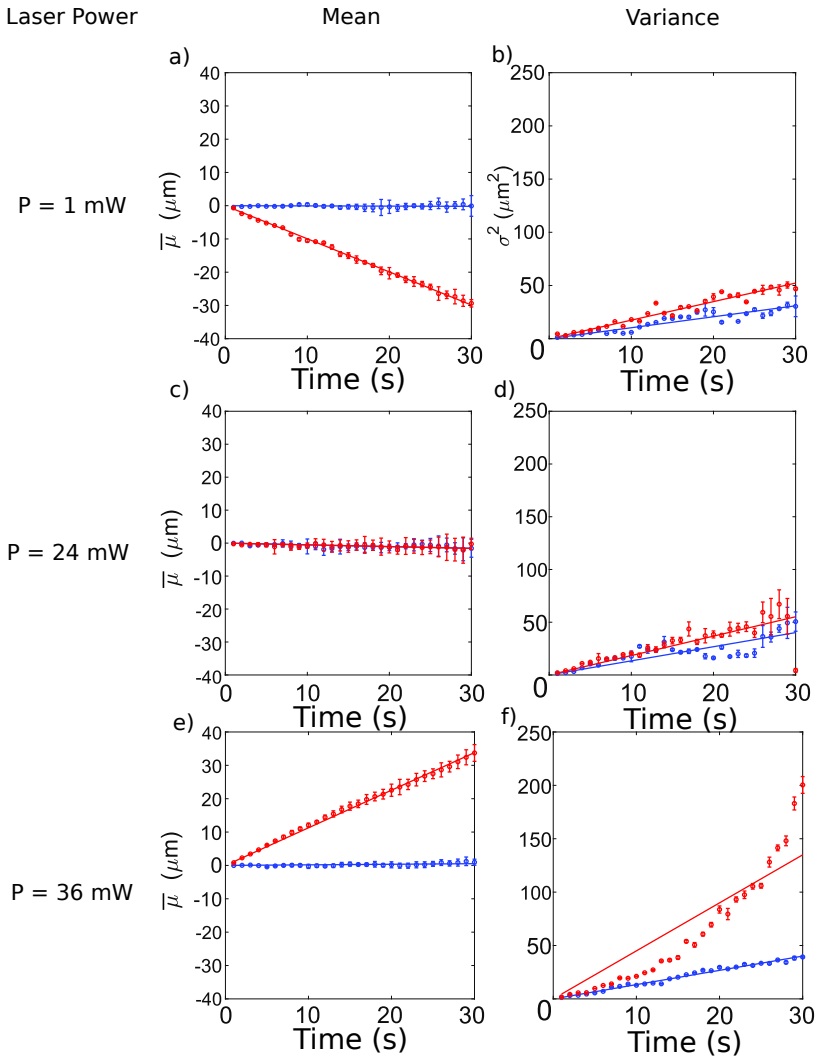

Figure 4.7 – Evolution of the mean and the variance of the PDF of position with respect to time. The blue and red curves represents Y and Z respectively. The solid line are the fitting of the data using a linear model. The errorbars represents the confidence intervals at 95% computed from fitting the PDFs

4.3.2 *PDF of displacements*

In this section, we now look at the PDF of displacements Δr defined over a chosen and fixed time difference Δt. We work with concatenated trajectories $\mathcal{T}_{P_i}$ and use the same sub-sampling strategy as in the previous section. We look at the statistical properties of $\mathcal{P}_{N_{sub}}(\Delta r, \Delta t)$ where N_{sub} is the number of sub samples.

Figure (4.8) displays, in the same three regimes, the means $\mu_{\Delta r}$ of all sub-sampled trajectories (numbered as individual trajectory Traj # in the figure). The estimator of the mean displacement for the sub trajectory i, $\mu_{N^i_{sub}}$ is :

$$\mu_{\Delta r N^i_{sub}} = \frac{\sum_{j=1}^{N^i_{sub}} r_j - r_{j-1}}{N^i_{sub} - 1} = \frac{\sum_{j=1}^{N^i_{sub}} \Delta r_j}{N^i_{sub} - 1} \tag{4.30}$$

where N^i_{sub} is the length, as a step number, of the sub- trajectory i. As discussed above the errorbars are the standard errors around the mean defined by :

$$SE(\mu_{\Delta r N^i_{sub}}) = \frac{\sigma_{\Delta r}}{\sqrt{N^i_{sub}}} \tag{4.31}$$

with $\sigma^2_{\Delta r} = \frac{\sum_{j=1}^{N^i_{sub}} \Delta r_j - \mu_{N^i_{sub}}}{N^i_{sub}}$ is the variance of the distribution, and $\sigma_{\mu_{\Delta r}}$ is the standard deviation. The distribution of the mean displacement is presented in figure (4.9).

As clearly seen, the mean of the displacement distribution of the sub sampled distribution is constant over time. The width of the distribution of the estimators i.e. standard deviation of the estimated mean, are within the standard error fixed by thermal fluctuations $\sqrt{\frac{2k_B T \Delta t}{\gamma N^i_{sub}}}$.

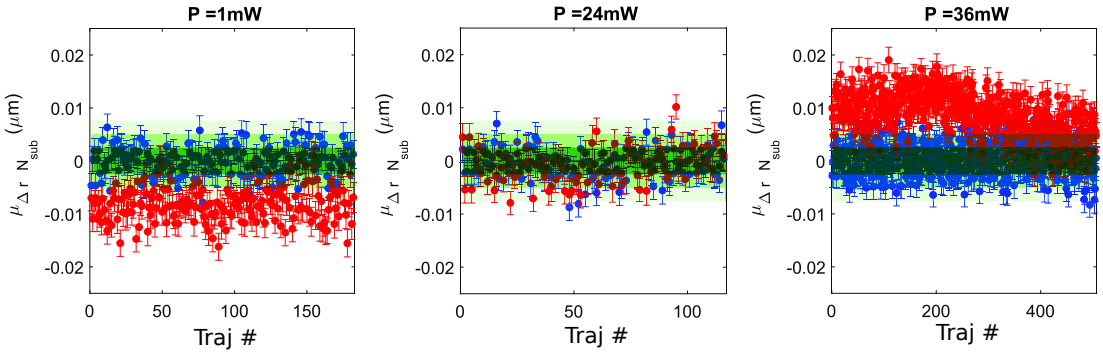

Figure 4.8 – Estimators of the mean displacement of the sampled trajectories. The blue and red bullets represents respectively the Y and Z directions. The green shadowed region represents standard error from mean theoretical displacement due to thermal fluctuations : from the darker to the lighter green 1σ, 2σ, and 3σ confidence levels.

In addition, the variances of the displacement distribution of the sub samples are presented in figure (4.10). The variances are more dispersed than the means presented in figure (4.8), but their distributions still remain narrow, as shown in figure (4.11).

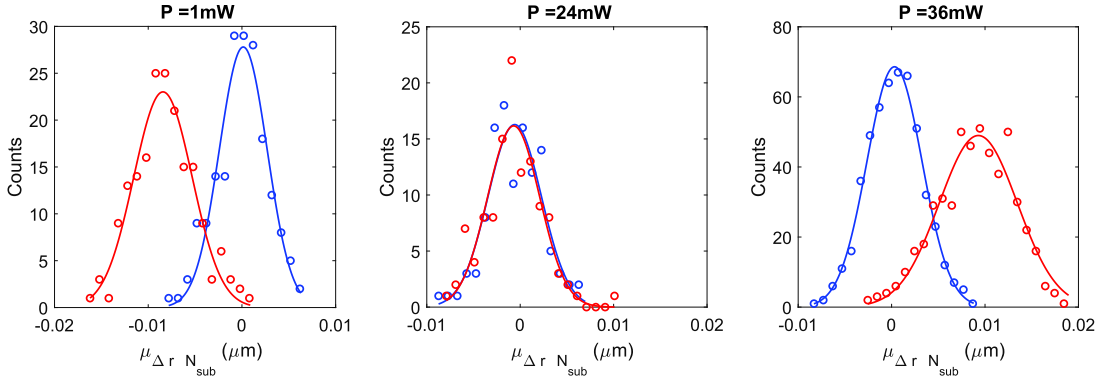

Figure 4.9 – PDF of the mean displacement of the sub sampled trajectories. The continuous lines represents a normal fit to the distribution of the mean of the estimator of the mean displacement for each sub-trajectory. The distributions are clearly sharp around the mean displacement. The counts are the number of estimated means that falls within the bin width defined in chapter I.

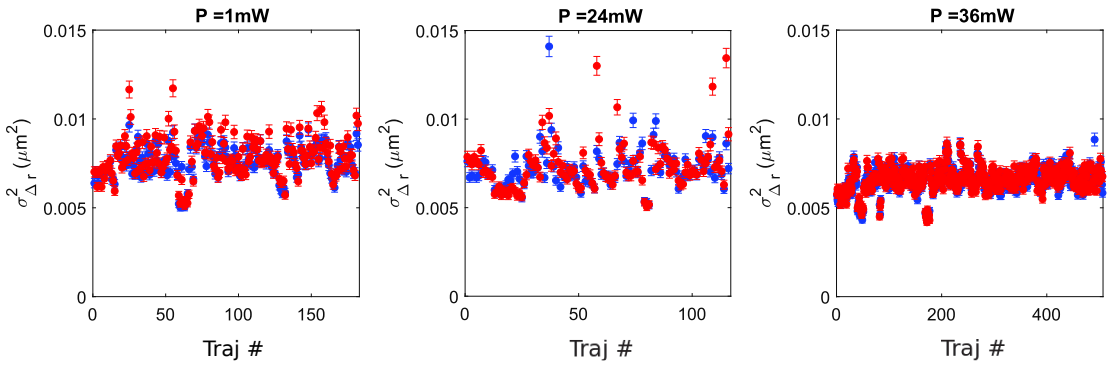

Figure 4.10 – Estimators of the variance of the displacement distribution defined in equation (4.31) of the sub sampled trajectories. The blue and red bullets represent respectively the Y and Z directions.

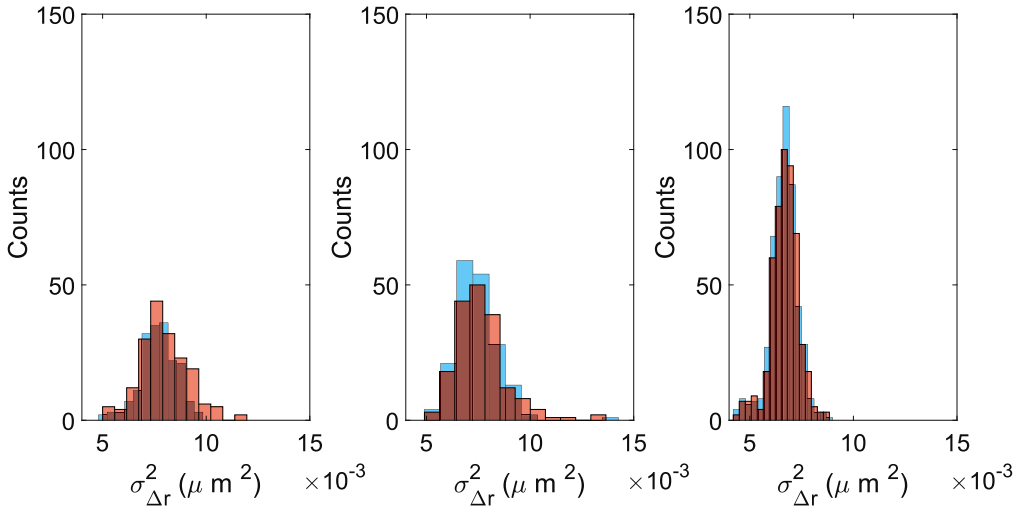

Figure 4.11 – Estimators of the variance of the displacement distribution of the sub sampled trajectories. The blue and red histograms represents respectively the along Y and Z axes. The number of bins depend on the sample size and is determined following Rice rule presented in the methods chapter.

4.3.3 *Autocorrelation function*

As another condition for the stationarity of a process, the autocorrelation function (ACF) measures the correlation between the stochastic time series Δr_t and Δr_{t+k} where k stands for time lag $\tau_k = k\Delta t$, with $k = \{0, 1, ..., K\}$, K being the number of intervals over which we calculate the ACF. For a Brownian particle the ACF decays to 0 with respect to time lag, demonstrating the independence of the displacements. The autocorrelation function for an ensemble of detected displacements $\{\Delta r_t\}$ is:

$$C(\tau_k) = < \Delta r(t + \tau_k) - \mu_{\Delta r} >< \Delta r(t) - \mu_{\Delta r} > \tag{4.32}$$

with the discrete version :

$$C_k = \frac{1}{T} \sum_{i=1}^{T-k} (\Delta r_i - \mu_{\Delta r})(\Delta r_{i+k} - \mu_{\Delta r}), \tag{4.33}$$

with T the number of displacements contained in the ensemble of displacements $\{\Delta r_{i+k}\}$. The ACF of an ensemble of detected displacements is shown in figure (4.12).

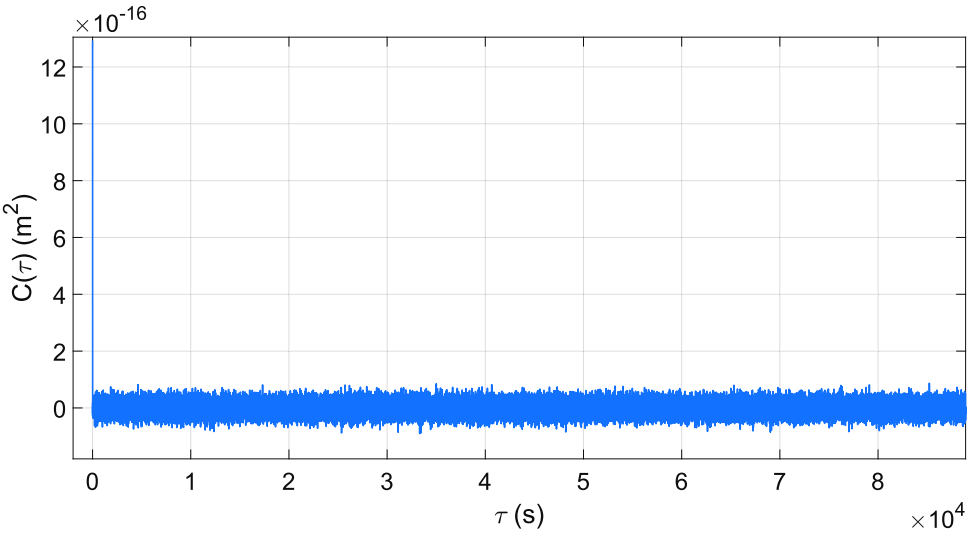

Figure 4.12 – Estimators of the covariance of the tracked displacements. The clear fast decay demonstrate that the displacements are non correlated. This is expected for Brownian motion.

The results taken together clearly correspond to the stationary condition (4.29) as verified on the statistical properties o the system. Having verified that the mean value and the variance of the stochastic Brownian process do not change over time and having verified a covariance equal to 0 constitute what is known as "strict stationarity". This stationary behaviour is confirmed in the three regimes of sedimentation, suspension and convection. This confirmation is central to the results presented below where a quantitative measurement of the external optical force field is performed from the analysis of the displacement based PDF of the assembly.

4.3.4 *Ergodic steady state*

The ergodic hypothesis is one fundamental hypothesis in statistical physics. A stochastic process is called ergodic if time average and ensemble average converge to be identical in the long time limit. In this section, we will compare the Ensemble Time Averaged MSD (ETAMSD) and the Ensemble Average MSD (EAMSD) defined, for an ensemble of N_T particles and time lags $\tau_j = j\Delta t$, as follows :

$$< \Delta x^2(\tau_j) >= \frac{1}{N_T} \sum_{i=1}^{N_T} (x_i(\tau_j) - x_i(0))^2 \tag{4.34}$$

where $x_i(t)$ is the measured time series for $i = \{1, 2, ..., N_T\}$. The procedure to compute the EAMSD is presented in figure (4.13). Firstly, we compute

all the squared differences $(x_i(\tau_j)-x_i(0))^2$ for the i^{th} particle. Secondly, we do the same for all the N_T trajectories. Finally, we calculate the arithmetic mean over the ensemble of trajectories.

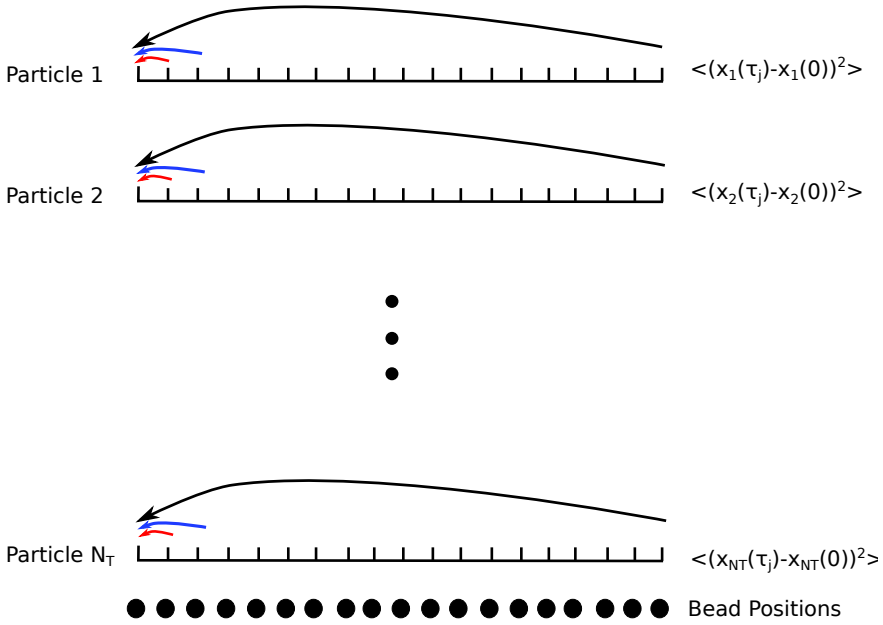

Figure 4.13 – Procedure to calculate the EAMSD.

We start by computing the ratio between the ETAMSD and the EAMSD :

$$\epsilon B = \frac{<\overline{\delta x^2(\tau)}>}{<\Delta x^2(\tau)>}. \tag{4.35}$$

We show in figure (4.14) in green the results for ϵB parameter in the three regimes. As naively expected, a $\epsilon B = 1$ value should correspond to the signature of ergodicity. But the concept of weak ergodicity breaking has stimulated many theoretical analysis [5] which have concluded, in particular, that ϵB can only be considered as a necessary condition for ergodicity, and, when testing the ergodic character of a stochastic process, it should be supplemented by an additional, sufficient, condition, built from the variance of the dimensionless parameter [5] :

$$\xi = \frac{\overline{\delta x^2(\tau)}}{<\overline{\delta x^2(\tau)}>}, \tag{4.36}$$

which quantifies the ratio between the TAMSD of a single trajectory $\overline{\delta x^2(\tau)}$ and the ETAMSD $<\overline{\delta x^2(\tau)}>$ for the ensemble of particles . The parameter ξ is related to the so called "ergodicity breaking" parameter EB, through its variance:

$$EB(\tau) = <\xi^2> - <\xi>^2 \tag{4.37}$$

where $< \xi >^2 = 1$ by definition of ξ.

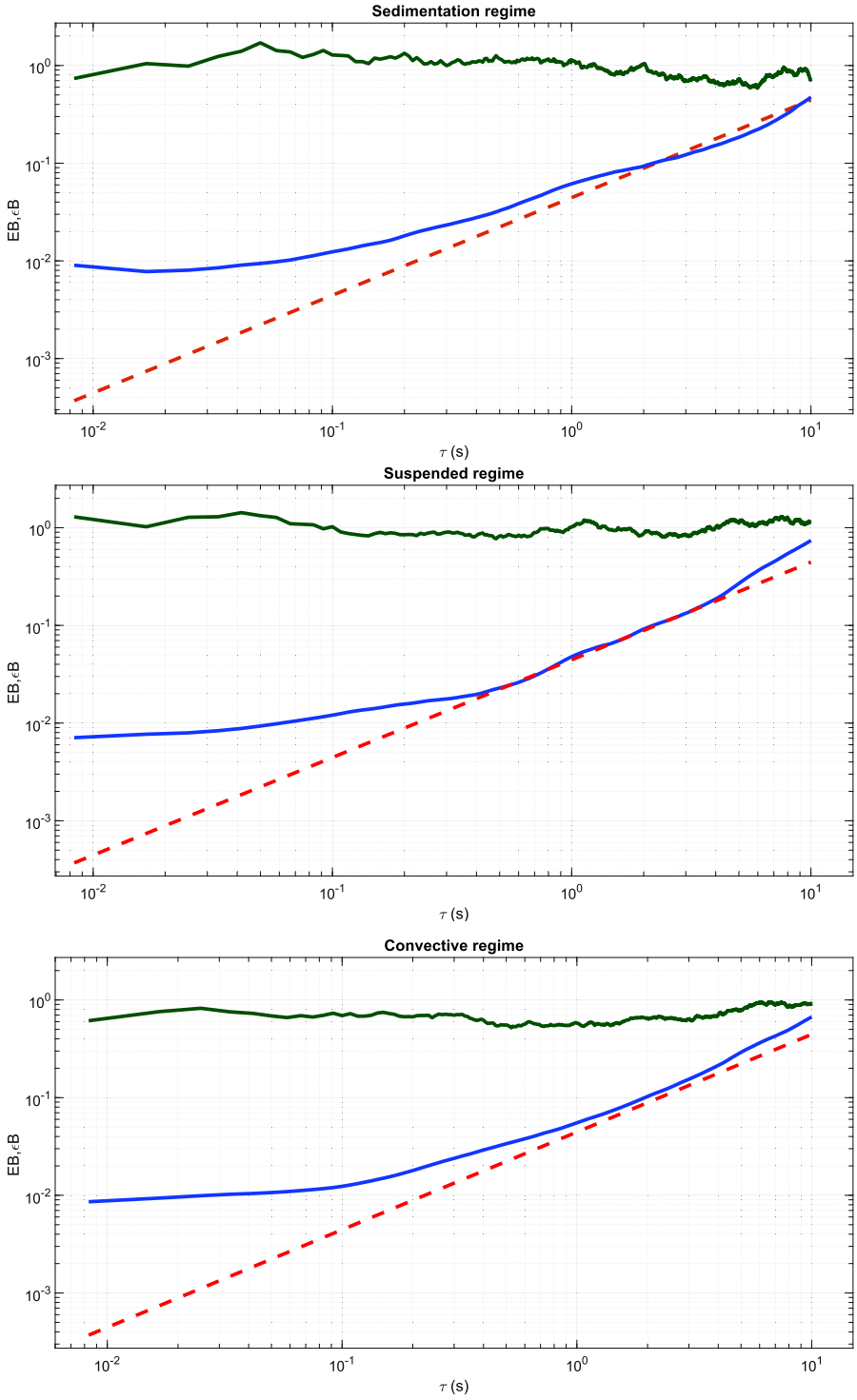

Figure 4.14 – Ergodicity breaking parameters in the three regimes. The red dashed line represents the free Brownian motion limit. The blue line is EB and the green line is εB.

For free Brownian motion, which is an ergodic process, the ergodicity breaking parameter $EB_{BM}(\tau)$ scales in the long time limit as [4] :

$$EB_{BM}(\tau) = \frac{4\tau}{3T}, \tag{4.38}$$

where T is the time duration of the trajectory. It is important to stress that this behaviour of EB is a sufficient condition for ergodicity.

The weak ergodicity breaking parameters are consistent with what is expected for free Brownian motion, validating the ergodic hypothesis for our system.

Together with the stationarity check, this analysis on ergodicity confirms, a posteriori, our initial assumptions and "concatenation" strategy, that we can use without loosing any information on the whole system.

4.4 STATISTICAL RESOLUTION

We now show how disposing of such long concatenated trajectories, we can actually measure the mean optical force exerted at the level of a single particle by the illumination laser itself, together with controlled uncertainties,

4.4.1 *Force estimator.*

We estimate the applied force on a single particle from the methodology discussed in section (2.1.3) that consists in computing the estimator of the external force following equation (4.23). We construct the displacements statistical ensemble by differentiating the successive positions Y_n and Z_n taken by the Brownian bead on the two main axis of the experiment presented in the last section.

Simulations are interesting to perform in this context. We start with the trajectory of Brownian particle under the gravity force field F_g :

$$F_g = mg = \rho V g = 4/3\pi\rho g R^3, \tag{4.39}$$

defined along the Z axis. The corresponding discretized Langevin equation then write as:

$$z_{n+1} = z_n + \frac{F_g}{\gamma}\Delta t + \sqrt{2D\Delta t}\, randn. \tag{4.40}$$

where randn is a random number generator of variables following the reduced centred normal distribution $\mathcal{N}(0,1)$. We show in figure (4.15) an example of such a simulated trajectory and the corresponding displacement distribution. The applied force is then extracted from the shift of the mean of displacements from zero. In that case, the measured force is : $F_g^{sim} = 9.3 \pm 2.9 fN$ to be compared to the expected force $F_g^{th} = 6.57 fN$ from equation (4.39). The two values are within the errorbars, but the relative errors are high in the order of 31%. Therefore defined for a random variable X as :

$$RE(X) = \frac{SE(X)}{\mu_X},$$

where SE(X) is the standard error around the mean, and μ_X is the estimator of the mean value of X.

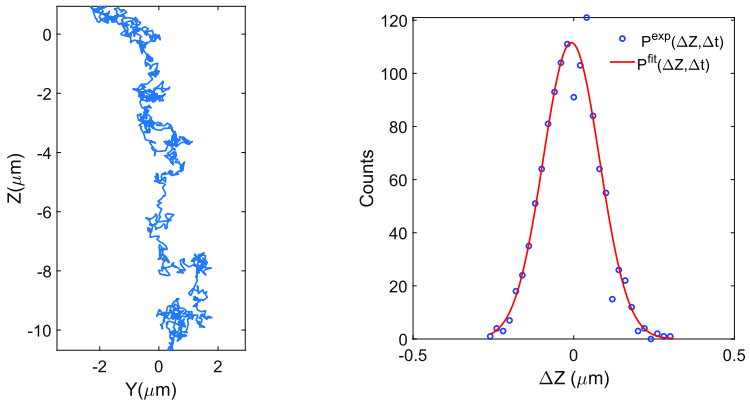

Figure 4.15 – Simulated Brownian trajectory under gravity force field. The displacement distribution is presented on the right panel. The length of the trajectory is $N_i = 1200$.

We now increase the length of the trajectory ten times and present the results in figure (4.16). In this case the measured force is :

$$< F_g >_{sim} = 6.15 \pm 0.91 fN.$$

The two values are still within the errorbars, but the relative error in this case has dropped to 14 %. Furthermore, the displacement distribution fits even better the Gaussian distribution.

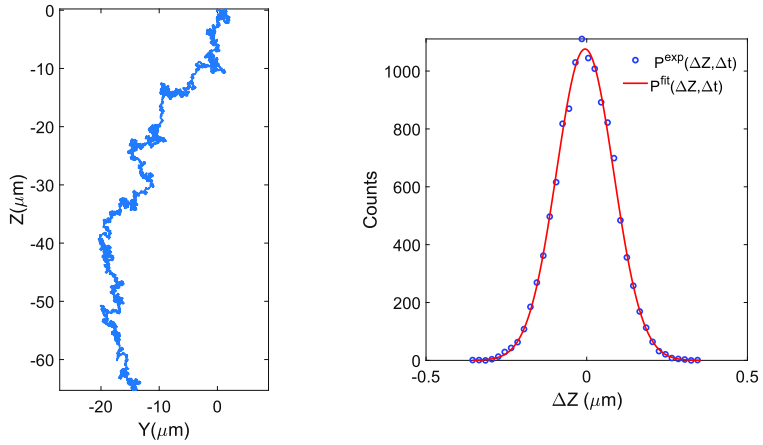

Figure 4.16 – Simulated Brownian trajectory under gravity force field. The displacement distribution is presented in the right panel. The length of the trajectory is $N_i = 12000$.

These tests clearly reveal the obvious relationship between the sample size and the measurement uncertainties. We will see in details the importance of the sample size for reducing the uncertainties from the experimental point of view, as discussed in section (4.2.4) above.

4.4.2 *Simulation results*

In this section, we resort to Langevin simulations in order to find a theoretical estimate of the uncertainties around the mean thermal force. The thermal force is a stochastic variable defined as :

$$F^{thermal} = \sqrt{\frac{2k_B T\gamma}{\Delta t}} l_n, \tag{4.41}$$

where l_n, defined in equation (4.18), follows $\mathcal{N}(0,1)$ distribution. The SE around the mean force is defined from equation (4.41) as :

$$SE(F^{thermal}) = \sqrt{\frac{2k_B T\gamma}{\Delta t}} SE(l_n), \tag{4.42}$$

where, from the definition of SE, one has :

$$SE(l_n) = \frac{\sigma}{\sqrt{N_t}}, \tag{4.43}$$

where $\sigma = 1$ because l_n is normally distributed with a variance equal to one, and where N_t is the total number of detected positions of the concatenated trajectory.

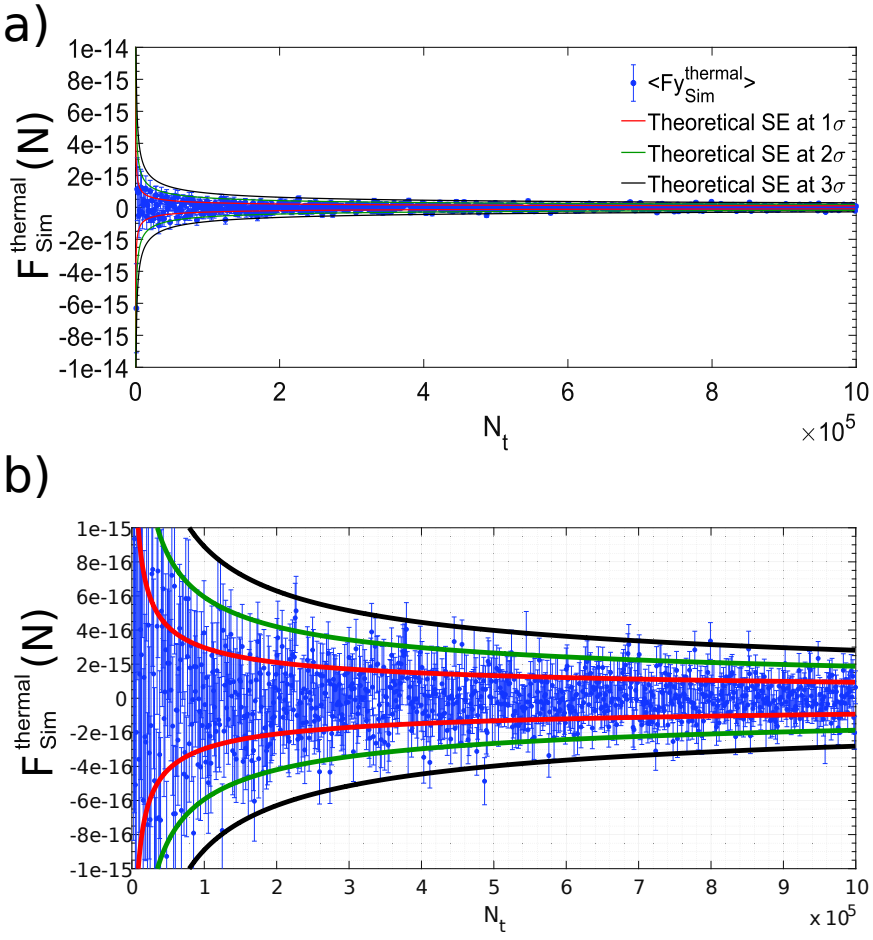

Figure 4.17 – Mean thermal force $F_{Sim}^{thermal}$ extracted from simulated trajectories as the sample size N_t (total number of simulated displacements) increases. The errorbars are the standard errors defined (4.42). Panel (b) is a zoom of panel (a) in the small sample limit.

Then the resolution level on force measurement is :

$$SE(F^{thermal}) = \sqrt{\frac{2k_B T\gamma}{\Delta t}} \frac{\sigma}{\sqrt{N_t}}, \tag{4.44}$$

which is inversely proportional to the square root of the total number of displacements N_t. As discussed in section (4.2.4) equation (4.44) clearly show that, the concatenation strategy, under validated assumptions, is good strategy to reduce the resolution we can reach on force measurement.

4.5 GLOBAL NOISE AND STABILITY

The discussion above relies on the fundamental role played by thermal fluctuations in our system. The "white" fluctuating spectrum of the Langevin force, fixed by the fluctuation-dissipation theorem, determines

the magnitude of the Langevin force $\sqrt{2k_BT\gamma}$, a value central to the whole analysis on force resolution.

It is thus critical : (i) to verify that the noise in our system is determined, essentially, by a white type of noise over a broad spectrum and (ii) to check the temporal limits of stability of our system under such white noise conditions since these limits will set a maximal size for our statistical ensemble of displacements which yields the corresponding SE, following equation (4.44). The appropriate tool to asses these two points simultaneously is the Allan deviation analysis used in a variety of contexts, ranging from atomic clocks, optical traps and optomechanics [63–66] .

The Allan variance AV $\sigma^2_{AV}(x)$ (the Allan deviation being $\sigma_{AV}(x)$) quantifies the type and stability of the noise involved in a random processes [67]. Figure(4.18) summerizes the type of AV expected for different kinds of noise. In our experiments, determined by a Gaussian white noise, we expect to measure an AV with a $-\frac{1}{2}$ slope (uncorrelated white noise).

Allan variance for a time series of N_t displacements is computed in the following way:

$$\begin{aligned}\sigma^2_{AV}(x) =& \frac{1}{2}<(x_{i+1}-x_i)^2>_\tau \\ =& \sum_{i=1}^{N_t}\left(\frac{x((i+1)\tau)-x(i\tau)}{\tau}\right)^2 - \frac{1}{2}\sum_{i=1}^{N_t}\left(\frac{x((i+1)\tau)-x(i\tau)}{\tau}\right)^2,\end{aligned} \tag{4.45}$$

where τ is the time interval, over which the particle moves by $x_{i+1}-x_i$, related to the sampling time $\tau = m\Delta t$, where m is an integer. Here the <...> corresponds to an arithmetic mean.

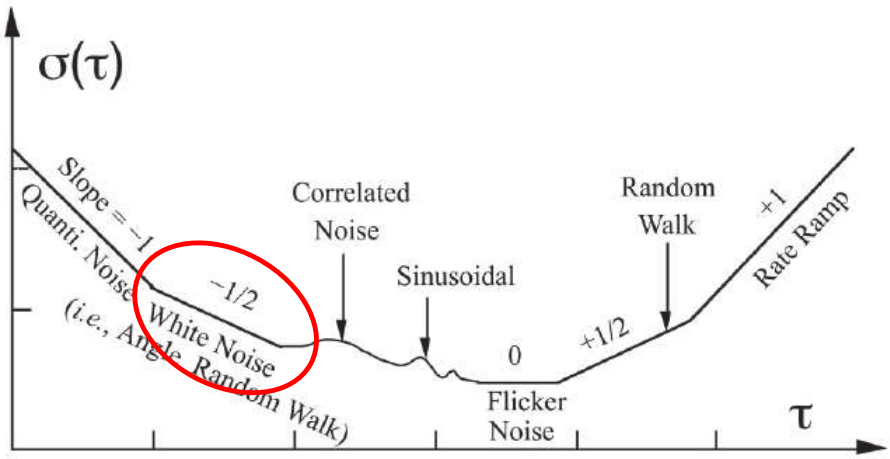

Figure 4.18 – Sample plot of AV analysis [68] for differents sources of noise. The slope of AV gives what type of noise and over which time window this noise determines the studied process.

For our experiments, we have computed the Allan variance for the ensemble of displacements measured along the Y-axis. The results, computed for 15 different experiments, are shown in figure (4.19). They clearly reveal :

- i) a -1/2 slop in log-log scale, corresponding to the signature of white noise,
- ii) and that this noise signature covers ca. 4 decades in time lag, enabling experiments to be tracked over ~ 300s within strict Brownian conditions

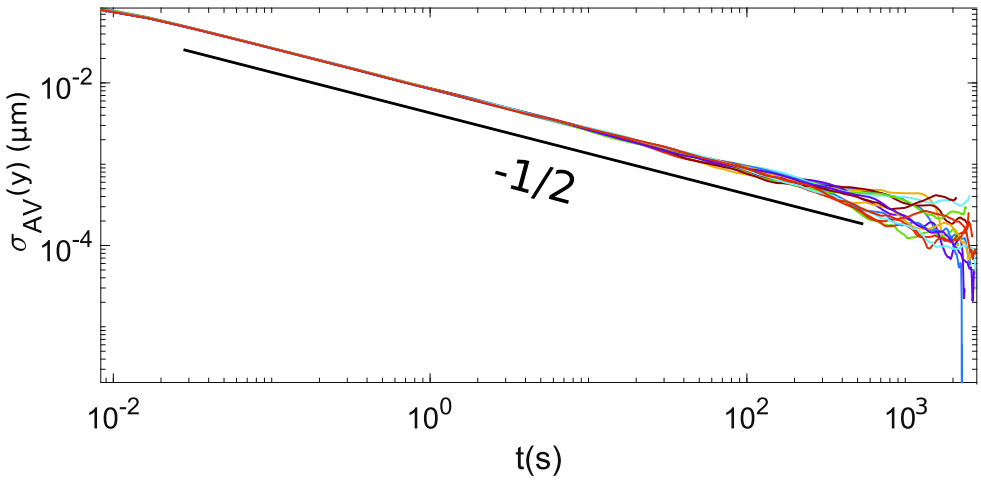

Figure 4.19 – Experimental Allan variance standard deviation σ_{AV} computed as a function of time lag τ. Each color corresponds to an experiment, where we compute AV for all the detected displacements. Each trajectory, concatenated, as been acquired in the contra-propagating beam configuration, at a given laser power. At long time lags, the noise comes from poor statistics, considering that the sample size decreases as time lag is increased. For such time lags, the AV is not so well defined any more.

This is a very important result that essentially confirms that our experiments, up to ~ 300s integration time, remain thermally limited with no drift in the thermodynamic noise. We also note that this white noise signature stemming from the Allan variance analysis is consistent with the covariance check done in section (4.3.3).

4.6 RADIATION PRESSURE FORCE MEASUREMENTS.

In this section, we give the results for radiation pressure force measurements using the setup presented in section (2.1), when all the power is injected in one arm. This option enables us to explore the dynamical range accessible in our experiment. We will then search for the lowest force that can be measured with our setup and compare it with the mean theoretical thermal force at play in the system.

4.6.1 *One beam configuration*

For this experiment, we inject all the power in one arm, with a beam diameter of 50 µm. In term of flux, the maximum input power is $0.4 kW/cm^2$ which a relatively low power. The measurement of radiation pressure force is shown in figure (4.20). These points have been acquired

following the methodology presented in section (4.6). As discussed in section (4.2.4), the errorbars are the standard errors defined in table (0.1).

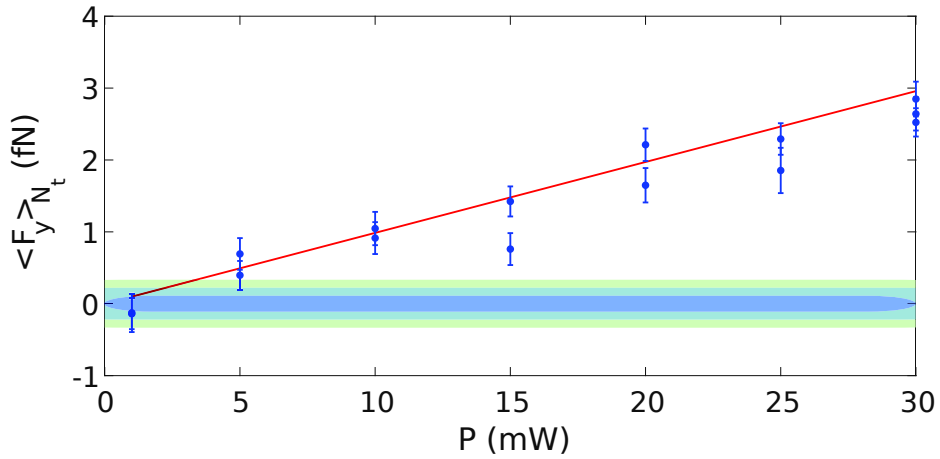

Figure 4.20 – Measured radiation pressure force $< F_y^{ext} >_{\{N_t\}}$ on Melamine beads along the optical axis for a displacement ensemble $\{\Delta Y\}_{N_t}$ at different laser powers. The errorbar represents the standard error around the estimator of the mean force along Y. The thermal limit is calculated from equation (4.44). The darker blue region is the standard error at the theoretical thermal limit with 1 σ, the lighter blue is 2 σ, and the green is 3 σ. The red line is the force value expected from a Mie calculation of the radiation pressure.

In red, we plot the theoretical value for radiation pressure applied on a single particle as evaluated using equation (4.2). The agreement between the measured and the calculated force is reasonable.

The question now is related to the minimal force that we can measure in our experiment. In order to answer this, we will focus on the limits of the thermal fluctuations, at the smallest level of power, where we reach the resolution limit of our setup. It is important to assess this resolution in order to provide a value for the minimum detectable force in our experiment.

4.6.2 *Resolution and sensitivity*

While the estimator of the mean displacement $\overline{\mu}_{\Delta y}$ due to the external force field, i.e radiation pressure, is given by the drift of the distribution of displacement from zero, it is clear that the minimum detectable force will be limited by the variance of the mean value of displacement. In other words:

$$< F_{ext} >_{min} = \frac{\gamma}{\Delta t} \overline{\sigma}_{\mu_{\Delta y}} \tag{4.46}$$

where $\sigma_{\overline{\mu}_{\Delta y}}$ can be estimated by the standard error of $\overline{\mu}_{\Delta y}$ built on the SD of the displacements ΔY. From section (4.2.2) this SD $\sigma_{\overline{\mu}_{\Delta y}}$ can be directly written from the Langevin equation in the absence of external force as:

$$\sigma_{\overline{\mu}_{\Delta y}} = \sqrt{\frac{2k_B T \Delta t}{\gamma}}.$$

corresponding to the thermal force discussed in section (**??**). The standard error is thus :

$$SE(\overline{\mu}_{\Delta y}) = \frac{\sigma_{\overline{\mu}_{\Delta y}}}{\sqrt{N_t}}$$

where N_t is the ensemble of detected displacements. For our thermally limited experiments, the thermal resolution is thus:

$$< F >_{min} = \sqrt{\frac{2kBT\gamma}{N_t \Delta t}}, \tag{4.47}$$

which can be evaluated in time-frame interval fixed in our experiments to $\Delta t = 1/120s$, to :

$$< F >_{min} = 93.5 fN/\sqrt{N_t}, \tag{4.48}$$

We display in figure (4.21) the measured values for radiation pressure for various power difference ΔP injected in each arm. These values are given with an ensemble of displacements $N_t = 5 \times 10^5$. The thermal limit is also drawn on the figure, setting 1σ, 2σ and 3σ confidence levels.

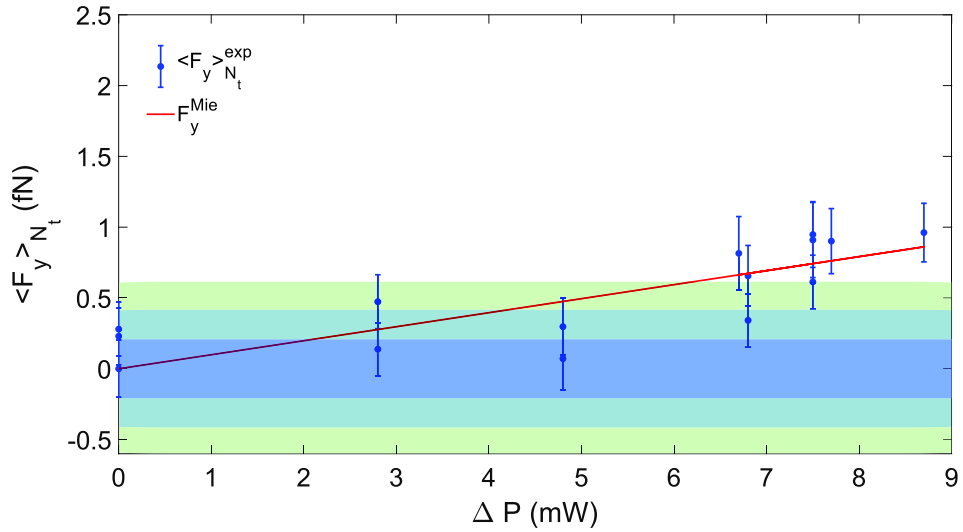

Figure 4.21 – Mean radiation pressure force on Melamine beads along the optical axis. The errorbars represent the standard error around the mean measured force along Y. The thermal limit is calculated from equation (4.44) and displayed as 1σ, 2σ and 3σ confidence levels.

Remarkably we are able to reach a high level of resolution in radiation pressure measurement. We can indeed unambiguously measure sub-femto newton forces at the thermal limit. Our experiment resolution is set to $< F_{ext} >_{min} = 0.2fN$ using $N_t = 5.10^5$ displacements, and working at 2σ confidence level.

4.6.3 *Force field profile reconstruction*

With such a high level of resolution, it becomes possible to envision reconstructing complex external force fields. As a proof-of-principle, we show that the Gaussian profile of the radiation pressure force field inherited by the laser beam can be reconstructed with good fidelity.

A CCD image of the laser beam is shown in figure (4.22), together with a cross cut fit of the image that both show the Gaussian nature of the beam and give an estimation of the beam diameter $2a \sim 100\mu m$.

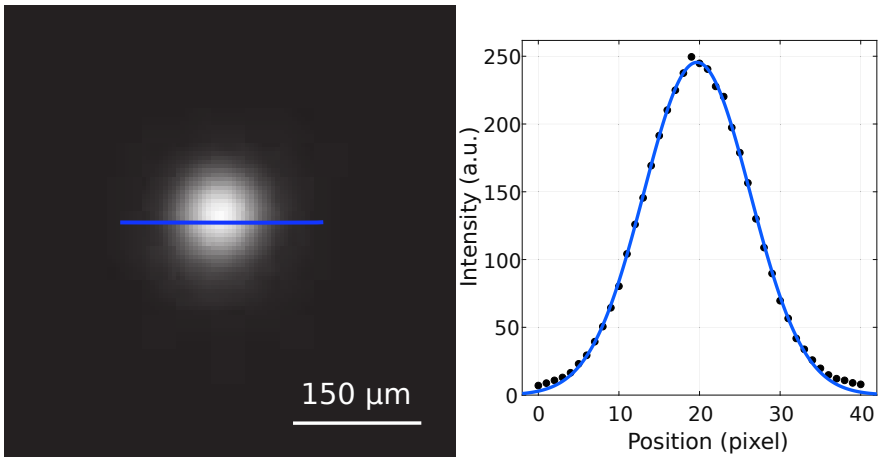

Figure 4.22 – Direct image of the beam at the level of the sample. The pixel size of the camera we used is 5.6µm. We see clearly the Gaussian profile. The blue continuous line is a Gaussian fit using the Gaussian model.

Taking into account this Gaussian profile into the force field applied along Y-axis, the Z dependence of the force field can be written as :

$$< F_y(z) >= F_{max} \exp\left(-\frac{z^2}{a^2}\right) = \frac{\gamma}{\Delta t} < \overline{\mu}_{\Delta y} > \tag{4.49}$$

wherz the estimator $\overline{\mu}_{\Delta y}$ is calculated over all the detected displacement during the experiment.

In order to find the Gaussian parameters corresponding to the force field profile, we define the function $f(a,b,c)$:

$$f(A) = \left(< A \exp\left(-\frac{2Z_n^2}{w_0^2} \right) > - \frac{\gamma}{\Delta t} < \overline{\mu}_{\Delta y} > \right)^2, \tag{4.50}$$

where A is the maximal strength of the force applied on the particles in the center of the beam. This value is reached when the defined function $f(A)$ reaches a minimum. The statistical samples used to perform the minimisation are : i) the ensemble of displacements $\{\Delta y_n\}$ along the horizontal Y-axis and ii) the corresponding positions ensemble $\{z_n\}$ along the vertical Z-axis.

In figure (4.23), we present the results obtained for the force profile. The shaded blue regions represents the theoretical thermal standard error (see equation (4.21)) with 1σ, 2σ and 3σ confidence levels. At low laser power, the distributions fall under the thermal noise level. But as we increase the power the amplitude which represents F_{max} scales linearly with the injected power. From 10 mW the measured values of the force and their uncertainties clearly emerge from thermal noise floor, and yield the Gaussian profile of the force field.

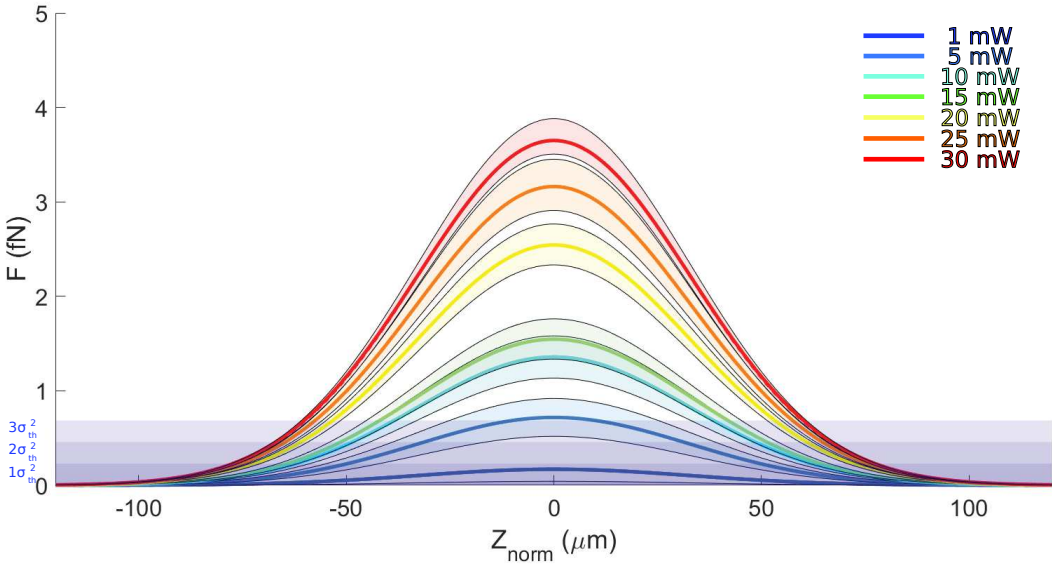

Figure 4.23 – Reconstruced force profiles for different laser power. The shaded regions represents the confidence intervals at 95%. The uncertainties displayed around the reconstructed profile are the SE defined in equation (2.41).

Our experiments are sensitive enough to measure very weak forces at the thermal limit. Exploiting the ensemble of displacements of the

particles, we can reconstruct the profile of the applied external force field. As seen in figure (4.23), the reconstructed profiles are in good agreement with the measured optical profile of the laser beam generating the force.

4.7 CONCLUSION

In this chapter, the optical setup described in chapter 1 has been exploited for measuring optical weak forces. The Brownian motion under such an external force field was described and the important statistical measures have been introduced. The concatenation strategy used to increase the statistical sample size was presented and the underlying hypotheses were verified in the context of stationary ergodic stochastic process. Furthermore, the uncertainties of our measurements have been quantified from the statistical point of view. We also verified the noise stability during our experiment which turned out, as expected, to be a white noise, validating our strategy of concatenation. Finally, the quantitative measurement of external radiation force was presented and compared to the evaluated force applied on a spherical particle in the framework of Mie scattering. We also proposed a method to reconstruct force field profiles from the tracked Brownian trajectories.

Our experiments open the door for interesting perspectives, by playing on the one hand on the properties of the colloidal assembly by using for example non spherical particles and study the torque applied by the laser radiation on the asymetric particle. We also envision using chiral particles and measuring their interaction with chiral light. On the other hand, more exotic field distributions like for example Bessel modes, or even more complex field distributions, could be used in order to resolve specific light-matter momentum transfer dynamics.

5

OBSERVINGING ANOMALOUS BROWNIAN TRAJECTORIES WITHIN A COLLOIDAL ASSEMBLY

In his derivation of the diffusion equation, Einstein made three assumptions :

- The particles are independent and non interacting,
- the existence of a sufficiently small time scale, over which the particles displacements are statistically independent,
- typical displacements of a particle during this characteristic time scale are symmetrically distributed in positive and negative directions.

Under such assumptions, the diffusion of a particle is characterized by the mean squared displacement :

$$< (r(t) - r(0))^2 >= \delta r^2(t) = 2Dt, \tag{5.1}$$

that we discussed and characterized in the previous chapters.

But if the particle starts interacting with the environment, taken in the broadest sense, in which it is diffusing, the diffusing behaviour can be very different. In a non-uniform medium, for instance, the instantaneous drag felt by the moving particle can lead to a random time-dependent friction [69]. The interaction can also stem from the hindering of the motion of the particle due to the presence of obstacles in the medium. This is exactly the situation corresponding to various work in particular theoretical ones, that reported anomalous diffusion effects in biological environments, so called "crowded environments" [70]. In such situations, the MSD associated with the motion of the particle now scales as :

$$\delta r^2(t) \sim t^{\alpha} \quad \text{with } \alpha < 1. \tag{5.2}$$

Experimental observations of sub diffusive motion have been reported in cytoplasm of living cells [71, 72], micellar solutions [73], and

functionalized environment [74, 75] to name of few of them. Such algebric laws for the MSD have sparkled a huge interest, with new models and new results proposed that are challenging two fundamental aspects of free Brownian motion : the ergodic character of the diffusion [76] and the relation between the MSD and the Gaussian character of the probability distribution of displacements [6]. Non Gaussian distributions are observed in viscoelastic fluids where memory effects are no longer negligible [77].

Considering the complexity of the systems, most of them biological, on which anomalous diffusion is usually observed, the emergence of anomalous trajectories in our simple experiments came as a surprise. As explain below, it is the possibility given by our microscope to isolate, from the colloidal ensemble, specific trajectories that led us to identify a few which motional behaviours are "anomalous" in the statistical sense within the ensemble, i.e. as rare manifestations among otherwise normal diffusive dynamics.

We will show in this chapter that such anomalous trajectories come from localized and accidental particle-particle interactions. While the precise mechanism inducing such interaction has still to be described, the statistical tools presented in the previous chapters allow us to characterize such trajectories, in particular from their MSD point of view, their probability displacement functions and their ergodic character.

5.1 OBSERVING ANOMALOUS DIFFUSION

Experimental observations of anomalous diffusion has been largely reported in crowded biological systems. Indeed, Single Particle Tracking (SPT) and optical tweezers have given access to the trajectories of fluorescent tracers diffusing in such complex media [78]. The observable which is often used to characterize such trajectories is the Time Averaged MSD (TA- MSD) which gives information on the dynamics of the particles from its temporal evolution. Figure (5.1) displays the main types of evolution expected for different types of dynamics.

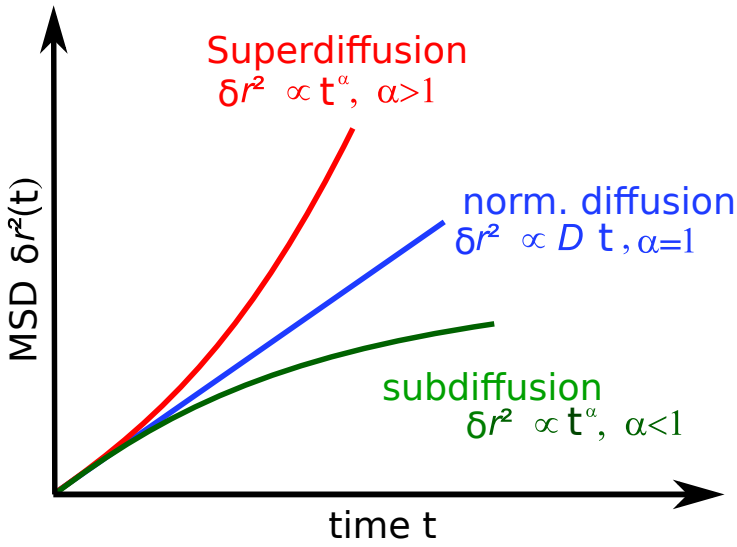

Figure 5.1 – Time Averaged MSD for different type of dynamics. For free diffusion the TA-MSD grows linearly with respect to the time lag τ. Sub-diffusive motion is characterized by a slower evolution of the TA-MSD. The super diffusive TA-MSD is representative of a ballistic motion due to an external flow transporting the particle, as discussed in chapters 3 and 4.

A simple and clear example of sub-diffusion can be found at the level of Brownian motion in visco-elastic media. Figure (5.2) displays an example of sub-diffusion of polystyrene beads in an artificial visco-elastic medium [73].

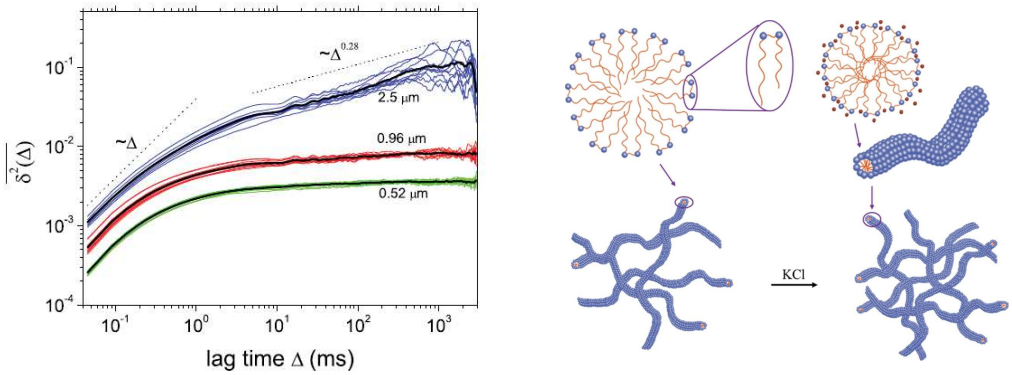

Figure 5.2 – Time Averaged MSDs for a mixture of micelles and polystyrene beads of different diameters $\{0.52\mu m, 0.96\mu m, 2.5\mu m\}$, where Δ is the time lag over wich the squared displacements are averaged. The black line represent the ETA-MSD defined by equation (3.10). The data are taken from [73]. The right hand side displays the micellar solution used in the experiment of [79] with added polystyrene beads.

For short time, the ETA-MSD is linear with respect to the time lag demonstrating a free diffusive motion. Then, for longer time lags, the evolution of the ETA-MSD is slowed down, with an exponent $\alpha = 0.28$ which is a clear evidence of sub-diffusive motion. The sub diffusive

behaviour for long time lags is understood as a manifestation of the hindered motion of the polystyrene beads by the micelles dispersed in the solution. This effect is not observed at short time lags because the particles motion at short time is not influenced by such obstacles.

This experiment demonstrates the cross over in the dynamics of particles diffusing in a crowded environment. This experiment also shows how a dynamical behaviour can be analysed be studying the behaviour of the MSDs at different time scales.

5.2 FROM ENSEMBLE TO SINGLE PARTICLE ANALYSIS

Our data analysis presented so far in the manuscript relies on looking at diffusing particles from an ensemble point of view. In this chapter, we are rather interested in looking at the dynamic of single particles. In this point of view, all the other particles become constituents of the medium itself. In other words, they can be seen as diffusing, neighbouring, dynamical obstacles for a specific targeted particle. Experimentally, the setup remains identical but we now reduce the microscope region of interest to one targeted particle which trajectory is recorded as a "single diffuser".

Figure (5.3) displays such an example where the free diffusive dynamics of a particle is eventually hindered by the presence of an other particle in its vicinity. Such neighbouring diffusing particles break down the Einstein's assumption of symmetric distribution of the positive and negative displacements.

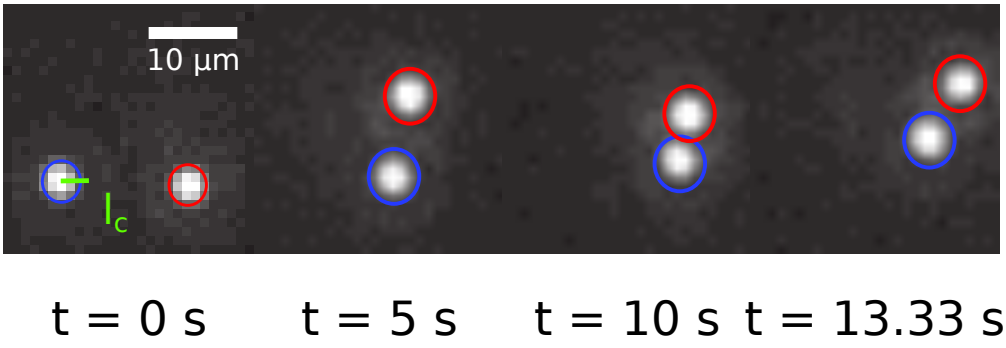

Figure 5.3 – Raw images of two interacting particles. At t=0, the two particles diffuse "normally" under the action of thermal fluctuations and the inter particle distance is d=15R, where R is the physical radius of a particle. From t=5s, the distance between the two particles is reduced to 10R. After that, beyond t=10s, the distance is reduced to d=5R and the particles starts repulsing each other due to the negative charge on their surface. Then from t=13.33 s the interparticle distance increases to d=13R. The characteristic length l_c is defined in equation (5.6).

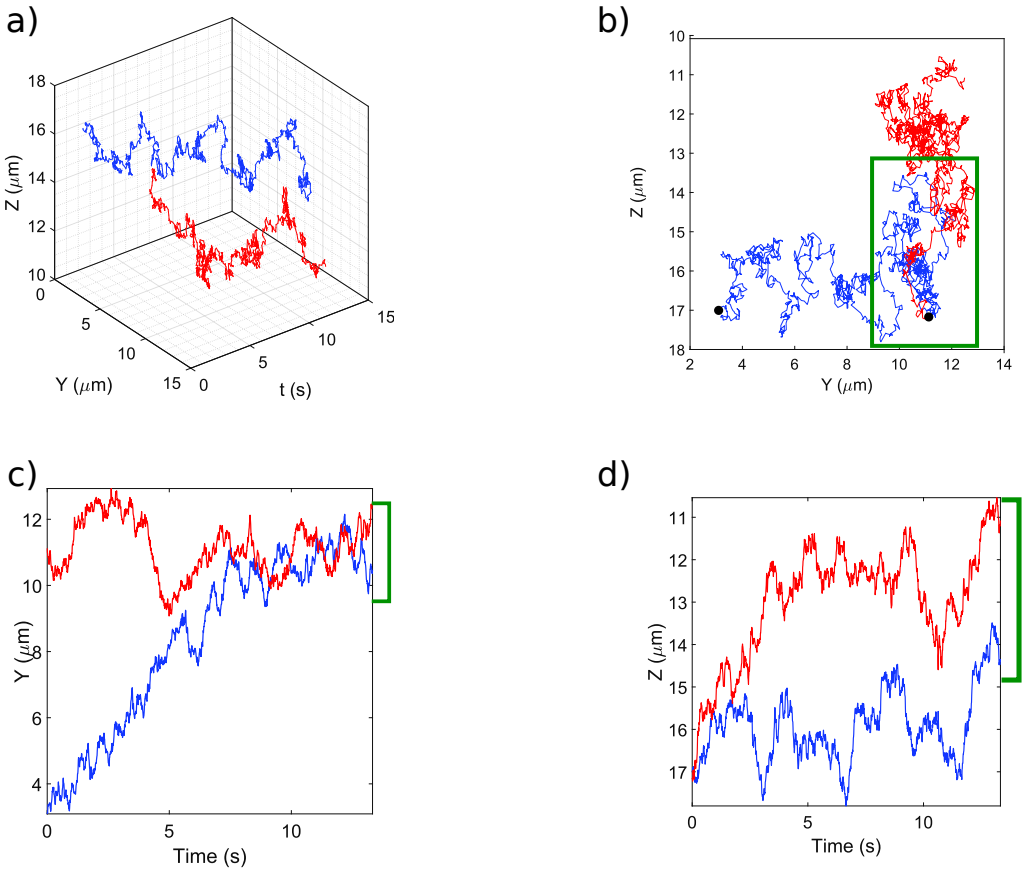

Figure 5.4 – Example of recorded trajectories of two interacting Melamine particles. Panel (a) displays the evolution of the 2D trajectories with respect to time. In panel (b) the 2D trajectories are presented. The panel (c) and (d) are the 1D projections of the interacting particles. The confinement is highlighted by the green rectangle and the corresponding regions are showed in panel c) and d).

This configuration is one of the few rare events that we have been able to notice in our experiments. The interaction occurs when the particles are in the vicinity of each others. This proximity is a random event, caused by thermal fluctuations. Such sub-diffusive behaviour has been observed in the three regimes presented in Chapter II. In figure (5.4) we display the trajectories of both interacting particles as seen along the Y and Z-axes of the experiment. It clearly appears on these data that while diffusing freely at the initial period of acquisition, the two particles accidentally get closer to each other. If charge stabilization prevent the particles to aggregate, we clearly observe a region where the two particles seem to interact with each other, as if one particle eventually hinders the motion of the other to freely diffuse. The actual origin of such "attraction" is an unsolved question for us. But its manifestation can clearly be revealed in our experiments, and

in particular through the time evolution of the motional MSD of a targeted particle.

5.3 ANOMALOUS MEAN SQUARED DISPLACEMENTS

One of the evidence for anomalous diffusion (and sub-diffusion in particular) is the algebraic evolution of TAMSDs following:

$$\delta r^2(\tau) = K_\alpha \tau^\alpha, \tag{5.3}$$

where K_α is the generalised diffusion coefficient [80], with the dimension $m^2.s^{-\alpha}$. The exponent α determines which type of diffusion the particle is undergoing. The logarithm of the measured TAMSD leads to extracting the local scaling exponent α as :

$$\alpha(\tau) = \frac{d(\log(\delta_r^2(\tau)))}{d(\log(\tau))}, \tag{5.4}$$

which represents the slope of $\log(\delta_r^2(\tau))$ with respect to $\log(\tau)$. Figure (5.5) displays the TAMSDs and ETAMSD of the particles undergoing sub-diffusion of the typical trajectories shown in (5.4).

The sub diffusive behaviour progressively emerges in the TAMSDs and the ETAMSD of the anomalous trajectories as a deviation from the linear TAMSD representative of a free diffusive motion. It is interesting to observe two different regimes that can be quantitatively analysed. Fitted at short and long time limits by :

$$\log(< \delta_y^2(\tau) >) = \alpha \log(\tau) + \log(K_\alpha), \tag{5.5}$$

the ETAMSD yields two exponents for each time limits. The results are presented in figure (5.5), revealing a free diffusive dynamics at short time ($\alpha = 1$) while non-ambiguously showing that the motion becomes sub-diffusive at longer time with $\alpha = 0.43$.

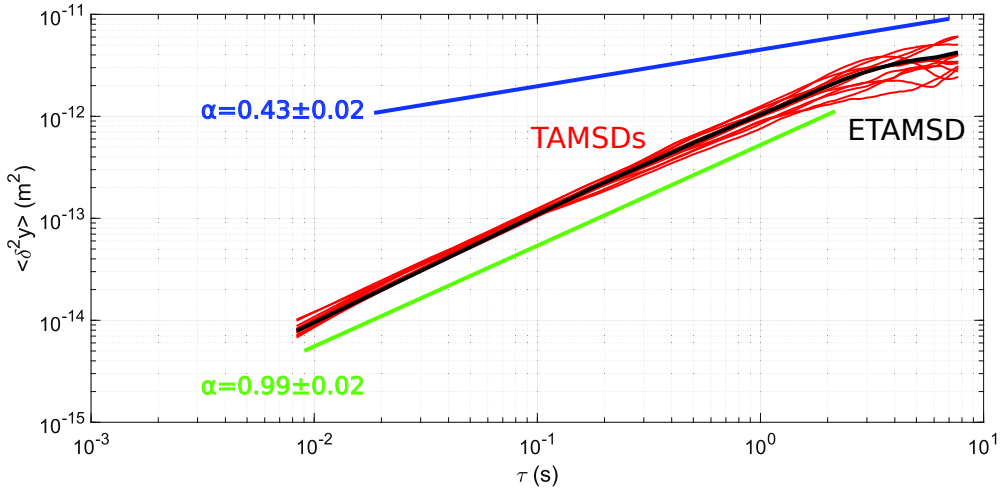

Figure 5.5 – The red curves are the TAMSDs $\delta^2_r(\tau)$ of 12 anomalous trajectories detected for an experiment recorded over 90 min. The black line is the ETAMSD $< \delta^2_r(\tau) >$ of the ensemble of anomalous trajectories. The blue line represents the exponent of the fitted ETAMSD which is $\alpha = 0.43 \pm 0.02$ for long time. The green line represents the fitted ETAMSD for short time : $\alpha = 0.99 \pm 0.02$.

The most interesting result here is the appearance of a well-defined transition between these two regimes. Indeed it seems that, we can defined a cut off time τ_c from which there is a transition from pure diffusion to anomalous diffusion. This characteristic time can be related to a characteristic length l_c through Einstein's relation as :

$$l_c = \sqrt{2D\tau_c} \tag{5.6}$$

where D is the diffusion coefficient.

In our experiments, we find $l_c = 1.73\mu m$. It is tempting to associate to this characteristic length l_c an interacting range as for instance given by a Yukawa-type interaction potential :

$$V_{int}(r) = A \exp^{-\frac{r}{l_c}}, \tag{5.7}$$

with A the strength of the interaction and r is the inter particle distance (see figure (5.3)).

5.4 DISPLACEMENT DISTRIBUTIONS AND ERGODICITY

The observation of anomalous diffusion obviously raises important questions about the precise mechanism at play behind such deviations from free Brownian motion. But the variety of situations where anomalous

diffusion is found challenges the possibility to provide an universal model. In fact, one finds in the litterature practically as many models as experimental situations, as discussed for instance in [5]. From a statistical point of view, the models aim at understanding some striking consequences of anomalous diffusion, in particular related to the Gaussian or non-Gaussian character of the motion [6, 81] or its ergodic or non-ergodic properties [5, 76].

As discussed in the previous chapter, from such Gaussian and ergodic perspectives, we have implemented the appropriate tools in our experiments to characterize the diffusive dynamics that we observe. We will first analyse the statistical nature of the motion by looking at the displacements distributions. The distributions are computed following the method presented in the previous chapters. Figure (5.6) displays the displacements distribution at different time lags $\mathcal{P}(\Delta Y, \tau_i = i\Delta t)$ where $\Delta Y = Y(\tau_{i+1}) - Y(\tau_i)$. In these experiments, $\Delta t = 1/120$s. At all times, the displacement distributions seem to follow Gaussian profiles. In this Gaussian framework, the distribution can be written as:

$$\mathcal{P}(\Delta y, \tau) \propto \frac{1}{\sqrt{4\pi D\tau^{\alpha}}} \exp\left(-\frac{\Delta y^2}{4D\tau^{\alpha}}\right). \tag{5.8}$$

keeping the time evolution of the distribution as general as possible through a power law variation for the variance. This variation is extracted from the Gaussian fits of all displacements distributions. The results are displayed in figure (5.6) from which we extract $\alpha = 0.92 \pm 0.03$. We see that this result is comparable to the results shown in figure (5.7) from the MSD at short time lags. For longer times, the distributions remain Gaussian and their associated variances evolve algebraically with time, as displayed in figure (5.8). The exponent extracted from a linear fitting of the variance evolution is equal to $\alpha = 0.24 \pm 0.1$, a value smaller than one that clearly reveals the anomalous character of the diffusion. As such, this result is comparable with the exponent extracted from the ensemble time averaged MSD, although of a smaller magnitude using the distribution approach.

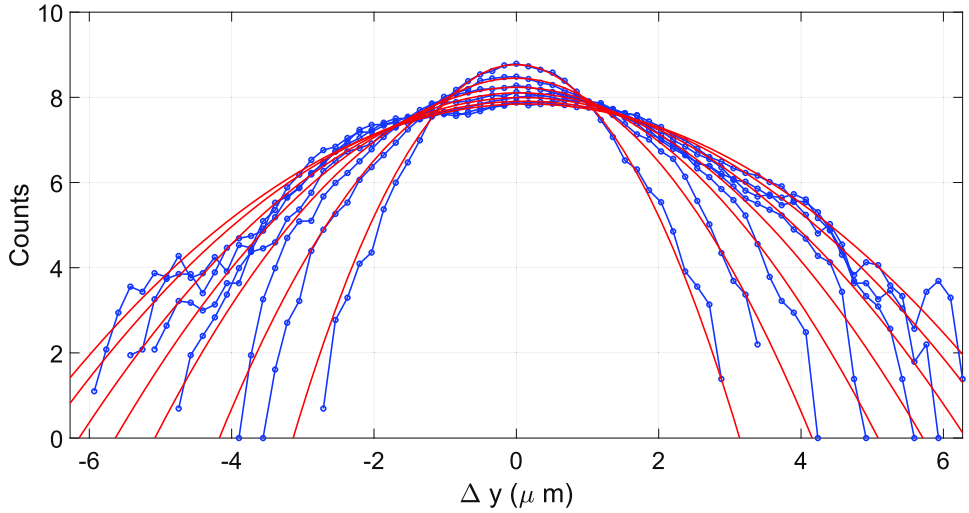

Figure 5.6 – Displacements distributions $\mathcal{P}(\Delta y, t)$ of the anomalous trajectories for different times $t = \{0.5s, 1s, 1.5s, 2s, 2.5s, 3s\}$. Remarkably the distributions remain Gaussian at all time. The counts are the number of times that the displacement of the particle lies within a given bin width of $0.17\mu m$.

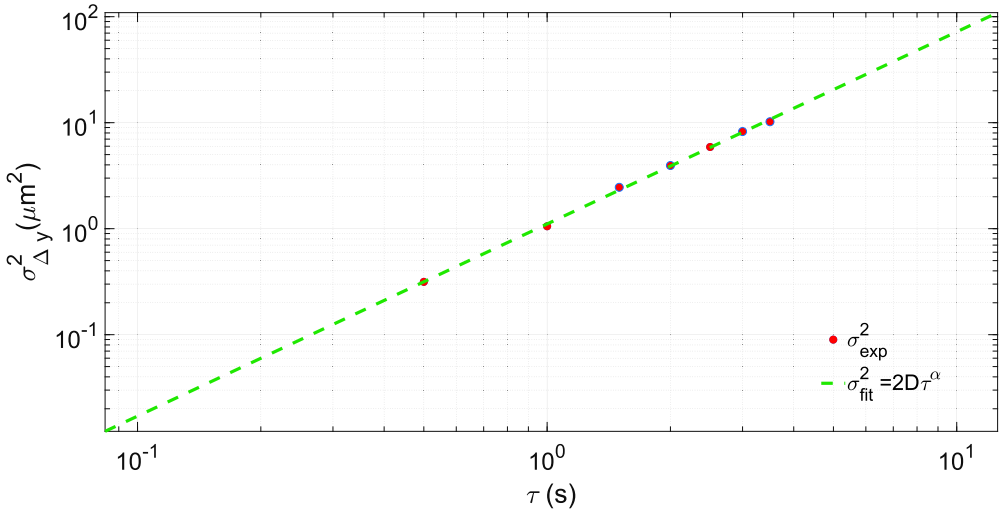

Figure 5.7 – Evolution of the variance of the displacements distributions with respect to time. By fitting $\log(\sigma^2)$ we extract $\alpha = 0.92 \pm 0.03$ defined in equation (5.8).

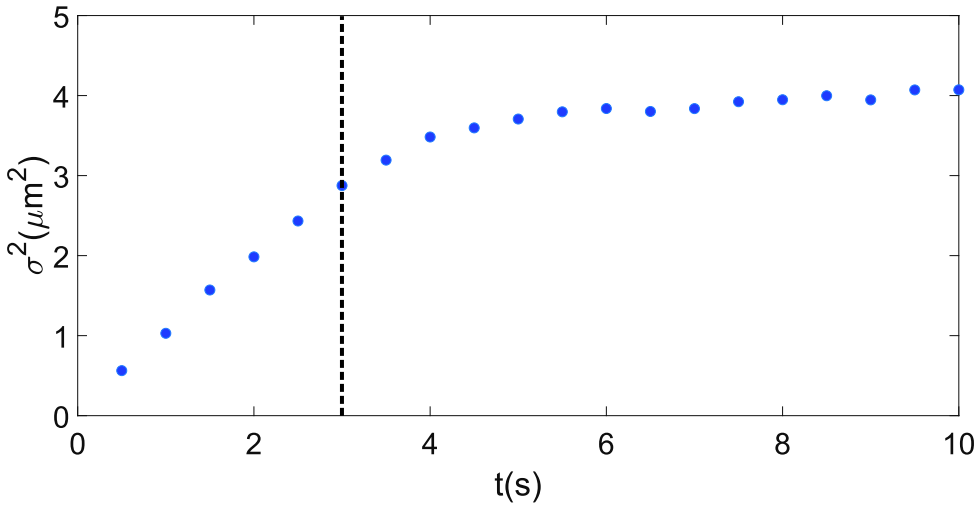

Figure 5.8 – Evolution of the variance of the displacements distributions. By fitting $\log(\sigma^2)$ at long time, we extract $\alpha = 0.24 \pm 0.1$ defined in equation (5.8).

We then study the ergodicity of the anomalous trajectories. We implement here the tools detailed in chapter three on the sample we built from the 12 anomalous trajectories that we recorded. Therefore we will evaluate the ergodic parameters, EB and ϵB. We recall the expression of the parameter ξ :

$$\xi = \frac{\delta r^2(\tau)}{< \delta r^2(\tau >}, \tag{5.9}$$

which quantifies, at the level of one individual particle, the ratio between the TAMSD and the ETAMSD.
The EB parameter is defined as follows:

$$EB(\tau) =< \xi^2 > -1, \tag{5.10}$$

which converge at long time to a finite value for free Brownian motion [5]

$$EB_{Brownianmotion}(\tau) = \frac{4\tau}{3T}, \tag{5.11}$$

where T is the total duration of the recorded trajectory. While this condition of convergence is a sufficient condition for ergodicity, a second necessary condition of ergodicity can be derived from the ratio between the ETAMSD and the Ensemble averaged MSD EAMSD defined in chapter three as :

$$\epsilon B = \frac{< \delta r^2(\tau) >}{< \Delta r^2(\tau >}. \tag{5.12}$$

We first show in figure (5.9) the TAMSDs, the ETAMSD and the EAMSD of the anomalous trajectories presented in the last section. We identify the

non linear behaviour in both the ETAMSD and the EAMSD that reveal the anomalous diffusion observed earlier at the level of the TAMSD evaluated on single trajectories.

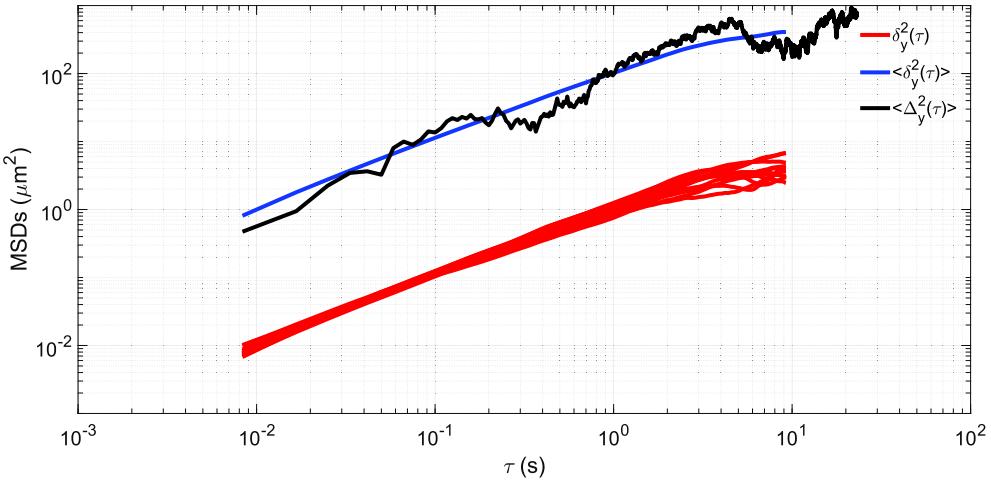

Figure 5.9 – Different MSDs for anomalous trajectories. The red curves are individual TAMSDs. The black curve is the EAMSD. The blue curve represents the ETAMSD.

We then present in figure (5.10) the corresponding ergodicity parameters. Our data, and despite their intrinsic fluctuations, seem to indicate that for long time limit, both of the parameters converge to one. This implies that although anomalous, our trajectories remain ergodic.

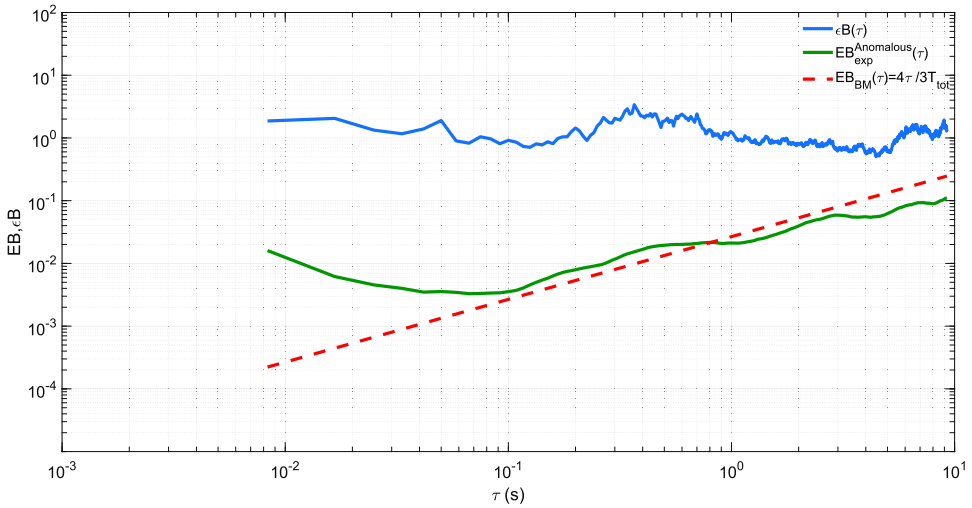

Figure 5.10 – ergodicity parameters computed for the 12 anomalous trajectories for which the MSDs are presented in figure (5.9). The blue curve is ϵB which is equal to one. The green line shows the parameter EB which progressively follow the EB expected for free Brownian motion, represented by the dashed red line.

5.5 CONCLUSION

Anomalous diffusion of passive particles is observed in a variety of systems and contexts ranging from physics to biology. Usually, the systems have a level of complexity that immediately put Einstein's assumption into questions : for instance, crowded environments, confined media, visco-elastic fluids, structured environments, bacterial media, biological matter.

The manifestation of anomalous diffusion in our experiments came as a surprise, considering the simplicity of our setup as a whole, made of simple dielectric particles, dispersed in a Newtonian fluid at low volume fraction. But out video microscopy technique allowed us to "focus" on very specific situations where the motion of a targeted particle is modified by the presence of one, or more, neighbouring particles. The results presented in this chapter have shown that the statistical properties of these trajectories, although anomalous, remain Gaussian and ergodic. This is an interesting piece of information when relating our experiments to existing models that could help us in describing the observed dynamics and understanding its microscopic source.

An obvious guess is to analyze our data in the framework of the continuous time random walk (CTRW) which is widely used for describing anomalous diffusion in complexe environments [82]. But such model implies non ergodic motions [83] which is not what we observe. This relation with ergodicity also seems to exclude another class of anomalous diffusion model know as "random diffusivity" models [4] . These models, among which belongs the model of scaled Brownian motion [84] are very attractive since they reflect anomalous MSD into a simple rescaling of the diffusion "constant" as :

$$\delta r^2(t) = (2K_\alpha t^{\alpha-1})t.$$

However, such models induce generally non-ergodic trajectories through the time dependence of the diffusion constant.

Our observations rather point towards the onset of an "effective" motion of the targeted particle induced by 2-body (and more) coupled interactions. The sudden change in the power law governing the recorded MSD for the anomalous trajectories that we monitored seem to indicate, as discussed above, the existence of an attraction volume beyond the exclusion volume created by charge repulsion. As a consequence, the thermal noise that drives the particle's diffusion, can show some correlations. Such

correlations constitute the basis of another class of models, so called Fractional Brownian models[5].

Remarkably, Fractional Brownian motion is characterized by Gaussian displacement distributions, while maintaining (at least asymptotically) full ergodicity.

Naturally, these two features turn out into assets for proposing a model able to describe our experiments in their apparent simplicity. This task however is beyond the scope of this work.

6

CONCLUSION AND PERSPECTIVES

Single Particle Tracking has been used to quantify the dynamics of colloidal suspensions subjected to external force fields. Such technique allows us to efficiently proceed to real-time tracking of Brownian particles with a temporal resolution of $\Delta t = 8ms$ and positional resolution of the order of 20 nm.

The non-equilibrium steady state character of our system is investigated through the study of the stationary and ergodic aspects of the recorded trajectories. Such aspects have been used in this work as tools for characterizing the motional effects that we have observed under laser light irradiation.

The injected laser power in our system has allowed us to manipulate our colloidal assemblies in different regimes, explored both from a statistical "ensemble" point of view and a more local one, looking at specifically targeted trajectories. A first part of the work has been devoted to look at collective motional manifestation of heat injected by the laser into the fluid that modified the local density of the fluid. The observation of two ballistic regimes for high and low laser power limits was presented, with the interesting intermediate regime where a practically freely diffusive regime was observed in 3D space.

Moving from such "ensemble" observations, we also reported on rare individual trajectories signatures of anomalous diffusion. Such report, on such a simple system as ours, came as a surprise. We identified the source of anomaly in the accidental modification of Brownian diffusion of a given particle due to the presence of an other particle in its vicinity. The statistical characterization of such anomalous motion (Gaussian and ergodic characters) remarkably seem to indicate that our experimental records do not match a priori the main model proposed for describing anomalous Brownian diffusion. This interestingly opens the door for more theoretical input.

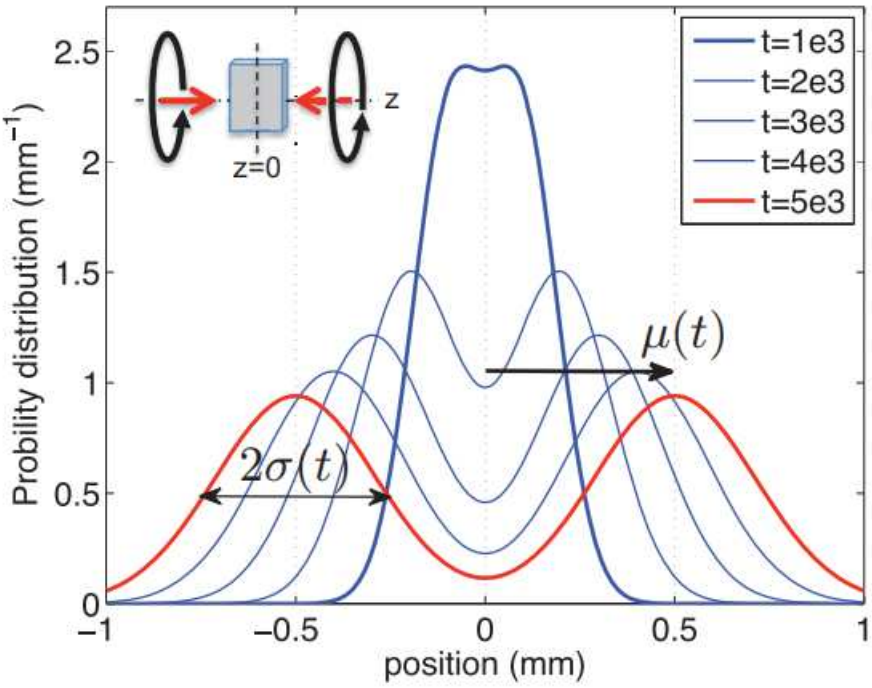

Figure 6.1 – Demonstration of chiral particles separation induced by dissipative chiral forces. A racemic mixtur illuminated by counter-propagating circularly polarized two-beam configuration, can be sorted. A separation of 1 mm is predicted for an experiment lasting one hour. This figure is from [16].

In addition to heat injection, the illumination laser can also work on our system by exerting radiation pressure on each colloidal particle that diffuses inside the optical beam. Under our experimental conditions, we demonstrated a capacity to measure weak radiation pressure forces at the thermal limit fixed by the temperature of the fluid. Exploiting the fact that we can access many trajectories and thereby form a large ensemble of displacements, we have been able to resolve such radiation pressure forces at the fN level and reconstruct the actual optical force field profiles responsible for biasing the Brownian motion of the colloidal assembly.

This level of resolution opens many opportunities in the context presented in the general Introduction of the manuscript, when aiming at reconstruct exotic optical force fields from Brownian trajectories. In the context of dynamical chiral light-chiral matter interactions, resolving with such a high-resolution level light-matter momentum transfers is particularly important. We could today envision using chiral colloidal assemblies illuminated by circularly polarized light, in order to reveal and measure at the nano-scale the optical chiral forces recently predicted in our group, and simultaneously also by a couple of other groups [17]. Such forces have only been revealed to date on experiments involving

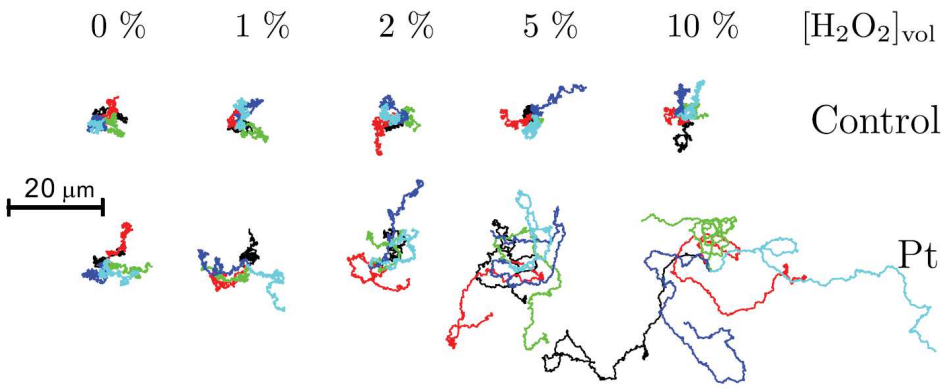

Figure 6.2 – Example of active Janus spherical particles (Platinum-Polystyrene) trajectories. The active motion is fuelled by asymmetric catalysis of hydrogen peroxide of platinum at the surface of the half coated particles. At short time scales the motion is directed and at long time scales the motion is randomized. As shown, for non coated particles the motion is freely diffusive. However, the motion of platinum coated particles is clearly directed. This figure is direcly taken from [87].

micron-scaled cholosteric spheres [85], with the argument that at such a large scale, the "racemizing" effect of Brownian motion could be much better controlled. Our setup using chiral colloids, as recently prepared [86], gives the possibility to implement at the nano-scale the all-optical chiral sorting scheme proposed theoretically in [16].

It is worth mentioning that the force resolution we have reached in the present work lies within the "realistic" bounds set in this theoretical proposal. Finally, we would like to stress that our setup is versatile enough to study active Brownian dynamics, as shown in figure (6.2). Active Brownian motion constitutes today an extremely active field of research. This tool is drawing interesting perspectives along which the general methods implemented in this work could be relevant.

Appendices

A

HEAT EQUATION SOLUTION

In this appendix the detailed calculation to solve equations (3.21). Starting from equation (3.21), we perform a first integration of :

$$\frac{\partial}{\partial r}\left(r\frac{\partial}{\partial r}\delta T\right) = -r\frac{AP_0}{\pi a^2\lambda}\exp\left(-\frac{r^2}{a^2}\right), \tag{A.1}$$

to obtain :

$$r\frac{\partial}{\partial r}\delta T = -\frac{AP_0}{\pi a^2\lambda}\int r.\exp\left(-\frac{r^2}{a^2}\right)dr,$$

$$r\frac{\partial}{\partial r}\delta T = -\frac{AP_0}{2\pi\lambda}\int \exp\left(-\frac{r^2}{a^2}\right)d\left(\frac{r^2}{a^2}\right) = \frac{AP_0}{2\pi\lambda}\exp\left(-\frac{r^2}{a^2}\right) + C.$$

The constant C is determined assuming the first boundary condition :

$$r\frac{\partial \delta T}{\partial r}\bigg|_{r=0} = 0 = C + \frac{AP_0}{2\pi\lambda}$$

$$C = -\frac{AP_0}{2\pi\lambda},$$

we get then :

$$\frac{\partial \delta T}{\partial r} = -\frac{AP_0}{2\pi\lambda}\left(\frac{1}{r} - \frac{\exp\left(-r^2/a^2\right)}{r}\right),$$

which we integrate to have the temperature difference :

$$\delta T = -\frac{AP_0}{2\pi\lambda}\left(\ln(r) - \int \frac{\exp(-\frac{r^2}{a^2})}{r\frac{r}{a^2}}\frac{r}{a^2}dr + C'\right),$$

and substitute $t = \frac{r^2}{a^2}$ in the integral to get :

$$\delta T = -\frac{AP_0}{2\pi\lambda}\left(\ln(r) - \frac{1}{2}\int \frac{\exp(-t)}{t}dt + C'\right). \tag{A.2}$$

We introduce the exponential integral function defined as :

$$E_1(x) = \int_x^\infty \frac{\exp(-u)}{u} du = \int_1^\infty \frac{\exp(-tx)}{t} dt. \tag{A.3}$$

Taking the first derivative :

$$\begin{aligned} \frac{dE_1(x)}{dx} &= \int_1^\infty \frac{d}{dx}\left(\frac{\exp(-tx)}{t}\right) dt \\ &= -\int_1^\infty \exp(-tx) dt \\ &= -\frac{1}{x}\int_1^\infty \exp(-tx) dtx \\ &= -\frac{\exp(-x)}{x}, \end{aligned} \tag{A.4}$$

we can identify the integral in equation (A.2) as :

$$\int \frac{\exp(-t)}{t} dt = -E_1(t) + C_1.$$

Equation (A.2) is rewritten then :

$$\delta T = -\frac{AP_0}{2\pi\lambda}\left(\ln(r) + \frac{1}{2}E_1\left(\frac{r^2}{a^2}\right) + C_1'\right), \tag{A.5}$$

then in order to get the constant C_1', we use the second boundary condition :

$$\delta T(\delta_T/2) = 0,$$

we obtain then :

$$C_1' = -\ln(\delta_T/2) - \frac{1}{2}E_1\left(\frac{\delta_T^2}{4a^2}\right),$$

and finally :

$$\delta T = \frac{A.P_0}{4.\pi.\lambda}\left(-2\ln\left(\frac{2.r}{\delta_T}\right) - \frac{1}{2}E_1\left(\frac{r^2}{a^2}\right) + \frac{1}{2}E_1\left(\frac{\delta_T^2}{4a^2}\right)\right).$$

B

NAVIER-STOKES EQUATION SOLUTION

In order to solve the system (3.28), we follow the same procedure by integrating twice each equation of the system. Let us first introduce some constants :

$$K = \frac{g\beta A P_0}{4\pi\lambda\nu},$$

$$K' = -2\ln\left(\frac{\delta_T}{2}\right) - E_1\left(\frac{\delta_T^2}{4a^2}\right).$$

Starting by the first equation of the system :

$$\frac{\partial^2 v_z^{(1)}}{\partial x^2} = K\left[2\ln(x) + E_1\left(\frac{x^2}{a^2}\right) + K'\right], \tag{B.1}$$

the integral is then :

$$\frac{\partial v_z^{(1)}}{\partial x} = K\left[2x\ln(x) - 2x + K'x + C_1 + \int E_1\left(\frac{x^2}{a^2}\right)dx\right].$$

The integral of $E_1\left(t^2\right)$ is calculated as follows :

$$\begin{aligned} E_1\left(\frac{x^2}{a^2}\right) = E_1(t^2) &= \int\int_1^\infty \frac{e^{-t^2u}}{u}du\,dt \\ &= tE_1(t^2) - \int t\left(\int_1^\infty \frac{e^{-t^2u}\cdot(-u)\cdot(2t)}{u}du\right)dt \\ &= tE_1(t^2) + 2\int t^2\left(\int_1^\infty e^{-t^2u}du\right)dt \\ &= tE_1(t^2) + 2\int e^{-t^2}dt \\ &= tE_1(t^2) + \sqrt{\pi}\,\mathrm{erf}(t) \end{aligned} \tag{B.2}$$

where the error function is defined by :

$$\mathrm{erf}(x) = \frac{2}{\sqrt{\pi}}\int_0^x e^{-u^2}du.$$

Equation (B.1) become then :

$$\frac{\partial v_z^{(1)}}{\partial x} = K\left[2x\ln(x) - 2x + K'x + C_1 + xE_1\left(\frac{x^2}{a^2}\right) + a\sqrt{\pi}\,\mathrm{erf}\left(\frac{x}{a}\right)\right],$$

here the constant is calculated from the boundary condition :

$$\left.\frac{\partial v_z^{(1)}}{\partial x}\right|_{x=0} = 0$$

then :

$$C_1 = 0$$

and the expression of the first integral is :

$$\frac{\partial v_z^{(1)}}{\partial x} = K\left[2x\ln(x) - 2x + K'x + xE_1\left(\frac{x^2}{a^2}\right) + a\sqrt{\pi}\,\mathrm{erf}\left(\frac{x}{a}\right)\right]. \qquad (B.3)$$

The solution of the second equation in the system (3.28) is simply :

$$v_z^{(2)} = \pm C'x + C''$$

the constants are determined using the continuity of v_z at the merger of the thermal and the velocity boundary layer, firstly for the derivative:

$$\left.\frac{\partial v_z^{(1)}}{\partial x}\right|_{x=\pm\delta_T/2} = \left.\frac{\partial v_z^{(2)}}{\partial x}\right|_{x=\pm\delta_T/2}$$

so we obtain :

$$C' = K\left[\delta_T\ln\left(\frac{\delta_T}{2}\right) - \delta_T - \delta_T\ln\left(\frac{\delta_T}{2}\right) - \frac{\delta_T}{2}E_1\left(\frac{\delta_T^2}{4a^2}\right) + \frac{\delta_T}{2}E_1\left(\frac{\delta_T^2}{4a^2}\right) + a\sqrt{\pi}\,\mathrm{erf}\left(\frac{\delta_T}{2a}\right)\right]$$

we have then the first constant C':

$$C' = K\left[-\delta_T + a\sqrt{\pi}\,\mathrm{erf}\left(\frac{\delta_T}{2a}\right)\right] \qquad (10)$$

Secondly, using the boundary condition:

$$v_z^{(2)}(\pm\delta_v/2) = 0$$

we then determine the second coefficient C'':

$$C'' = -C'\frac{\delta_v}{2} = K\left[\frac{\delta_v\delta_T}{2} - \frac{a\delta_v}{2}\sqrt{\pi}\,\mathrm{erf}\left(\frac{\delta_T}{2a}\right)\right] \qquad (11)$$

Finally we obtain :

$$v_z^{(2)} = K\left[-\delta_T + a\sqrt{\pi}\,\mathrm{erf}\left(\frac{\delta_T}{2a}\right)\right]\left(x - \frac{\delta_v}{2}\right) \tag{12}$$

From (B.3), we get the expression for $v_z^{(1)}$:

$$v_z^{(1)} = K\left[x^2\ln(x) - \frac{x^2}{2} - x^2 + \frac{K'}{2}x^2 + \int xE_1\left(\frac{x^2}{a^2}\right)dx + a^2\sqrt{\pi}\int \mathrm{erf}\left(\frac{x}{a}\right)d\left(\frac{x}{a}\right) + C_2\right]$$

$$v_z^{(1)} = K\left[x^2\ln(x) + \frac{K'-3}{2}x^2 + a^2\sqrt{\pi}\left(\frac{x}{a}\,\mathrm{erf}\left(\frac{x}{a}\right) + \frac{1}{\sqrt{\pi}}e^{-x^2/a^2}\right) + \int xE_1\left(\frac{x^2}{a^2}\right)dx + C_2\right]$$

the integral of $xE_1\left(\frac{x^2}{a^2}\right)$, is obtained by substituting $w = x^2/a^2$:

$$\int xE_1\left(\frac{x^2}{a^2}\right)dx = \frac{a^2}{2}\int E_1\left(\frac{x^2}{a^2}\right)d\left(\frac{x^2}{a^2}\right) = \frac{a^2}{2}\int E_1(w)dw = \frac{a^2}{2}\left(wE_1(w) - \int wdE_1(w)\right)$$

then for the last integral:

$$\int wdE_1(w) = \int wd\left[\int_1^\infty \frac{e^{-tw}}{t}dt\right] = \int w\int_1^\infty \frac{-te^{-tw}}{t}dtdw = -\int e^{-w}dw = e^{-w}$$

we get then :

$$\int xE_1\left(\frac{x^2}{a^2}\right)dx = \frac{a^2}{2}\left(wE_1(w) - e^{-w}\right).$$

finally $v_z^{(1)}$ is given by:

$$v_z^{(1)} = K\left[x^2\ln(x) + \frac{K'-3}{2}x^2 + a^2\sqrt{\pi}\left(\frac{x}{a}\,\mathrm{erf}\left(\frac{x}{a}\right) + \frac{1}{\sqrt{\pi}}e^{-x^2/a^2}\right)\right] + K\left[\frac{a^2}{2}\left(\frac{x^2}{a^2}E_1\left(\frac{x^2}{a^2}\right) - e^{-x^2/a^2}\right) + C_2\right] \tag{B.4}$$

the constant C_2 is given by taken the value of $v_z^{(2)}$ at $\delta_t/2$:

$$v_z^{(1)}(\pm\delta_t/2) = v_z^{(2)}(\pm\delta_t/2)$$

So we have for this continuity condition:

$$K' = -2\ln\left(\frac{\delta_T}{2}\right) - E_1\left(\frac{\delta_T^2}{4a^2}\right)$$

$$v_z^{(1)}(\pm\delta_T/2) = K\left[\frac{\delta_T^2}{4}\ln\left(\frac{\delta_T}{2}\right) - \frac{\delta_T^2}{4}\ln\left(\frac{\delta_T}{2}\right) - \frac{\delta_T^2}{4}\frac{E_1\left(\frac{\delta_T^2}{4a^2}\right)}{2} - \frac{3}{2}\frac{\delta_T^2}{4} + \sqrt{\pi}\frac{a\delta_T}{2}\,\mathrm{erf}\left(\frac{\delta_T}{2a}\right)\right.$$
$$\left. + \frac{a^2}{2}e^{-\delta_T^2/4a^2} + \frac{\delta_T^2}{4}\frac{E_1\left(\frac{\delta_T^2}{4a^2}\right)}{2} + C_2\right] = K\left[-\delta_T + a\sqrt{\pi}\,\mathrm{erf}\left(\frac{\delta_T}{2a}\right)\right]\left(\frac{\delta_T}{2} - \frac{\delta_v}{2}\right)$$

the equation is simplified:

$$K\left[-\frac{3}{2}\frac{\delta_T^2}{4} + \frac{a^2}{2}e^{-\delta_T^2/4a^2} + C_2\right] = K\left[-\frac{\delta_T^2}{2} + \frac{\delta_T\delta_v}{2} - \sqrt{\pi}\frac{a\delta_v}{2}\,\mathrm{erf}\left(\frac{\delta_T}{2a}\right)\right]$$

then the constant C_2 is determined by:

$$C_2 = -\frac{1}{8}\delta_T^2 + \frac{\delta_T\delta_v}{2} - \frac{a^2}{2}e^{-\delta_T^2/4a^2} - \sqrt{\pi}\frac{a\delta_v}{2}\,\mathrm{erf}\left(\frac{\delta_T}{2a}\right)$$

Finally the maximal convective velocity v_{max} is taken at $x = 0$:

$$v_{max} = v_z^{(1)}(0) = K\left(\frac{a^2}{2} + -\frac{1}{8}\delta_T^2 + \frac{\delta_T\delta_v}{2} - \frac{a^2}{2}e^{-\delta_T^2/4a^2} - \sqrt{\pi}\frac{a\delta_v}{2}\,\mathrm{erf}\left(\frac{\delta_T}{2a}\right)\right)$$

with:

$$K = \frac{g\beta AP_0}{4\pi\lambda\nu}$$

BIBLIOGRAPHY

[1] Eli Barkai, Yuval Garini, and Ralf Metzler. of single molecules in living cells. *Phys. Today*, 65(8):29, 2012.

[2] Jean-Yves Tinevez, Nick Perry, Johannes Schindelin, Genevieve M Hoopes, Gregory D Reynolds, Emmanuel Laplantine, Sebastian Y Bednarek, Spencer L Shorte, and Kevin W Eliceiri. Trackmate: An open and extensible platform for single-particle tracking. *Methods*, 115:80–90, 2017.

[3] A Cuche, B Stein, A Canaguier-Durand, E Devaux, C Genet, and TW Ebbesen. Brownian motion in a designer force field: dynamical effects of negative refraction on nanoparticles. *Nano letters*, 12(8):4329–4332, 2012.

[4] Andrey G Cherstvy and Ralf Metzler. Anomalous diffusion in time-fluctuating non-stationary diffusivity landscapes. *Physical Chemistry Chemical Physics*, 18(34):23840–23852, 2016.

[5] Ralf Metzler, Jae-Hyung Jeon, Andrey G Cherstvy, and Eli Barkai. Anomalous diffusion models and their properties: non-stationarity, non-ergodicity, and ageing at the centenary of single particle tracking. *Physical Chemistry Chemical Physics*, 16(44):24128–24164, 2014.

[6] Bo Wang, Stephen M Anthony, Sung Chul Bae, and Steve Granick. Anomalous yet brownian. *Proceedings of the National Academy of Sciences*, 106(36):15160–15164, 2009.

[7] James Clerk Maxwell. *A treatise on electricity and magnetism*, volume 1. Clarendon press, 1881.

[8] PN Lebedev. Experimental examination of light pressure. *Nuovo Cimento*, 15(195):195, 1883.

[9] Arthur Ashkin, James M Dziedzic, JE Bjorkholm, and Steven Chu. Observation of a single-beam gradient force optical trap for dielectric particles. *Optics letters*, 11(5):288–290, 1986.

[10] David G Grier. A revolution in optical manipulation. *nature*, 424(6950):810, 2003.

[11] Steven B Smith, Yujia Cui, and Carlos Bustamante. Overstretching b-dna: the elastic response of individual double-stranded and single-stranded dna molecules. *Science*, 271(5250):795–799, 1996.

[12] Jeffrey R. Moffitt, Yann R. Chemla, Steven B. Smith, and Carlos Bustamante. Recent advances in optical tweezers. *Annual Review of Biochemistry*, 77(1):205–228, 2008. PMID: 18307407.

[13] Michelle D Wang, Hong Yin, Robert Landick, Jeff Gelles, and Steven M Block. Stretching dna with optical tweezers. *Biophysical journal*, 72(3):1335–1346, 1997.

[14] Gabriel Schnoering, Lisa V. Poulikakos, Yoseline Rosales-Cabara, Antoine Canaguier-Durand, David J. Norris, and Cyriaque Genet. Three-dimensional enantiomeric recognition of optically trapped single chiral nanoparticles. *Phys. Rev. Lett.*, 121:023902, 7 2018.

[15] Juan José Sáenz. Optical forces: laser tractor beams. *Nature Photonics*, 5(9):514, 2011.

[16] Antoine Canaguier-Durand, James A Hutchison, Cyriaque Genet, and Thomas W Ebbesen. Mechanical separation of chiral dipoles by chiral light. *New Journal of Physics*, 15(12):123037, 2013.

[17] Robert P Cameron, Stephen M Barnett, and Alison M Yao. Discriminatory optical force for chiral molecules. *New Journal of Physics*, 16(1):013020, 2014.

[18] SB Wang and CT Chan. Lateral optical force on chiral particles near a surface. *Nature communications*, 5:ncomms4307, 2014.

[19] A. Cuche, A. Canaguier-Durand, E. Devaux, J. A. Hutchison, C. Genet, and T. W. Ebbesen. Sorting nanoparticles with intertwined plasmonic and thermo-hydrodynamical forces. *Nano Letters*, 13(9):4230–4235, 2013. PMID: 23927628.

[20] Robert Brown. Xxvii. a brief account of microscopical observations made in the months of june, july and august 1827, on the particles contained in the pollen of plants; and on the general existence of active molecules in organic and inorganic bodies. *The Philosophical Magazine*, 4(21):161–173, 1828.

[21] A Einstein. On the movement of small particles suspended in stationary liquids required by the molecularkinetic theory of heat. *Ann. d. Phys*, 17(549-560):1, 1905.

[22] Marian Smoluchowski. The kinetic theory of brownian molecular motion and suspensions. *Ann. Phys*, 21:756–780, 1906.

[23] Marian Smoluchowski. *Essai d'une théorie cinétique du mouvement Brownien et des milieux troublés*. Acad. Litterarum Cracoviensis, 1906.

[24] Jean Perrin. L'agitation moléculaire et le mouvement brownien. *Comptes rendus hebdomadaires des séances de l'académie des sciences*, 146:967–970, 1908.

[25] Paul Langevin. Sur la théorie du mouvement brownien. *Compt. Rendus*, 146:530–533, 1908.

[26] G. E. Uhlenbeck and L. S. Ornstein. On the theory of the brownian motion. *Phys. Rev.*, 36:823–841, Sep 1930.

[27] John C Crocker and David G Grier. Microscopic measurement of the pair interaction potential of charge-stabilized colloid. *Physical review letters*, 73(2):352, 1994.

[28] VD Nguyen, MT Dang, TA Nguyen, and P Schall. Critical casimir forces for colloidal assembly. *Journal of Physics: Condensed Matter*, 28(4):043001, 2016.

[29] James A Dix and AS Verkman. Crowding effects on diffusion in solutions and cells. *Annu. Rev. Biophys.*, 37:247–263, 2008.

[30] Jun Chen, Jack Ng, Zhifang Lin, and CT Chan. Optical pulling force. *Nature photonics*, 5(9):531, 2011.

[31] Veerachart Kajorndejnukul, Weiqiang Ding, Sergey Sukhov, Cheng-Wei Qiu, and Aristide Dogariu. Linear momentum increase and negative optical forces at dielectric interface. *Nature Photonics*, 7(10):787, 2013.

[32] Veerachart Kajorndejnukul, Sergey Sukhov, and Aristide Dogariu. Efficient mass transport by optical advection. *Scientific reports*, 5:14861, 2015.

[33] W. R. Schowalter W. B. Russel, D. A. Saville. *Colloidal Dispersions*.

[34] Sriram Ramaswamy. Issues in the statistical mechanics of steady sedimentation. *Advances in Physics*, 50(3):297–341, 2001.

[35] Ken Sekimoto. *Stochastic energetics*, volume 799. Springer, 2010.

[36] John C Crocker and David G Grier. Methods of digital video microscopy for colloidal studies. *Journal of colloid and interface science*, 179(1):298–310, 1996.

[37] Michael J Saxton. Single-particle tracking: the distribution of diffusion coefficients. *Biophysical journal*, 72(4):1744–1753, 1997.

[38] Richik N Ghosh and Watt W Webb. Automated detection and tracking of individual and clustered cell surface low density lipoprotein receptor molecules. *Biophysical journal*, 66(5):1301–1318, 1994.

[39] Bo Zhang, Josiane Zerubia, and Jean-Christophe Olivo-Marin. Gaussian approximations of fluorescence microscope point-spread function models. *Appl. Opt.*, 46(10):1819–1829, Apr 2007.

[40] Xavier Michalet. Mean square displacement analysis of single-particle trajectories with localization error: Brownian motion in an isotropic medium. *Physical Review E*, 82(4):041914, 2010.

[41] Michael P Brenner. Screening mechanisms in sedimentation. *Physics of fluids*, 11(4):754–772, 1999.

[42] Anand Yethiraj. Tunable colloids: control of colloidal phase transitions with tunable interactions. *Soft Matter*, 3(9):1099–1115, 2007.

[43] Clemens Bechinger, Roberto Di Leonardo, Hartmut Löwen, Charles Reichhardt, Giorgio Volpe, and Giovanni Volpe. Active particles in complex and crowded environments. *Reviews of Modern Physics*, 88(4):045006, 2016.

[44] Marco A Catipovic, Paul M Tyler, Josef G Trapani, and Ashley R Carter. Improving the quantification of brownian motion. *American Journal of Physics*, 81(7):485–491, 2013.

[45] CM Vest. Analysis of laser-induced convection in unconfined fluids and in vertical cylinders. *The Physics of Fluids*, 17(11):1945–1950, 1974.

[46] Michel Favre-Marinet and Sedat Tardu. *Convective Heat Transfer: Solved Problems*. John Wiley & Sons, 2013.

[47] Luc Petit, Jean-Pierre Hulin, and Étienne Guyon. *Hydrodynamique physique 3e édition (2012)*. EDP sciences, 2012.

[48] Radyadour Kh Zeytounian. Joseph boussinesq and his approximation: a contemporary view. *Comptes Rendus Mecanique*, 331(8):575–586, 2003.

[49] Adrian Bejan. *Convection heat transfer*. John wiley & sons, 2013.

[50] Edward M Purcell. Life at low reynolds number. In *Physics and Our World: Reissue of the Proceedings of a Symposium in Honor of Victor F Weisskopf*, pages 47–67. World Scientific, 2014.

[51] Kirstine Berg-Sørensen and Henrik Flyvbjerg. Power spectrum analysis for optical tweezers. *Review of Scientific Instruments*, 75(3):594–612, 2004.

[52] Arthur Ashkin. Acceleration and trapping of particles by radiation pressure. *Physical review letters*, 24(4):156, 1970.

[53] Arthur Ashkin. Applications of laser radiation pressure. *Science*, 210(4474):1081–1088, 1980.

[54] Craig F Bohren and Donald R Huffman. *Absorption and scattering of light by small particles*. John Wiley & Sons, 2008.

[55] Hendrik Christoffel Hulst and Hendrik C van de Hulst. *Light scattering by small particles*. Courier Corporation, 1957.

[56] Guillaume Baffou. Mie theory for metal nanoparticles, 2012.

[57] William M Irvine. Light scattering by spherical particles: radiation pressure, asymmetry factor, and extinction cross section. *JOSA*, 55(1):16–21, 1965.

[58] Giovanni Volpe, Laurent Helden, Thomas Brettschneider, Jan Wehr, and Clemens Bechinger. Influence of noise on force measurements. *Phys. Rev. Lett.*, 104:170602, Apr 2010.

[59] Albert Einstein. *Investigations on the Theory of the Brownian Movement*. Courier Corporation, 1956.

[60] Bertrand Duplantier. Brownian motion,"diverse and undulating". In *Einstein, 1905–2005*, pages 201–293. Springer, 2005.

[61] Ming Chen Wang and G. E. Uhlenbeck. On the theory of the brownian motion ii. *Rev. Mod. Phys.*, 17:323–342, Apr 1945.

[62] Nicolaas Godfried Van Kampen. *Stochastic processes in physics and chemistry*, volume 1. Elsevier, 1992.

[63] David W Allan. Should the classical variance be used as a basic measure in standards metrology? *IEEE Transactions on Instrumentation and Measurement*, 1001(2):646–654, 1987.

[64] Gabriel Schnoering. *On the Brownian dynamics of a particle in a bistable optical trap*. PhD thesis, Université de Strasbourg, 2016.

[65] Yvan RP Sortais. *Construction d'une fontaine double à atomes froids de 87Rb et 133Cs; Etude des effets dépendant du nombre d'atomes dans une fontaine*. PhD thesis, Université Pierre et Marie Curie-Paris VI, 2001.

[66] AN Cleland and ML Roukes. Noise processes in nanomechanical resonators. *Journal of Applied Physics*, 92(5):2758–2769, 2002.

[67] Fabian Czerwinski, Andrew C Richardson, and Lene B Oddershede. Quantifying noise in optical tweezers by allan variance. *Optics express*, 17(15):13255–13269, 2009.

[68] Xiaoji Niu, Qingjiang Wang, You Li, Qingli Li, and Jingnan Liu. Using inertial sensors in smartphones for curriculum experiments of inertial navigation technology. *Education Sciences*, 5(1):26–46, 2015.

[69] Rohit Jain and Kizhakeyil L Sebastian. Diffusion in a crowded, rearranging environment. *The Journal of Physical Chemistry B*, 120(16):3988–3992, 2016.

[70] S Condamin, Vincent Tejedor, Raphael Voituriez, Olivier Benichou, and Joseph Klafter. Probing microscopic origins of confined subdiffusion by first-passage observables. *Proceedings of the National Academy of Sciences*, 105(15):5675–5680, 2008.

[71] Ido Golding and Edward C. Cox. Physical nature of bacterial cytoplasm. *Phys. Rev. Lett.*, 96:098102, Mar 2006.

[72] Jedrzej Szymanski and Matthias Weiss. Elucidating the origin of anomalous diffusion in crowded fluids. *Phys. Rev. Lett.*, 103:038102, Jul 2009.

[73] Jae-Hyung Jeon, Natascha Leijnse, Lene B Oddershede, and Ralf Metzler. Anomalous diffusion and power-law relaxation of the time averaged mean squared displacement in worm-like micellar solutions. *New Journal of Physics*, 15(4):045011, 2013.

[74] Q. Xu, L. Feng, R. Sha, N. C. Seeman, and P. M. Chaikin. Subdiffusion of a sticky particle on a surface. *Phys. Rev. Lett.*, 106:228102, Jun 2011.

[75] I. Y. Wong, M. L. Gardel, D. R. Reichman, Eric R. Weeks, M. T. Valentine, A. R. Bausch, and D. A. Weitz. Anomalous diffusion probes microstructure dynamics of entangled f-actin networks. *Phys. Rev. Lett.*, 92:178101, Apr 2004.

[76] Weihua Deng and Eli Barkai. Ergodic properties of fractional brownian-langevin motion. *Physical Review E*, 79(1):011112, 2009.

[77] George David Joseph Phillies. In complex fluids the gaussian diffusion approximation is generally invalid. *Soft matter*, 11(3):580–586, 2015.

[78] Iva Marija Tolić-Nørrelykke, Emilia-Laura Munteanu, Genevieve Thon, Lene Oddershede, and Kirstine Berg-Sørensen. Anomalous diffusion in living yeast cells. *Physical Review Letters*, 93(7):078102, 2004.

[79] Jincheng Mao, Heng Zhang, Wenlong Zhang, Jinming Fan, Chong Zhang, and Jinzhou Zhao. Dissymmetric beauty: A novel design of heterogemini viscoelastic surfactant for the clean fracturing fluid. *Journal of industrial and engineering chemistry*, 60:133–142, 2018.

[80] Ralf Metzler and Joseph Klafter. The random walk's guide to anomalous diffusion: a fractional dynamics approach. *Physics reports*, 339(1):1–77, 2000.

[81] Gyemin Kwon, Bong June Sung, and Arun Yethiraj. Dynamics in crowded environments: is non-gaussian brownian diffusion normal? *The Journal of Physical Chemistry B*, 118(28):8128–8134, 2014.

[82] T. H. Solomon, Eric R. Weeks, and Harry L. Swinney. Observation of anomalous diffusion and lévy flights in a two-dimensional rotating flow. *Phys. Rev. Lett.*, 71:3975–3978, Dec 1993.

[83] Weihua Deng and Eli Barkai. Ergodic properties of fractional brownian-langevin motion. *Phys. Rev. E*, 79:011112, Jan 2009.

[84] Jae-Hyung Jeon, Aleksei V. Chechkin, and Ralf Metzler. Scaled brownian motion: a paradoxical process with a time dependent diffusivity for the description of anomalous diffusion. *Phys. Chem. Chem. Phys.*, 16:15811–15817, 2014.

[85] Georgiy Tkachenko and Etienne Brasselet. Optofluidic sorting of material chirality by chiral light. *Nature communications*, 5:3577, 2014.

[86] Kevin M McPeak, Christian D Van Engers, Mark Blome, Jong Hyuk Park, Sven Burger, Miguel A Gosalvez, Ava Faridi, Yasmina R Ries, Ayaskanta Sahu, and David J Norris. Complex chiral colloids and surfaces via high-index off-cut silicon. *Nano letters*, 14(5):2934–2940, 2014.

[87] Jonathan R. Howse, Richard A. L. Jones, Anthony J. Ryan, Tim Gough, Reza Vafabakhsh, and Ramin Golestanian. Self-motile colloidal particles: From directed propulsion to random walk. *Phys. Rev. Lett.*, 99:048102, Jul 2007.

Résumé en français suivi des mots-clés en français

Le travail réalisé dans cette thèse porte sur l'étude du mouvement Brownien d'une suspension colloïdale sous champ de force optique faible et l'étude fondamentale des effets convectifs et de diffusion anormale. Nous avons construit un microscope à fond noir afin de suivre les particules et de reconstruire leurs trajectoires avec une résolution spatiale de 20 nm et une résolution temporelle de 8 ms. Ces trajectoires sont analysées statistiquement afin d'en extraire la contribution balistique induite par la force de pression de radiation appliquée par le laser d'illumination. En plus de l'effet mécanique du laser sur les particules, le fluide absorbe les radiations ce qui le chauffe et crée ainsi une différence de température entre la partie illuminée et la partie non illuminée de l'échantillon.

Nous validons aussi les hypothèses de stationnarité et d'érgodicité qui sont fondamentales pour notre stratégie de mesure de force faible. L'analyse statistique fine de notre système nous permet de mettre en évidence et de caractériser des effets de diffusion anormale brownienne. Nos expériences révèlent en effet la présence de trajectoires anormales dont l'origine se comprend comme un effet d'interaction entre la particule suivie et le reste de l'ensemble colloïdal.

Mots clés :

Mouvement Brownien, Force optique, diffusion anormales, Ergodicité.

Résumé en anglais

The work presented in this thesis deals with the study of the Brownian motion of a colloidal suspension under an external weak optical force, the study of convective effects and anomalous diffusion. We have built a dark field microscope in order to track the particles and reconstruct the Brownian trajectories with a spatial resolution of 20 nm and a temporal resolution of 8 ms.

Statistical analysis of the trajectories has allowed us to extract the ballistic contribution induced by the radiation pressure force exerted by irradiating a laser on the particles.

In addition to the mechanical effect of the laser on the particles, the fluid absorbs the radiation. Consequently, the temperature of the fluid rises and results in a thermal difference between the illuminated and the non-illuminated areas of the sample.

In order to validate our weak force measurement, we have investigated two fundamental hypotheses in statistical physics: ergodicity and stationary aspect. A closer statistical analysis enables us to demonstrate and characterize the effect of anomalous Brownian diffusion. Our experiments have revealed the existence of anomalous trajectories, which can be understood as an effect of the interactions between the particles.

Keywords:

Brownian motion, optical force, anomalous diffusion, ergodicity